Masteroppgave

NTNU
Norges teknisk-naturvitenskapelige universitet
Fakultet for informasjonsteknologi og elektroteknikk
Institutt for elkrafteknikk

Ole Amund Storlien

Comparison of droop-based grid-forming and PLL-based grid-following control of VSC during symmetrical fault

Masteroppgave i Energi og Miljø
Veileder: Kjetil Obstfelder Uhlen
Medveileder: Atle Rygg

Oktober 2022

NTNU
Kunnskap for en bedre verden

Ole Amund Storlien

Comparison of droop-based grid-forming and PLL-based grid-following control of VSC during symmetrical fault

Masteroppgave i Energi og Miljø
Veileder: Kjetil Obstfelder Uhlen
Medveileder: Atle Rygg
Oktober 2022

Norges teknisk-naturvitenskapelige universitet
Fakultet for informasjonsteknologi og elektroteknikk
Institutt for elkraftteknikk

NTNU
Kunnskap for en bedre verden

Preface

This master thesis concludes my tenth and final semester of my masters degree in Energy and Environmental Engineering at the Norwegian University of Science and Technology. This thesis is a continuation of my project thesis last semester. While a lot of the scope of work and objective has changed, some aspects are still very relevant. Because of this the most essential parts of the theory and literature is reused in this thesis. This is yields for the chapter about grid codes as well as the maritime electrification.

Even though I am the author of this thesis, there are several people I would like to thank. I would like to thank my supervisor Kjetil Uhlen for counselling through the last year, with both the master thesis and project thesis. Many of our meetings the last semester has been online in order to facilitate for my needs, which I am very grateful for. The same must also be said for my co-supervisor Atle Rygg from Siemens Energy. In addition I would like to thank Atle for helping me with creating a model sufficient for the scope of the thesis and for making sure this master thesis became as exciting to work with as I hoped.

Lastly I would like to thank my family, my friends and my girlfriend, Maria, for all their support, love and motivating words throughout this final year.

Ole Amund Storlien, Oslo 2022

Abstract

This thesis is about controlling of voltage source converters during a fault scenario. More specifically it is about comparing two different control methods, namely droop-based grid-forming control and PLL-based grid-following control. The fault conditions are varied in order to uncover the performance characteristics of the two control methods and quantify their advantages and disadvantages. During the simulation study the difficulty of limiting fault currents in grid-forming control was discovered. Two simple methods of limiting the fault current was discovered, and compared with each other, as well as with the grid-following control.
The comparison was done in a scenario provided by Siemens Energy - Offshore Marine Center. They have field experience with operation and control of droop-based grid-forming converters, through their work in delivering power system solutions to electric passenger ferries in Norway. Their challenges related to handling of faults in the outer-lying grid during charging, is the background for the simulation study in this thesis. The scenario was modelled in the Matlab/Simulink environment, and the simulation study performed in the time-domain.
The main difference between the control methods ability to handle a symmetrical fault is related to their control objectives. The grid-forming converter injects large reactive currents to prevent the voltage from dropping, whereas the grid-following converter allows the voltage to drop. The fault current limitation was done through saturating or removing the feed-forward term in the voltage control loop. This came at a large cost of performance for the grid-forming control, resulting in a superior ability to handle the fault for the grid-following control.
The grid-forming converter had less robustness when it came to varying fault duration, and had a smaller critical clearing time than compared to the grid-following converter. The effect of increasing the fault magnitude, i.e fault current, was less detrimental than increasing the fault duration. The grid-following converters point of weakness was discovered when increasing the line impedance, as it highly dependant on a strong connection to the power grid. It was therefore concluded that without proper fault current limitations techniques in the droop-based grid-forming converter, the PLL-based grid-following converter performs better whenever not exposed to a high impedance grid

Sammendrag

Denne oppgaven handler om kontroll av spenningsomformere under et feilscenario. Mer spesifikt så handler oppgaven om sammenligning av to forskjellige kontrollmetoder, droop-basert nettdannende kontroll og faselåst-sløyfe basert nettfølgende kontroll. Feilscenarioene vil bli variert for å bestemme karakteristikken til de to forskjellige kontrollmetodene, og for å kvantifisere fordelene og ulempene ved de. Under simuleringen ble det oppdaget vanskeligheter med å begrense feilstrømmene i den nettdannende kontrollmodusen. To enkle måter å begrense feilstrømmene ble funnet ut av, og sammenlignet med hverandre, samt den nettfølgende kontrollmetoden.
Sammenligninen er gjort i et scenario gitt av Siemens Energy - Offshore Marine Center. De har felterfaring med droop-basert nettdannende kontrol av spenningsomformere gjennom deres arbeid med å levere kraftsystem og ladesystem til elektriske passasjerferger i Norge. De har opplevd utfordringer knyttet til feilsituasjoner i ytterliggende nett under lading, og dette vil være bakgrunnen for simuleringene som gjøres i denne oppgaven. Scenarioet er modellert i Matlab/Simulink, og analysen gjøres i tids-domenet.
Hovedforskjellene mellom kontrollmetodenes evne til å håndtere en symmetrisk feil er knyttet til kontrollmålene deres. Den nettdannende spenningsomformeren vil injisere reaktive strømmer til kraftsystemet for å opprettholde spenningsnivået, mens den nettfølgende spenningsomformeren vil tillate spenningen å falle. Feilstrømbegrensningene ble gjort gjennom å innføre metningsgrenser på foroverkoblingen i spenningsløkka eller fjerne den totalt. Dette gikk veldig på bekostning av prestasjonen til den nettdannende spenningsomformeren, som gjorde at den nettfølgende spenningsomformeren håndterte feilsituasjonen betydelig bedre.
Den nettdannende spenningsomformeren var mindre robust når det gjaldt økt feiltid, og hadde en lavere kritisk klareringstid sammenlignet med nettfølgende spenningsomformeren. Effekten av økende feilstørrelse, m.a.o feilstrøm, var mindre skadelig enn effekten av økt feiltid. Den nettfølgende spenningsomformeren sin svakhet ble tydelig da linjeimpedansen ble økt, ettersom den er sterkt avhengig av en god forbindelse til det ytterliggende nettet. Det ble derfor konkludert at uten riktige strømbegrensningsmetoder på den droop-baserte nettdannende spenningsomformeren, så vil den faselåste-sløyfe-baserte nettfølgende spenningsomformeren prestere bedre utenom i scenarioer med høy linjeimpedanse.

Outline

List of Tables

List of Figures

List of Abbreviations

DG distributed generation electrical generation and storage performed by a variety of small, grid-connected or distribution system-connected devices. 20

FOL Forskrift om leveringskvalitet i kraftsystemet The Norwegian grid codes standard. 9

NVE Norges Vassdrag-og Energidirektorat The Norwegian Water Resource and Energy Directorate. 9

PCC point of common coupling the point in the power system at which the electric utility and the customer interface occurs. 16

PLL phase-locked loop a control system that generates an output signal whose phase is related to the phase of an input signal. 2

RMS root means square the square root of the arithmetic mean of the squares of a set of values. 9

THD total harmonic distortion a measurement of the harmonic distortion present in a signal and is defined as the ratio of the sum of the powers of all harmonic components to the power of the fundamental frequency. 12

VSC voltage source converter Power electronic device enabling conversion between AC and DC voltage. 1, 2

1. Introduction

1.1. Background and Objective

The stability of today's power systems is highly dependent on rotating kinetic energy present in the power system. This kinetic energy is supplied through large synchronous generators in a centralised production of electrical power. This electrical production must at all times meet the demand from the de-centralised consumers in the outer grid. Imbalances between production and demand causes variations of the power systems frequency which, large enough, can cause power systems to collapse. The inertia of the large synchronous generators yields the power system the ability to resist frequency changes [19]. Mowing towards the power system of the future introduces a larger share of renewable energy sources such as wind and solar. Most of this production will be done by small-scale, de-centralised power plants even though larger production units are also foreseen. In addition HVDC import and export of power between countries will play a larger part in the future as well. Common for all of these is that they are connected to the power system through power electronics which decreases the rotating kinetic energy - reducing the stability of the power systems [5].

Norway is world leading within electrifying the transport sector [10]. This also includes maritime transportation, in in which Norway is leading the process of transforming the maritime fleet into the zero-emission future. The electric ferries have been the door opening for this transition and about 60 electrical ferries are presently operated purely based on batteries with shore charging. Furthermore there will be 20 additional ferries operating by 2022 [7]. The power system architecture of marine vessels are complicated and complex, with a high penetration of power electronics. They are characteristic in the way that they can be considered as microgrids as they must be able to operate independently when out on the water, as well as be able to connect to the on-shore power system whenever charging. At the centre of these microgrids are the voltage source converter. It allows conversion between AC voltage and DC voltage through control of semi-conductor switches. This is vital as the varied power electronics on-board and other power drawing elements have to be operated on different voltages. Hence the operation and control of the VSC voltage source converter becomes a crucial task.
There are different ways of controlling the VSC voltage source converter and several ways of implementations this [17]. However there are generally two principles, either grid-forming or grid-following control, in which the control objectives are different. For grid-forming control the objective is to maintain the AC voltage level and frequency and can therefore be considered as a voltage source. Whereas grid-following control focuses on maintaining active power, reactive power or the dc-voltage level, by injecting currents and can therefore be considered as a current source. It leaves the responsibility maintaining of the frequency and AC voltage to the power grid. For the purpose of controlling the on-board power system, it is therefore necessary with grid-forming control because it has the ability of being the voltage source. Traditionally the grid-following control is a established concept which is widely used because of it reliability, robustness and good performance. However, moving

towards the power system of the future the presence of a strong grid in which it can follow will be weakened. Hence it is necessary to ensure that the grid-forming converter is able to perform as satisfactory as the grid-following converter.
Siemens Energy Offshore Marine Center have field experience with implementing grid-forming converters in their deliverance of power systems and charging solutions for electrical passenger ferries. While the electrification of the maritime fleet is still very much an undergoing process, there are some challenges which have been discovered in the projects that already have been delivered. In this thesis the focus will be on challenges with faults, or short-circuits, in the outer-lying grid and the grid-forming converters ability to handle these during charging. In order to study this, the performance of a grid-forming converter will be compared with a grid-following converter during a fault scenario. These will be modelled in the Simulink Environment, and a simulation study will be done. In addition fault parameters, and other critical parameters will be varied and the effect of these will be quantified. The purpose of this study is to quantify the differences in performance when handling a fault scenario, as well as to enlighten the difficulties of fault handling with the grid-forming converter.

1.2. Scope of work

The scope of work for this thesis is to:

- Model a VSC voltage source converter and LCL-filter
- Model and verify droop-based Grid forming control
- Model and verify PLL phase-locked loop-based grid-following control
- Study and compare the impact of a three-phase fault
- Study and compare the effect of fault duration and fault magnitude
- Study and compare the effect of varying line impedance

1.3. Outline

This thesis consist of nine chapters:

Chapter 1 Introduces the background and objective of the thesis as well as the scope of work.
Chapter 2 Gives an insight to the relevant theoretical background for better understanding the concepts and explanations in this thesis.
Chapter 3 Introduces the voltage source converter and gives insight into its working principle and topology, the park transformation utilized in modelling, as well as a

introduction to the working principle of the grid following and grid forming control methods.
Chapter 4 Gives detailed description of how the modelling of the grid-forming control method was done.
Chapter 5 Gives detailed description of how the modelling of the grid-following control method was done.
Chapter 6 Provides a description of the simulation model and its parameters.
Chapter 7 is the simulation study where the results are presented
Chapter 8 is the discussion of the results from the simulation study.
Chapter 9 contains the conclusion and suggestions for further work.

1.4. Relation to specialization project

The work done in this thesis is based on the work done in the specialization project [33]. The sections that bare resemblance to the specialization project are:

- subsection 2.1
- subsection 2.4
- subsection 2.2

2. Theoretical Background

In order to better the understanding of the concepts in this thesis for the reader it is necessary to be introduced to some theoretical background beforehand. Firstly a short review of the architectures of the marine power system present in electric passenger ferries will be presented. These systems are complex and contain a lot of power electronics, it is therefore important to understand the role of the VSC in these. Moreover the power flow between the grid and the on-board batteries, through the VSC, is essential for this thesis and the power flow dynamics will therefore be reviewed. In addition theory of the three-phase fault will be introduced. Lastly grid codes concerning power quality for the Norwegian power system will be reviewed.

2.1. Marine Power Systems

Even though there are examples of electric ferries as early as the 1830s, the concept as we know it today is relatively new. The first fully electric battery powered passenger ferry, MF Ampere, was introduced in 2015 in Norway [31]. A simplified one-line diagram of its on-board power system is shown in Figure 1.

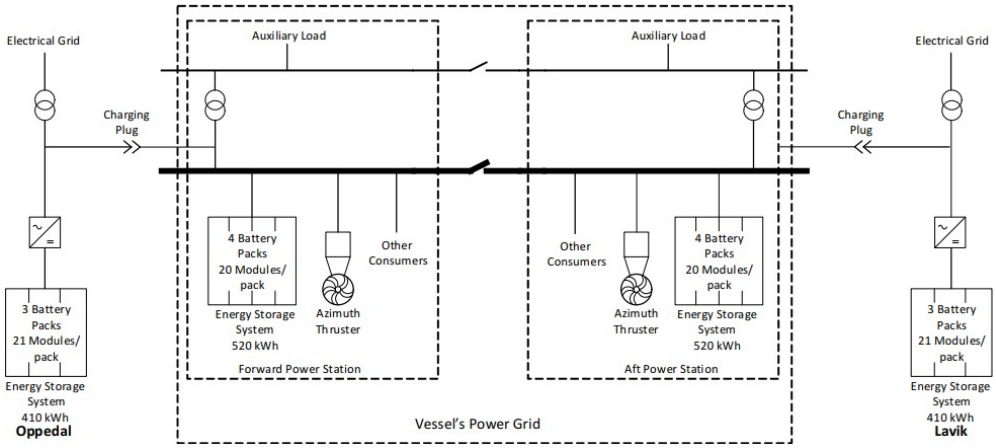

Figure 1: A simplified one-line diagram of the on-board power system of MF Ampere [15]

Today the most common design for the power system architecture and its corresponding shore-to-ship charging design is based on plug-in charging. Other solutions such as wireless charging and battery swapping shows promise, but is currently not as widespread [15]. The on-board electrical power system generally has two different structures based on whether it is operating on AC or DC. The charging system can also be based on either AC or DC, which leads to four different combinations. For AC charging two possible system architectures are shown in Figure 2. For DC charging two possible system architectures are shown in Figure 3. Most passenger ferries will have more than one on-board bus, however here one is drawn for simplicity.

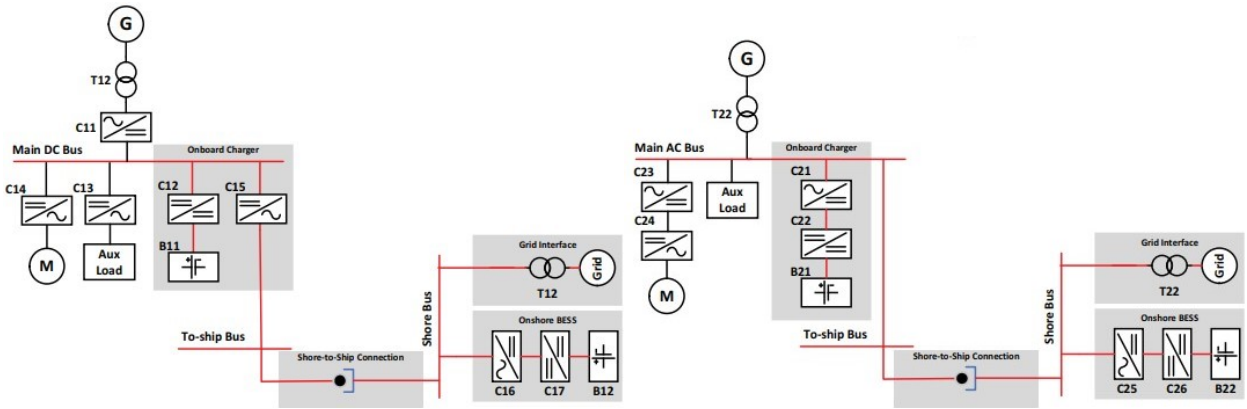

(a) DC on-board power system **(b)** AC on-board power system

Figure 2: AC charging system for (a) DC on-board power system and (b) AC on-board power system [14]

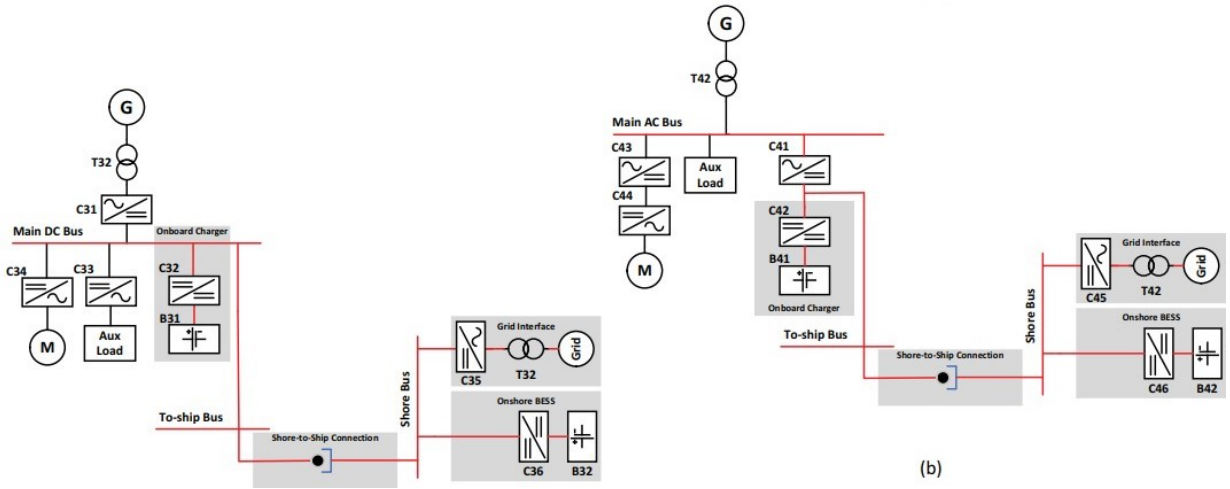

(a) DC on-board power system **(b)** AC on-board power system

Figure 3: DC charging system for (a) DC on-board power system and (b) AC on-board power system [14]

There are several advantages and disadvantages with the different combinations. However in most cases the most energy efficient is the design in 2a due to the low-weight of the DC on-board system, less power electronics on-board and reduced need for synchronizing to the on-shore grid [14]. This will be the chosen solution for this thesis because of this and because of the similarities with the solution used by Siemens Energy [29]. As these are complex systems with a high penetration of power electronics a simplified model will be utilized in the simulations, which will be presented later in the thesis.

2.2. Power flow dynamics

In order to derive the power flow equations a simplified model of the system is used. The VSC is represented as an ideal voltage source delivering power through an impedance to a load. This is shown in Figure 4. By modelling in this way the current flowing will be according to Equation 1.

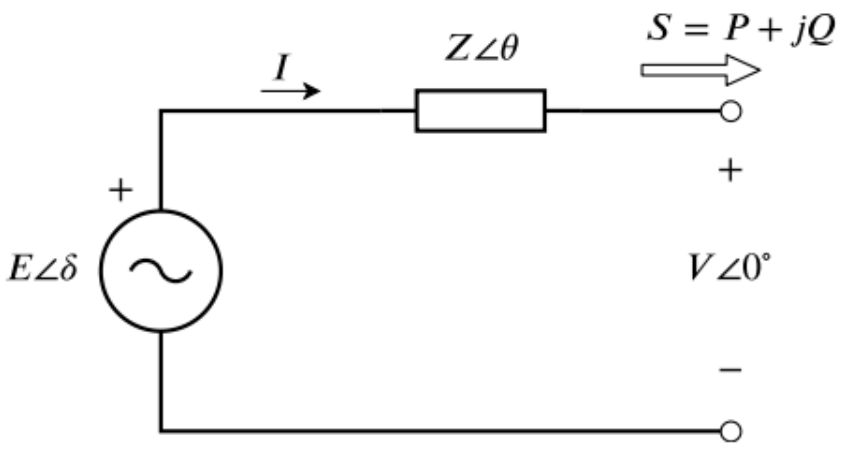

Figure 4: Voltage source delivering power through an impedance [22]

$$I = \frac{E\angle\delta - V\angle 0^{\circ}}{Z\angle\theta} \tag{1}$$

The output power is given by $S = VI^*$, such that by solving for active and reactive power the equations in Equation 2 is given.

$$P = (\frac{EV}{Z}\cos\delta - \frac{V^2}{Z}\cos\theta) + \frac{EV}{Z}\sin\delta\sin\theta \tag{2a}$$

$$Q = (\frac{EV}{Z}\cos\delta - \frac{V^2}{Z}\sin\theta) - \frac{EV}{Z}\sin\delta\cos\theta \tag{2b}$$

In this model the transmission line operates at at 66 kV. For a high voltage transmission line the impedance is substantially larger than the resistance [19]. Hence the $\frac{R}{X}$ ratio is so small that it is negligible, which yields $\theta = 90°$. Furthermore, assuming that σ is small, these assumptions yields the simplification shown in Equation 3. The $\frac{R}{X}$ ratio will not negligible for the 690 V line, however this line is very short in real life, such that the impact it has on the power flows is negligible.

$$P = \frac{EV}{X}\cos\delta \approx \frac{EV}{X}\delta \tag{3a}$$

$$Q = \frac{EV}{X}\cos\delta - \frac{V^2}{X} \approx \frac{EV - V^2}{X} \tag{3b}$$

From Equation 3 it is clear that the active power P is highly dependent on the phase angle, δ, of the voltage. The phase angle is proportional to the integral of the frequency f. Hence the active power can be controlled by manipulating the frequency. As can be seen the reactive power Q is equally dependent on the voltage amplitude.

By further investigating Equation 3 and renaming the variables to reflect the receiving-end and sending-end voltage and power they can be used to describe the dynamics of the power flow in the transmission lines as well. For a reference phasor $\underline{V}_R$ that lags $\underline{V}_S$ by phase angle δ_{SR}, that is $V_R = V_R \angle \underline{0}^\circ$ and $\underline{V}_S = V_S e^{j\delta_{RS}}$. Then the real power transfer of a line is given by Equation 4 [19].

$$P_R = \frac{V_s V_R}{X} \sin \delta_{SR} \tag{4}$$

Furthermore, the reactive power transfer of a line can then be described by Equation 5. It shows that it flows from the higher voltage to the lower voltage. From this it is possible to deduce that an increase in Q_R leads to a decrease in V_R, while a decrease in Q_R leads to an increase in V_R.

$$Q_R = \frac{V_R(V_s - V_R)}{X} \tag{5}$$

For the sending end reactive power a similar relationship can be developed, as shown in Equation 6.The strong dependence of reactive power with voltage magnitude is apparent and, as V_S is assumed constant, the approximate variation of Q_S with V_R is linear.

$$Q_s = \frac{V_S(V_S - V_R)}{X} \tag{6}$$

As the real power increases, the reactive power loss in the line is also profound, as shown in Equation 7. This loss must be supplied from the sending end giving an increase in Q_s, as shown in Equation 6. In this model the sending-end voltage will be constant, as it is modelled as a stiff voltage source. Hence, in order to increase Q_s then V_R must reduce. If the resulting reduction in V_R is unacceptable then this can be compensated by adjusting Q_R in some way, by introducing some form of reactive power compensation. [19]. P_{SIL} is the surge impedance loading of the transmission line [26].

$$\Delta Q(P_R) \approx \frac{2P_{SIL}}{\sin \beta l} * (\cos \beta l - \sqrt{1 - (\frac{P_R \sin \beta l}{P_{SIL}})^2}) \tag{7}$$

2.3. Three Phase Symmetrical faults in the Power System

Faults, or short-circuits, in power systems occur from time to time and with varying degree. Short circuits occur in power systems when equipment insulation fails due to system overvoltages caused by lightning or switching surges, to insulation contamination (salt spray or pollution), or to other mechanical causes [8]. The short-circuit can be both symmetrical or un-symmetrical. In three phase power systems the types of short circuits that occur most frequently are single line-to-ground, line-to-line, double line-to-ground and then balanced three-phase faults. The first three are un-symmetrical faults and the latter is a symmetrical fault. When analysing un-symmetrical faults it is necessary to describe it using positive-, negative and zero-sequence networks as they are interconnected at the fault cite only [8]. Whenever a three-phase fault occurs in a balanced power system sequence networks are not necessary as there is only positive sequence fault current since the negative-, zero-sequence networks are completely uncoupled. Even though, balanced three-phase short circuits are rarest, this thesis will focus on them as they are the most comprehensive, and the worst-case scenario is of interest. Any fault current will also include sub-transient and transient responses due to time varying reactance of the voltage source. However this is not included in the model.

Any fault current consist of both a steady-state component and a time-dependent component. These are often referred to as the AC fault current and the DC offset fault current respectively. In order to derive this consider the R-L circuit shown in Figure 5. By applying Kirchhoff's voltage law on the circuit the resulting equation is given by Equation 8. Here the voltage angle α is given by the time the switch closes, $t = 0$.

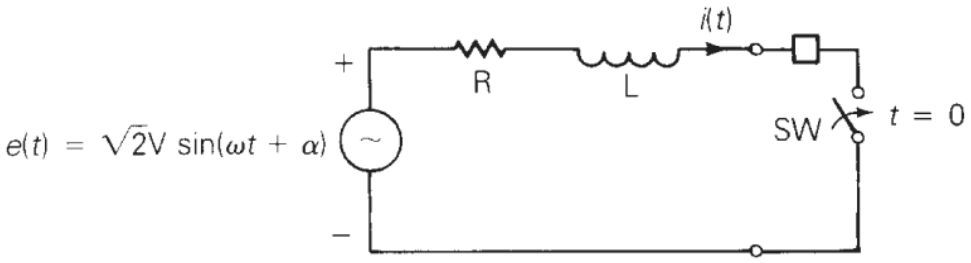

Figure 5: R-L circuit with ac voltage source

$$\frac{Ldi(t)}{dt} + Ri(t) = \sqrt{2V}\sin\omega t + \alpha t \geq 0 \tag{8}$$

The solution to Equation 8 is shown in Equation 9. The total fault current in Equation 9, called the asymmetrical fault current, is plotted in Figure 6, along with its two components.

The AC fault current is a sinusoid. Whereas the DC-component decays exponentially with time constant $T = \frac{L}{R}$.

$$i(t) = i_{ac}(t) + i_{dc}(t) = \frac{\sqrt{2}V}{Z}[\sin \omega t + \alpha - \theta - \sin \alpha - \theta e^{\frac{-t}{T}}] \tag{9}$$

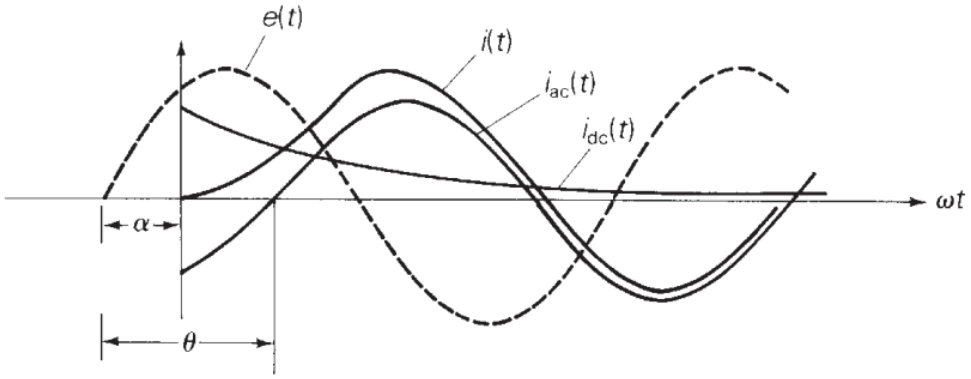

Figure 6: Fault Currents in the R-L circuit [8]

2.4. Power Quality Requirements and Standards

Power quality is a complex area covering many different topics. There are several different ways to characterise the different subjects, and different standards have been developed in order to do so. EN 50160 is the European standard [3], while in Norway the standard is developed by NVE Norges Vassdrag-og Energidirektorat and called FOL Forskrift om leveringskvalitet i kraftsystemet [23]. A supplementary description of the regulation is also provided by NVE, [1]. The power quality challenges that are most relevant for this thesis is subjects related to voltage levels and harmonics. The FOL introduces limits and regulations for these subjects, and will be reviewed in the following chapters.

2.4.1. Slow variations, voltage leap, voltage sag and surge

The first responsibility of the system operator presented in [23] is that the frequency of the voltage is maintained within $50Hz \pm 2\%$ in power networks that are temporarily without connection to bordering power grids. This implies that the frequency of the power system on-board the marine vessel should stay within these limits.
Furthermore the system operator is responsible for not allowing slow variations in the RMS root means square value of the voltage to exceed 10% of its nominal value, measured as an average over a minutes interval, in a point of connection in a low voltage network. The European standard deviates from the Norwegian here, as they allow an average to be measured over an interval of 10 minutes, instead of 1 minute.

Voltage leap, sag and surges are rapid changes in voltage rms value, that either increases or decreases, but relatively quickly returns to initial value, usually within a minutes interval. The limits set by the grid codes for voltage sags and surges are summarised in Table 1. From Table 1 it can be concluded that in order to be classified as either a leap, sag or surge in must have a stationary deviation exceeding 3% or a maximum deviation exceeding 5%.

Voltage leaps, sags and surges	**maximum number allowed during a 24 hour period**	
	0.23 kV $\leq$ $U_N \leq$ 35 kV	35 kV $<$ U_N
$\Delta_{ss} \leq 3\%$	24	12
$\Delta_{max} \leq 5\%$	24	12

Table 1: limits for voltage sags and surges [1]

In Figure 7 an illustration of a voltage surge is shown. Voltage surges are fast increases in the rms value to more than 1.1 pu of the nominal value with a typical duration of $10 - 60$ms. The voltage surge is over when the rms value of all of the three-phases drop below 1.1 pu.

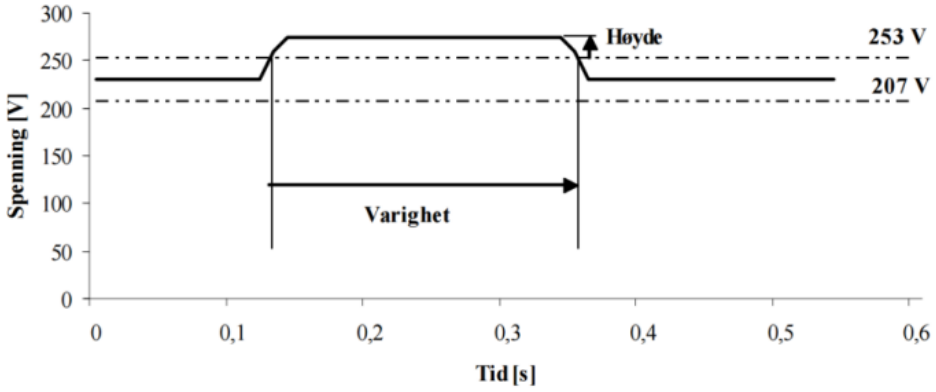

Figure 7: Illustration of a voltage surge [1]

Voltage sags is similarly a fast decrease in the rms value of the voltage level to below 0.9 pu with a duration of $10 - 60$ ms. This is illustrated in Figure 8. As described earlier the voltage must drop below 0.95 pu in order to be classified as voltage sag, otherwise it is classified as an interruption. The voltage sag is over when the voltage level increases to more than 0.9 pu for all of the three phases.

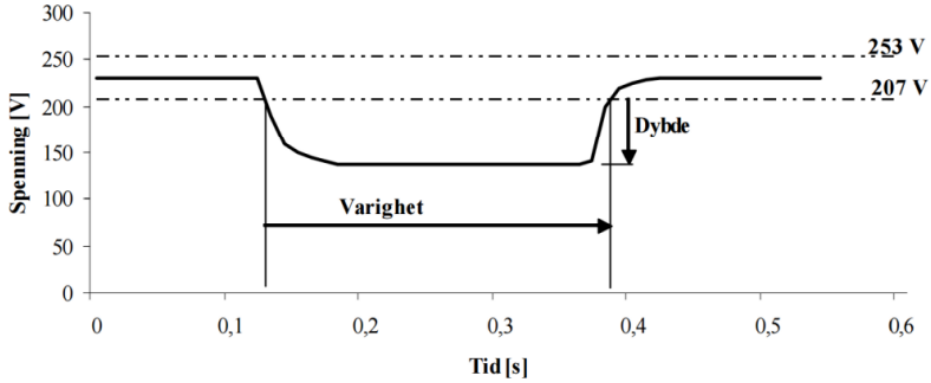

Figure 8: Illustration of a voltage sag [1]

A voltage leap is illustrated in Figure 9. This can be either a fast increase or decrease, however the rms value stays within ±0.1 pu of the nominal voltage during the maximum deviation and the stationary deviation. The rate of change must also be faster than 0.05 pu per second.

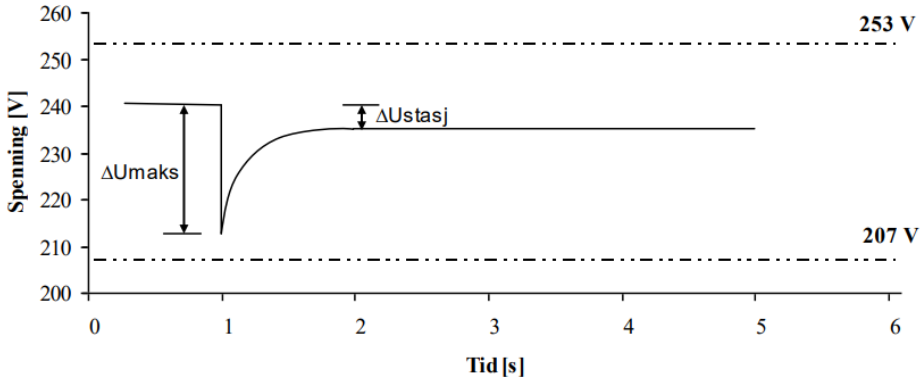

Figure 9: Illustration of a voltage leap [1]

2.4.2. Harmonics and inter-harmonics

There are two harmonic components that can occur in the power system, namely harmonic and interhamonic. A harmonic component is a sinus-shaped voltage curve with a frequency that is a multiple of the fundamental frequency, 50 Hz. That is, a integer multiplied with the fundamental frequency, such that a harmonic component will always have a frequency that is a n'th multiple of the fundamental frequency. The most common harmonics are the odd ones, such as $3rd$, $5th$, $7th$ and $9th$ harmonics. For inter-harmonics the multiple of the fundamental frequency of the sinus-shaped voltage curve does not have to be an integer.

For an individual harmonic component, U_k, the deviation it causes is defined by Equation 10

$$\%U_K = \frac{U_K}{U_1} * 100\% \tag{10}$$

While the THD total harmonic distortion is the sum of all individual harmonic deviations, and is defined by Equation 11.

$$\%THD_U = \frac{\sum_k^n U_k^2}{U_1} * 100\% \tag{11}$$

The system operator is responsible for that the THD of the voltage does not exceed 8% and 5% measured as an average over 10 minutes and a week, respectively. This yields for any point of connection in a network with a nominal voltage, $230V \leq U_N \leq 35kV$.

The system operator is also responsible for that any individual over-harmonic voltage does not exceed the values summarised in Table 2

Odd harmonics				Even harmonics	
Not multiple of 3		Multiple of 3			
Order h	U_h	Order h	U_h	Order h	U_h
5	6,0%	3	5,0%	2	2,0%
7	5,0%	9	1,5%	4	1,0%
11	3,5%	>9	0,9%	>4	0,5%
13	3,0%				
17	2,0%				
19,23,25	1,5%				
>25	1,0%				

Table 2: limits for harmonics [1]

3. Description and modelling of Voltage Source Converter

3.1. Topology and Working principle

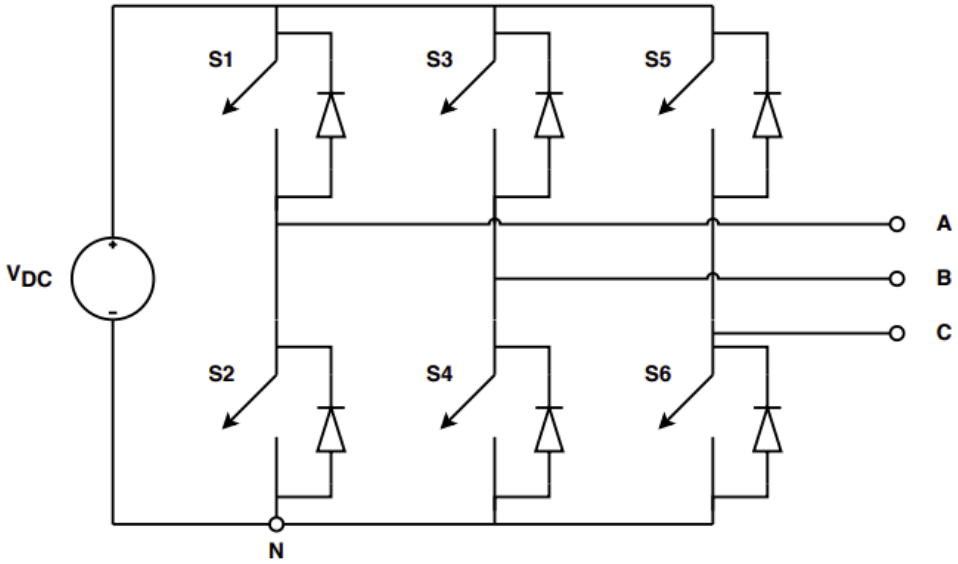

Figure 10: VSC topology [22]

In Figure 10 the structure of a two-level voltage source converter is shown. The purpose of the VSC is to convert the input voltage, whether it is AC or DC, to the opposite at the output voltage. The frequency and magnitude of the output voltage is controlled through operating the semi-conductor switches $S1 - S6$. The switches are turned on or off in a high frequency in order to create the desired waveform of the output signal. The desired waveform depends on whether the VSC is operating as a rectifier or inverter. The switching scheme is done by comparing a high frequency triangle signal with a sinusoidal wave, often referred to as the control signal. Whenever the control signal is greater than the triangle signal, the switch corresponding to that sine wave is turned on. Similarly, when the control signal is less than the triangle signal, the switch is turned off.

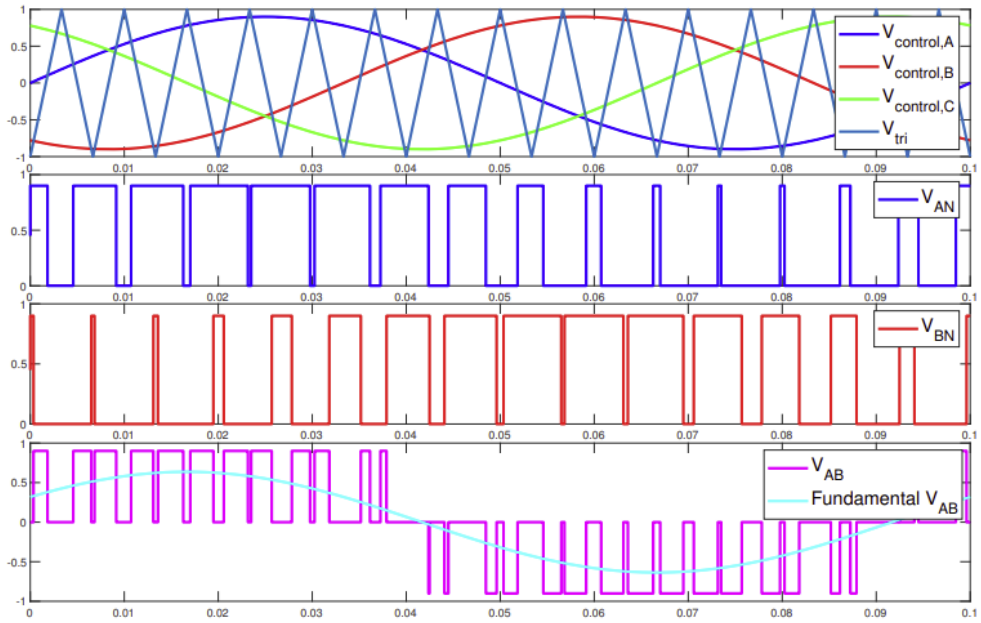

Figure 11: Switching scheme of the VSC [22]

This switching scheme is illustrated in Figure 11. The control signal consists of three signals, equal in amplitude, shifted 120° apart, imitating an AC voltage. Each leg of the VSC corresponds to one control signal such that the switches $S1$ and $S2$ corresponds with $V_{control,A}$ and so forth. In each leg, only one switch can be operated at once. This means that if $V_{control,A} \geq V_{tri}$ then $V_{AN} = V_{DC}$ because $S1$ is closed. Similarly, If $V_{control,A} < V_{tri}$, $V_{AN} = 0$ because the switch at the bottom, $S2$, is on. This creates an output signal where the fundamental component is a sinusoidal wave as shown in Figure 11. The same principle is applied in the other legs of the VSC. As the phases of the control signal is shifted 120° apart, the phases of the output signal will be as well. The output signal shown in Figure 11 contains a large amount of switching harmonics. It is necessary to filter these through an LCL filter to create a waveform that is closer to a sinusoidal waveform. In a LCL filter to inductors are used to smooth out current waveform, while the capacitor removes the harmonics the the voltage waveform.

3.2. Park Transformation

In order to reduce the complexity of the modelling a change of reference frame will be utilized. Traditionally a stationary reference frame, such as the *abc*-frame, is used to describe three-phase voltages and currents. By utilizing Park transformation the reference frame is changed to a rotating reference frame, Direct-Quadrature-Zero (*dq0*). This enables three-phase signals to be represented as DC components. This is done by matching the rotating speed of the reference frame with the frequency of the three-phase signal. In this

way the modelling and control can be done on DC components, which reduces the complexity drastically. The Park's Transformation preserve the amplitude of the electrical components (i.e voltage and currents). However it is a power variant transformation, meaning the do not preserve power computation [36]. The transformation is shown in Equation 12.

$$\begin{bmatrix} i_d \\ i_q \\ i_0 \end{bmatrix} = \frac{2}{3} \begin{bmatrix} \sin\theta & \sin\theta - \frac{2\pi}{3} & \sin\theta + \frac{2\pi}{3} \\ \cos\theta & \cos\theta - \frac{2\pi}{3} & \cos\theta + \frac{2\pi}{3} \\ \frac{1}{2} & \frac{1}{2} & \frac{1}{2} \end{bmatrix} \begin{bmatrix} i_a \\ i_b \\ i_c \end{bmatrix} \tag{12}$$

The Park's Transformation leads to the relation between *abc*-signals and *dq*-signals as shown in Equation 13 and Equation 14

$$|V_{dq}| = V_{LN-PK} = \sqrt{\frac{2}{3}} V_{LL-RMS} \tag{13}$$

$$|I_{dq}| = I_{L-PK} = \sqrt{2} I_{L-RMS} \tag{14}$$

As the transformation is power variant the relation between the stationary frame and rotating is given in the equation below:

$$\begin{aligned} S = P + jQ =& \sqrt{3} V_{LL-RMS} * I^*_{L-RMS} = \sqrt{3}\sqrt{\frac{2}{3}} v_{dq} \frac{i^*_{dq}}{\sqrt{2}} = \frac{3}{2}(v_d + jv_q) * (i_d - ji_q) \\ &= \frac{3}{2}((v_d i_d + v_q i_q) + j(-v_d i_q + v_q i_q)) = \frac{3}{2}(v_d i_d - jv_d i_q) \end{aligned}$$

3.3. Grid following control

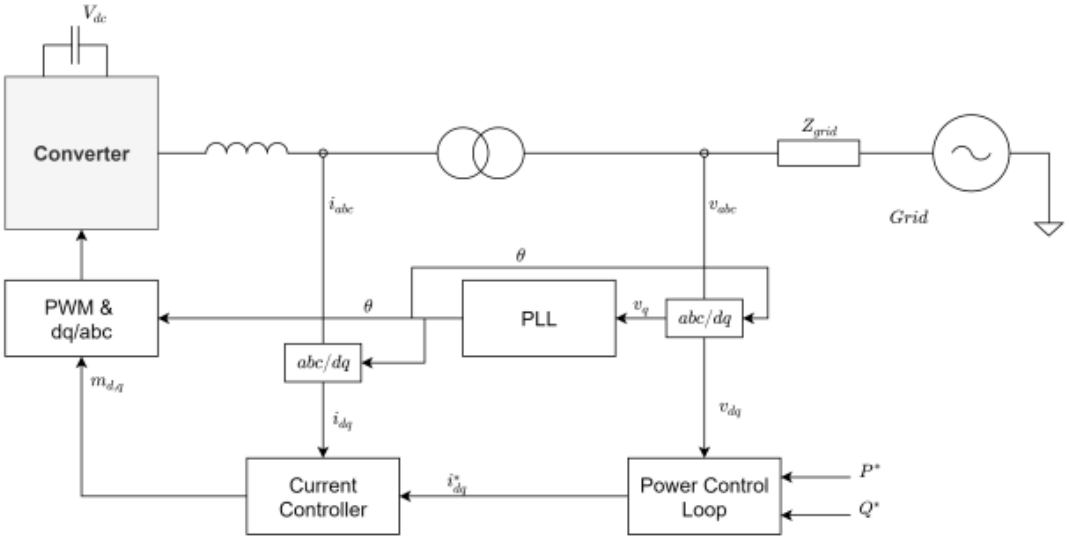

Figure 12: Block diagram of the working principle of grid following control

In a grid-following converter, active and reactive power at the PCC point of common coupling is controlled. The grid-following converter is often considered as a controllable current source because of its working principle. The control of active and reactive power is done through injecting, or drawing, current which is controlled with a specific phase displacement from the grid voltage to get the desired amount of active and reactive power. In order to do so it is therefore necessary to have knowledge of the fundamental frequency phasor of the grid voltage at all time. [39]. This is achieved by implementing a PLL which enables the converter to synchronize to the grid frequency, and therefore inject current with the correct phase displacement. A lack of proper synchronization to the grid will cause the current delivered to be out of phase with the voltage of the grid, which increases the amount of reactive power delivered. The working principle of the grid following control method is illustrated in Figure 12. It follows a cascaded structure with an inner current control loop that controls the current through the filter inductor. The outer control loop is a power controller which controls the amount of active and reactive power feed to the on-board batteries on the passenger ferry and determines the reference values for the inner, faster control loop. At all times the PLL provides the correct position of the grid voltage angle enabling the control loops, as well as the Park's Transformation to work properly.

3.3.1. Phase Locked Loop

For the purpose of this thesis the synchronisation scheme of the phase locked loop is based upon the method described in [34]. The method is based upon utilizing the Park's

Transformation and forcing the q-component of the output voltage to zero. In Equation 15 the power delivered to the grid is shown in the $dq0$-frame. From this it can be seen that this allows the active and reactive power to be controlled only by manipulating the i_d and i_q-components. Hence in order to draw power from the grid, these are controlled to be negative values.

$$s = p + jq = v^{dq} * i^{dq*} = (v_d + jv_q)(i_d - ji_q) \tag{15}$$

The method is based up on introducing a voltage-oriented reference frame, which rotates with the same speed as the grid voltage phase angle. This is illustrated in Figure 13. By aligning the V_d-component of the voltage-oriented reference frame, with the voltage vector of the grid voltage, then $V_q = 0$. This allows the power equation to be simplified as shown in Equation 16

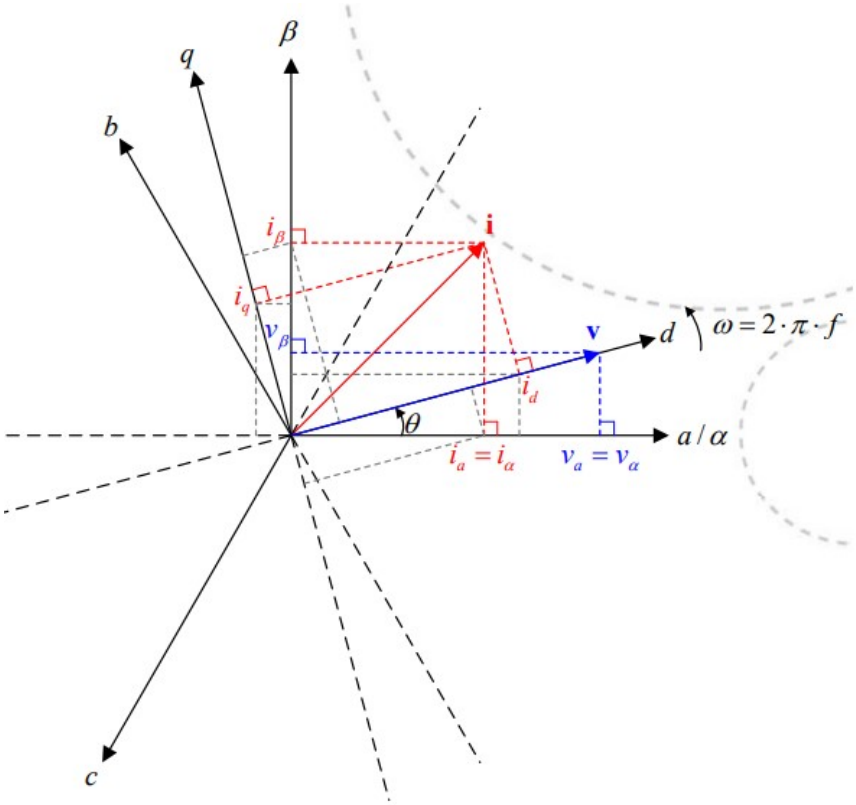

Figure 13: A voltage-oriented reference frame

$$S = v_d i_d + j(-v_d i_q) \tag{16}$$

However the definition of the voltage-oriented reference frame depends on the estimation of the voltage phase angle. The simplest approach of estimating this is by calculating it directly from voltage measurements, however this approach is sensitive to noise and disturbances as well as filtering. [35]. Hence another approach is chosen, where the goal is to minimize the phase angle difference instead. The working principle is illustrated in Figure 14. Here we assume a reference frame with phase angle θ, which is described by Equation 17.

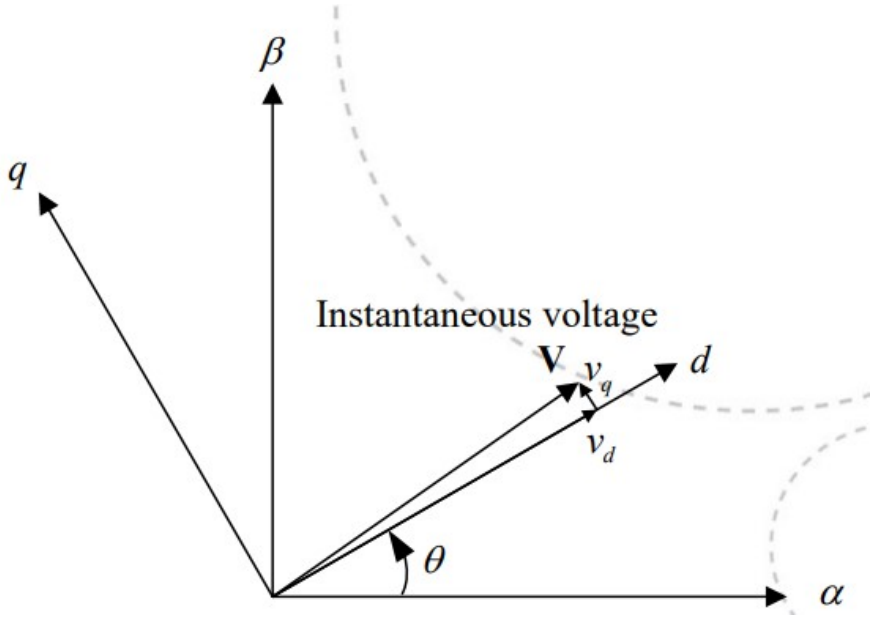

Figure 14: Working principle of the approach chosen [35]

$$v^{dq} = v^{\alpha\beta}\varepsilon^{-}j\Theta \tag{17}$$

A perfect alignment of the reference frame would give $v_q = 0$ and the phase angle error is given by Equation 18.

$$\Delta\theta = \tan^{-1}(\frac{v_q}{v_d}) \tag{18}$$

This allows for an implementation of the PLL as depicted in the block diagram shown in Figure 15.

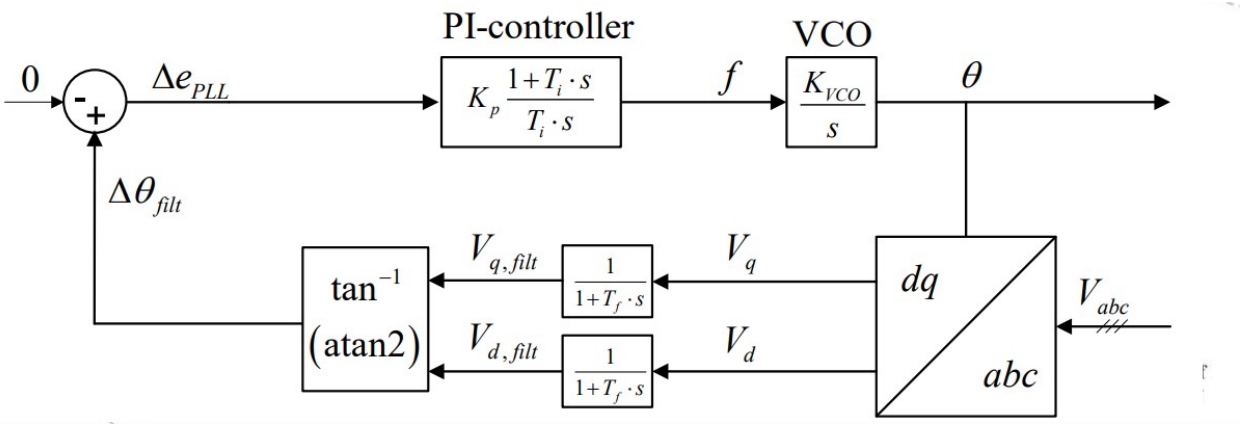

Figure 15: Block diagram of the PLL control system [35]

In Figure 15 a PI-controller is used for estimating the frequency based on the input phase angle error. Here $K_{VCO} = 2\pi$. Voltage filtering is introduced in order to attenuate noise and mitigate harmonics. The inverse tangent function allows accurate detection of the phase angle error in the full angular range, hence it requires a inverse tangent function with 4-quadrant angular detection (atan2) [35].

3.4. Grid forming control

In a grid-forming unit, the magnitude and angle of the voltage at the PCC are controlled. Because of this the grid-forming converter is often considered as a controllable voltage source. The active and reactive powers are therefore regulated such in order to support the voltage and frequency at the PCC. As a consequence, the knowledge of the fundamental frequency phasor of the grid voltage at the point of connection is not strictly necessary. [39]. As apposed to grid-following, in which the concept has been widely accepted, there are several different ways of implementing the grid-forming control depending on the characteristics of the power system it is connected to [27]. The most common implementations are however to make the converter behave like a synchronous machine [18], or to implement droop-control methods [9]. The main benefit of the droop control is that it removes the need for a phase-locked loop, and the stability issues caused by it [28]. Because of this, and that it is the chosen implementation used by Siemens Energy [29], droop-control will be used in this thesis.

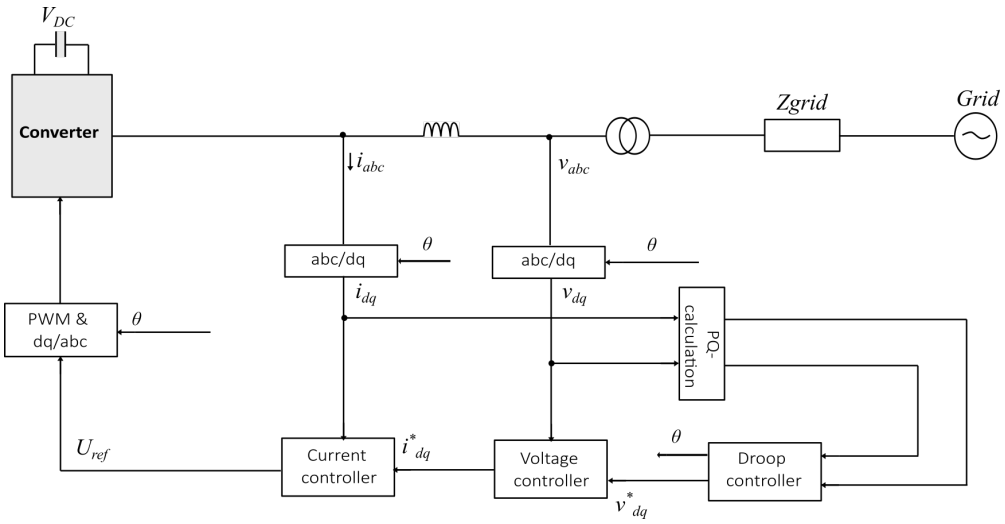

Figure 16: Block diagram of the working principle of grid forming control

The working principle of the grid forming control is illustrated in Figure 16, in which the control system follows a cascaded structure. The outer droop controller compares the measured active and reactive power with the respective set-points, and calculates the frequency and reference values for the voltage control loop. Furthermore the voltage control loop controls the voltage output of the VSC, and provides current references for the inner faster current control loop. Lastly the current controller calculates the current necessary in order to get the desired voltage magnitude at the PCC.

3.4.1. Droop Control

Droop control originates from the principle of power balance in synchronous generators, described by the swing equation, show in Equation B.1. An imbalance between the input mechanical power and the output electrical power causes a change in the rotor speed and electrical frequency. Similarly, variations in output reactive power results in voltage magnitude deviation. Such a characteristic can be artificially created for electronically interface DG distributed generation units, such as the VSC. In droop, the relationship between real power and frequency and reactive power and voltage are as shown in Equation 19 [20]

$$\omega = \omega^* - n_p(P - P^*) \tag{19a}$$
$$V = V^* - m_q(Q - Q^*) \tag{19b}$$

The reactive power is highly dependent of the voltage magnitude V and the active power, P

is strongly dependent on the phase angle δ. As the frequency is proportional to the derivative of the phase angle, the frequency is indirectly controlled. Hence by regulating the active power the frequency is regulated, and by regulating the reactive power, the voltage magnitude is regulated. This concept is utilized in a conventional droop controller. The active and reactive power is measured and compared with set-points, before the frequency and voltage is linearly adjusted through droop coefficients n_p and m_q. This is illustrated in Figure 17.

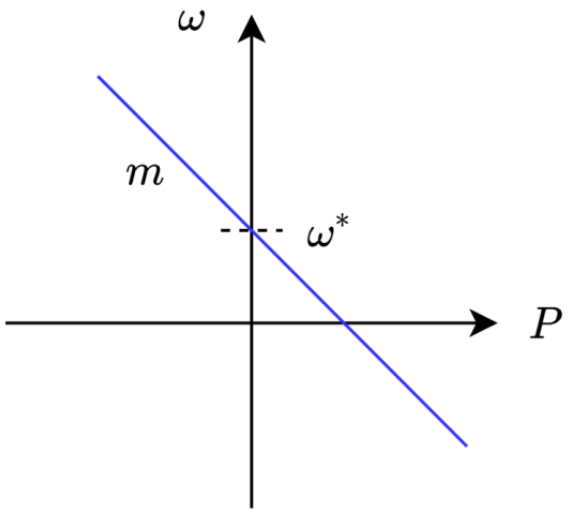

Figure 17: Illustration of the linear relation utilized in droop control in Equation 19

As a VSC seldomly operates completely alone, but rather together with several other VSC as well, it is necessary with some sort of coordination between them. This is also the case for the VSC in this thesis, as it is only one amongst other in the on-board power system of the marine vessel. The way this is solved is by using one of two modes of operation, *mater/slave* or *peer-to-peer* [16]. For the master/slave mode a generating unit takes the role of master unit, which determines the frequency and voltage reference. This reference is communicated to the other generating units, which follows the reference, hence are slaves to the reference. In the peer-to-peer mode, all of the generating units participate an equal amount in the regulation of the voltage and frequency reference. The main disadvantage of this operating mode is that it will cause a voltage and frequency deviation when the load is varied. However it removes the need for communication between the converters, and is therefore the chosen operating mode in this thesis. [16]

3.5. LCL - Filter

As described the output of the VSC contains harmonics due to the switching of semi-conductor switches in order to create alternating signal. It is necessary to filter the

output in order for it to have a sufficient power quality. There are several ways of filtering - both active and passive, however passive filtering is most commonly used for the VSC. There are various typologies for the passive filtering as well [6], however typically a LC or LCL filter is used. The LC filter is able to attenuate 40 dB/Decade at frequencies above its cut off frequency while the LCL filter provides 60 dB/decade [2]. Hence the LCL is chosen for the purpose of this thesis. A single-phase equivalent of the LCL filter is shown in Figure 18. The series resistances, R_c and R_g model the parasitic resistances related to the inductors L_c and L_g. The resistance,R_d, in series with the capacitor, is a damping resistor. This kind of passive damping is often included in the filter as this will reduce the amplification near the filter's resonance frequency. But, it comes with the cost of slightly reduced attenuation as well as giving increased power losses [22].

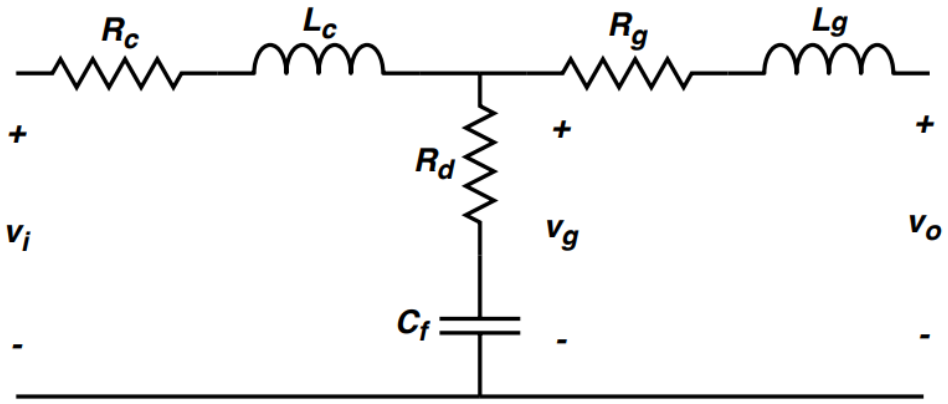

Figure 18: LCL filter at the inverter output

The values of the LCL-filter is chosen with regards to reducing the harmonics around the switching frequency. The values for the parameters is shown in Table 6. In order to attenuate the harmonics around the switching frequency the resonance frequency must be lower than the switching frequency, as well as higher than the grid frequency. A general criterion often used is shown in Equation 20.

$$10 * f_n \leq f_{res,LCL} \leq f_s w \tag{20}$$

The resonance frequency is therefore determined as shown in Equation 21.

$$f_{res} = \frac{1}{10} f_{sw} \tag{21}$$

The open loop transfer function of the LCL filter used is from [13], and shown in Equation 22. Here the resistances are neglected.

$$H_{LCL}(s) = \frac{1}{L_c C_f L_g s^3 + (L_c + L_g)s} \tag{22}$$

Lastly, the capacitor value is calculated as shown in Equation 23.

$$C_f = (\frac{1}{L_c} + \frac{1}{L_g})(\frac{1}{\omega_{res}^2 - \frac{R_c R_g}{L_c L_g}}) \tag{23}$$

4. Modelling of Grid-Forming control

The modelling of the grid-forming control has been inspired by the work done in [22].

4.1. Droop Control

When determining the droop controller coefficients they are selected with regards to quantify how dependent $P - f$ and $Q - V$ should be of each other. In order to do so a maximum and minimum level for both of the frequency and voltage level must be determined. As shown in Table 1 a stationary deviation of 3% and maximum deviation of 5% is allowed. The voltage range is therefore set to ± 0.05 pu. While for the frequency the deviation allowed is 0.02 pu. Hence the minimum and maximum voltage becomes as shown in Equation 24

$$V_{max} = (1 + \Delta V) * V_n \tag{24a}$$
$$V_{min} = (1 - \Delta V) * V_n \tag{24b}$$

Here, V_n is the nominal voltage and the resulting droop coefficient is as shown in Equation 25. The same reasoning is used for the frequency which yields the droop coefficient shown in Equation 26.

$$m_q^* = \frac{V_{max} - V_{min}}{Q_{rated}} \tag{25}$$

$$n_p^* = \frac{\omega_{max} - \omega_{min}}{P_{rated}} \tag{26}$$

However, it is important to take into consideration that there is a transmission line between the VSC and grid. The transmission line will yield a voltage drop across it, and therefore

the droop coefficients are reduced slightly to compensate for this. Yielding the final coefficients shown in Equation 27 and

$$m_q = \frac{\Delta V * V_{max}}{Q_{rated}} \tag{27}$$

The same reasoning is used for the frequency droop coefficient, seen inEquation 28, where the impedance of the transmission line could introduce a substantial shift in the phase angle.

$$n_p = \frac{\Delta \omega * \omega^*}{P_{rated}} \tag{28}$$

The system values used in these calculations are shown in Table 7.

4.2. Voltage Controller

The main purpose of the voltage controller is to regulate the voltage over the capacitor C_f shown in Figure 20. The damping resistor R_g is small compared to the reactance of the capacitor at 50 Hz, and is therefore neglected in the modelling of the voltage controller. In order to simplify the control system the Park's transformation will be utilized, as described in subsection 3.2.

Firstly kirckhoff's law is applied on the electrical circuit in Figure 20. The inverter current i_i is then given by Equation 29.

$$i_i \approx i_o + C_f \frac{dv_g}{dt} \tag{29}$$

Furthermore, by transforming into dq-frame and solving for the capacitor voltage yields Equation 30.

$$C_f \frac{dv_g^d}{dt} - \omega C_f v_g^d = i_i^d - i_0^d \tag{30a}$$

$$C_f \frac{dv_g^q}{dt} - \omega C_f v_g^q = i_i^q - i_0^q \tag{30b}$$

Lastly, Laplace's transformation is used in order to transform the equations into frequency domain, yielding Equation 31.

$$v_g^d = (i_i^d - i_0^d + \omega C_f v_g^q)\frac{1}{sC_f} \tag{31a}$$

$$v_g^q = (i_i^q - i_0^q - \omega C_f v_g^d)\frac{1}{sC_f} \tag{31b}$$

In order to improve the dynamic response of the controller the coupling between the equations, $C_f v_g^{d(/q)}$ is removed through a feed-forward term. By doing so, the voltage can be regulated by using a PI-controller acting on the open loop transfer function in Equation 32. Here K_{pv} and K_{iv} are the proportional and integral gains of the PI voltage regulator.

$$H_{OL,s}(s) = H_{PI,v}(s)H_{sys,v}(s) = (K_{pv} + \frac{K_{iv}}{s})\frac{\frac{1}{C_f}}{s} \tag{32}$$

By combining Equation 30 and Equation 32 the resulting equation is given by Equation 33. This is the modelling equation of the voltage controller. The output of the voltage controller, is on the left side of the equation and is the reference for the inner current controller.

$$i_{ref}^d = i_0^d + (v_{c,ref}^d - v_g^d)(K_{pv} + \frac{K_{iv}}{s}) - v_g^d \omega * C_f \tag{33a}$$

$$i_{ref}^q = i_0^q + (v_{c,ref}^q - v_g^q)(K_{pv} + \frac{K_{iv}}{s}) + v_g^q \omega * C_f \tag{33b}$$

4.3. Tuning of the voltage control

In order to properly tune the voltage controller, i.e determine the gains of the PI-regulator, the method described in [30] as pole placement will be used. The method consists of comparing a second order characteristic polynomial with the closed loop transfer function of the system. The desired response of the characteristic polynomial is then compared with the PI gains, and determined in order to get the desired response and bandwidth from the voltage controller.

The system that is regulated by the PI-controller is given by Equation 34.

$$H_{sys,v}(s) = \frac{\frac{1}{C_f}}{s} \tag{34}$$

The second order polynomial is shown in Equation 35. Here ρ is the damping ratio, and ω_0 is the natural frequency, i.e the frequency the system naturally oscillates in.

$$A(s) = s^2 + 2\rho\omega_0 s + \omega_0^2 \tag{35}$$

For a open loop transfer function $h_0(s)$ the closed loop transfer function becomes $h_{cl}(s) = \frac{h_0(s)}{1+h_0(s)}$. By combining this relation with Equation 32 the closed-loop transfer function of the voltage controller becomes as shown in Equation 36.

$$H_{CL,v}(s) = \frac{H_{OL,v}(s)}{1 + H_{OL,v}(s)} = \frac{s\frac{K_{p,v}}{C_f} + \frac{K_{i,v}}{C_f}}{s^2 + s\frac{K_{p,v}}{C_f} + \frac{K_{i,v}}{C_f}} \tag{36}$$

Lastly, by comparing the denominator in Equation 36 with the second order characteristic polynomial in Equation 35, and solving for the PI-regulator gains they are given as shown in Equation 37.

$$K_{p,v} = 2\rho\omega_{0,v}C_f \tag{37a}$$
$$K_{i,v} = \omega_{0,v}^2 C_f \tag{37b}$$

Here the damping ratio and natural frequency can be designed as wanted. Generally a system is said to be undamped when $\rho = 0$, underdamped when $0 < \rho < 1$, overdamped when $\rho > 1$ and critically damped when $\rho = 1$. [2]. However to get a sufficiently fast damping, as described in [30] the damping ratio is set $\rho = 1.1$ in this case. In order to get a fast response the natural frequency of the voltage controller should be high. However not so high that the voltage controller becomes faster than the inner current controller. Hence a good choice is a decade slower than the natural frequency of the current controller. The natural frequency of the current controller, $\omega_{0,i}$ is determined in an upcoming chapter, and will be described further there. For now the natural frequency of the voltage controller is given as shown in Equation 38.

$$\omega_{0,v} = \frac{\omega_{0,i}}{10} = \frac{3000\pi}{10} = 300\pi \tag{38}$$

4.4. Current Control Loop

The main purpose of the current controller is to regulate the current which flows through the inverter side inductor. This corresponds to the current, i_i shown in Figure 20. As for the design of the voltage controller, dq-frame is utilized here in order to simplify the modelling. Starting off by using kirkchoff's voltage law on the LCL-filter in the electrical circuit in Figure 20 yields Equation 39. Here v_i is the output voltage of the VSC.

$$v_i = R_c i_i + L_c \frac{di_i}{dt} + v_g \tag{39}$$

Furthermore, transforming into dq-frame using Park's transformation and solving for the inductor current yields Equation 40.

$$L_c \frac{di_i^d}{dt} - \omega L_c i_i^q = v_i^d - R_c i_i^d - v_g^d \tag{40a}$$

$$L_c \frac{di_i^q}{dt} + \omega L_c i_i^d = v_i^q - R_c i_i^q - v_g^q \tag{40b}$$

Finally, transforming into the frequency domain by using Laplace's Transformation and dividing by the inductance yields Equation 41.

$$i_i^d = (v_i^d - v_g^d + \omega L_c i_i^q) \frac{\frac{1}{L_c}}{s + \frac{R_c}{L_c}} \tag{41a}$$

$$i_i^q = (v_i^q - v_g^q + \omega L_c i_i^d) \frac{\frac{1}{L_c}}{s + \frac{R_c}{L_c}} \tag{41b}$$

As for the voltage controller, the two axes are coupled together, through $\omega L_c i^d (/q)_i$. These are removed with a feed-forward coupling which enables a faster response. In addition the current can be regulated by using PI-controller acting on the open loop transfer function shown in Equation 42. Here $K_{p,c}$ and $K_{i,c}$ are the proportional and integral gains of the PI current regulator.

$$H_{OL,c}(s) = H_{PI,c}(s) H_{sys,c} = (K_{p,c} + \frac{K_{i,c}}{s}) \frac{\frac{1}{L_c}}{s + \frac{R_c}{L_c}} \tag{42}$$

By combining the relation in Equation 40 with the open loop transfer function in Equation 42, Equation 43 is given. This is the modelling equation of the current controller. On the left side of the equation is the output of the current controller which is the reference signal for the VSC. The inverse Park's transformation is used to change the reference frame back to *abc*-frame before the reference signal is sent to the VSC.

$$v_{ref}^{d} = v_{c}^{d} + (i_{ref}^{d} - i_{i}^{d})(K_{p,c} + \frac{K_{i,c}}{s}) - \omega L_{c} i_{i}^{q} \tag{43a}$$

$$v_{ref}^{q} = v_{c}^{q} + (i_{ref}^{q} - i_{i}^{q})(K_{p,c} + \frac{K_{i,c}}{s}) + \omega L_{c} i_{i}^{d} \tag{43b}$$

4.5. Tuning of the current control

As for the voltage controller pole placement will be used as the tuning method to determine the PI-regulator gains. For the current controller the system that is controlled by the PI-regulator is shown in Equation 44.

$$H_{sys,c} = \frac{\frac{1}{L_c}}{s + \frac{R_c}{L_c}} \tag{44}$$

The closed-loop transfer function of the current controller is found in the same way as for the voltage controller. This yields closed transfer function shown in Equation 45.

$$H_{CL,c}(s) = \frac{H_{OL,c}(s)}{1 + H_{OL,c}(s)} = \frac{\frac{K_{p,c}}{L_c} s + \frac{K_{i,c}}{L_c}}{s^2 + s(\frac{K_{p,c}}{L_c} + \frac{R_c}{L_c}) + \frac{K_{i,c}}{L_c}} \tag{45}$$

Lastly, the PI-regulator gains is determined by comparing the denominator in the closed loop transfer function,Equation 45, with the second order polynomial, Equation 35. This yields the relation shown in Equation 46

$$K_{p,c} = 2\rho\omega_{0,i} L_c - R_c \tag{46a}$$

$$K_{i,c} = \omega_{0,i}^{2} L_c \tag{46b}$$

The damping ratio of the current controller is chosen on the same basis as for the voltage controller. While as for the natural frequency of the current controller this should be as high as possible yielding a fast response. However, not so high that it exceeds the switching frequency of the VSC. This is because this would enable a regulation that is faster than the VSC could handle. The chosen switching frequency used in this thesis is $f_{sw} = 15kHz$ such that the natural frequency of the current controller, $\omega 0, i$ should be sufficiently lower than this. Hence the natural frequency is determined to be a decade lower in order to comply with a fast response, but not too fast. This results in the natural frequency shown in Equation 47.

$$\omega_{0,i} = \frac{2\pi * 15000}{10} = 3000\pi \tag{47}$$

5. Modelling of Grid-following control

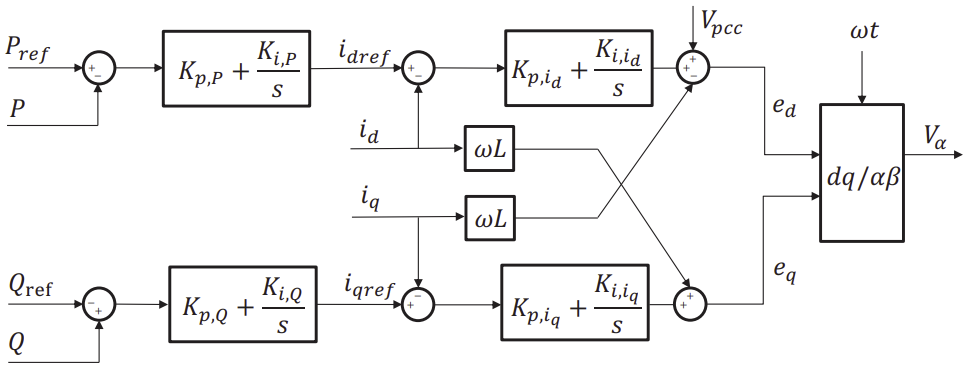

Figure 19: block diagram of the grid following control, and power control loop [4]

In Figure 19 a block diagram of the grid following control is shown. The design and tuning of the current control is equivalent to the current control used in grid-forming, hence this will not be repeated in this chapter. See subsection 4.4 for further explanation. The modelling and tuning of the PLL is done according to [34]. The implementation of the power control loop is done accordingly to [4]

5.1. Phase Locked Loop

Starting with the circuit shown in Figure 15 the system to be controlled is as shown in Equation 48. Also taking the filter into consideration requires modelling of that as well as shown in Equation 49

$$h_{sys,PLL}(s) = \frac{2pi}{s} \tag{48}$$

$$h_{filter_PLL}(s) = \frac{1}{1 + T_f s} \tag{49}$$

Including the PI-regulator, the open loop transfer function of the PLL becomes as shown in Equation 50.

$$h_{OL,PLL}(s) = K_p \frac{1 + T_i s}{T_i s} \frac{2\pi}{s} \frac{1}{1 + T_f s} \tag{50}$$

5.1.1. Tuning of the Phase Locked Loop

The characteristics of the open loop transfer function is suitable for tuning by the symmetrical optimum criterion [34]. The system should be tuned such that the maximum phase angle appears at the crossover frequency. Since the phase characteristics is symmetrical this implies the relation shown in Equation 51, where a is degree of freedom in the tuning and $T_f = 1e - 3s$.

$$T_{i,PLL} = a^2 T_{f,PLL} \tag{51}$$

The maximum phase angle at crossover frequency becomes as shown in Equation 52.

$$\omega_{\varsigma,max} = \frac{1}{a^2 T_{f,PLL}} \tag{52}$$

Solving Equation 50 for K_p evaluated at the maximum phase angle at crossover frequency yields the proportional gain of the PI-regulator shown in Equation 53.

$$K_{p,PLL} = \frac{1}{a 2\pi T_{f,PLL}} \tag{53}$$

Lastly the integral gain of the PI-regulator becomes as shown in Equation 54.

$$K_{i,PLL} = \frac{1}{T_i} \tag{54}$$

For further explanation the reader is refereed to [34] where it is shown that a degree of freedom in the tuning of $a = 3$ corresponds to a damping coefficient of $\rho = 1$.

5.2. Outer control loop - active and reactive power control

In Figure 19 the power control loop is shown. The active and reactive power references are compared with the measured values, before the error margin is minimalized using a PI-regulator. The output of the PI-regulators are the reference values for the inner current controller. The active power creates the reference for the i_d-component and the reactive

power for the i_q-component. As described in subsubsection 3.3.1 the output power are then controlled through the current controller manipulating the i_d-, and i_q-components. The power control loop can therefore be described by Equation 55

$$i_d^{ref} = (K_{p,P} + \frac{K_{i,P}}{s}) * (P_{ref} - P) \tag{55a}$$

$$i_q^{ref} = (K_{p,Q} + \frac{K_{i,Q}}{s}) * (Q_{ref} - Q) \tag{55b}$$

$$\tag{55c}$$

The active and reactive powers are calculated using the measured voltage and current accordingly to Equation 56and Equation 57 respectively.

$$P = \frac{3}{2} * (V_d * I_d + V_q * I_q) \tag{56}$$

$$Q = \frac{3}{2} * (V_q * I_d - V_d * I_q) \tag{57}$$

The tuning is done by applying a marginal step increase and adjusting the PI-controller gains until the response is sufficient.

6. Description of the simulation model

A simplified model of the power system is illustrated in Figure 20. In this model the other power-drawing elements connected to the main dc bus is neglected. The voltage level of the dc bus is regulated by very large batteries such that it remains constant. The grid is connected to the marine vessel through a transmission line Z_{line}, transformer T1 and a shore-to-ship connection which represents the plug-in charging solution.

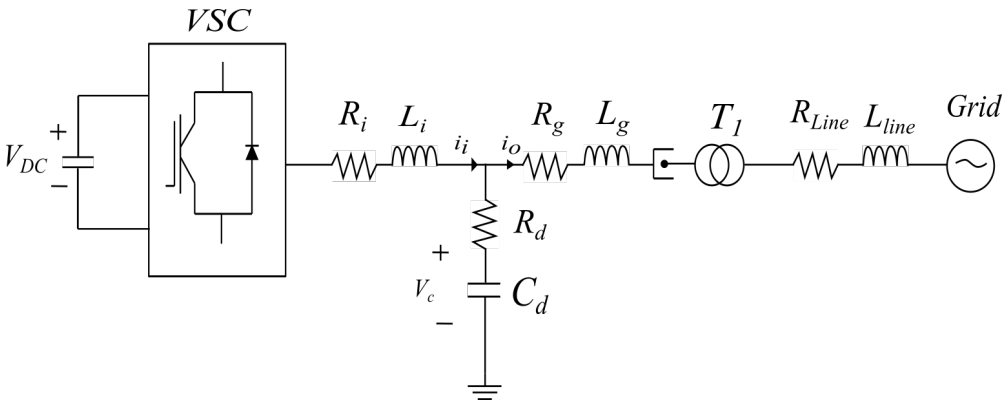

Figure 20: VSC electrical circuit

6.1. System basics

When establishing system parameters the goal was to have as realistic values as possible. They where therefore determined in co-operation with Atle Rygg and Siemens Energy Offshore Marine Center. As the focus in this thesis is on the control and performance of the VSC the base power was chosen to be equal to the rated capacity of the VSC. As there are two voltage levels in the model, the two base voltages are equal to the line-to-line voltages on the high-voltage and low-voltage side of the transformer. This yields the base values as shown in Table 3

Table 3: Base Values

Parameter	Symbol	Value
Base power	S_{base}	1.5 MVA
AC Base voltage (low voltage)	$V_{base,lv}$	690 V
AC Base voltage (high voltage)	$V_{base,hv}$	66 KV
Base impedance (low voltage)	$Z_{base,lv}$	0.3124 Ω
Base impedance (high voltage)	$Z_{base,hv}$	43.56 Ω
Base current (low voltage)	$I_{base,lv}$	1255.1 A
Base current (high voltage)	$I_{base,lv}$	13.12 A
DC base voltage	$V_{base,dc}$	1000 V

6.2. Line parameters and transformer

The passenger ferries are typically in remote places, a significant distance away from the distribution transformer, here represented by the grid. The infrastructure of the grid in these areas are often in worse conditions than more central areas, and the capacity of the grid often close to the limit [32]. This varying grid strength is therefore important to take into consideration, and will therefore be varied in the simulations in order to determine the

impact of it. For the purpose of this thesis, grid strength is the total impedance of the transmission line. For the initial simulations the resistance and reactance of the power line is shown in Table 4. The $\frac{X}{R}$-ratio of power lines are more apparent at increasing voltage levels, as the effect of resistance is decreasing. However, it typically lies between $10-2$ [19]. For the medium voltage level network, with a reduced grid strength, a choice of $\frac{X}{R} = 2\pi$ was chosen. The values of the line where chosen by experimental test. Where they where the smallest values which where large enough to prevent the grid handling the fault independently.

Table 4: Line Parameters

Total impedance	Impedance (pu)
$9\Omega + j18\pi\Omega$	$0.2066 + j1.298$ pu

The transformer is modelled as a lossless transformer in-order to simplify the regulation of the outer-lying impedance in the grid. As there is no difference in the impedance of a transformer or the impedance of a power line when determining the losses this does not compromise the validation of the results.

6.3. Voltage source converter

In this thesis the voltage source converter is modelled as an average model in the simulink environment. This means that the switching scheme described in subsection 3.1 is done internally in the VSC-block. By doing this it removes the need for an generator, signal generator and a comparator, as all of this is done internally. Hence the reference signal out of the control system is sent directly to the VSC, which determines the switching of the semi-conductors by itself. This way of modelling the VSC removes the harmonics introduced by the switching scheme, as well as reduces the complexity of the modelling. This was done as the main purpose of this thesis is to compare to different control modes.
The parameters for the VSC is shown in Table 5. The rated capacity for the VSC is 1.5 MW. The target for the VSC is to be able to deliver the rated active power to the on-board batteries, while controlling the reactive power to 20% of the rated capacity. As the VSC is an average model, the switching frequency is not modelled in the simulink model. However it is used when determining control parameters and is therefore included in Table 5. The values are determined together with the author's co-supervisor, and are typical for Siemens Energy's VSC used in their electrical marine vessels [29]

Table 5: Parameters for the VSC

Parameter	Symbol	Value
DC side voltage	V_{dc}	1000 V
AC side voltage (line-to-line)	V_{ll}	690 V
Rated active power	P_{rated}	1.5 MW
Rated reactive power	Q_{rated}	1.5 MVAr
System Frequency	f	50 Hz
Switching frequency	f_{sw}	15 KHz
Active power set-point	$P_{charging}$	-1.5 MW
Reactive power set-point	$Q_{charging}$	-0.3 MVAr

6.4. LCL-filter

Even though an average model of the VSC removes the harmonics in the output, it is still necessary with a LCL-filter in order to get a sinus-shaped voltage and current. As described in subsection 3.5 the parameter values of the LCL filter is chosen in order to attenuate a desired frequency. This resonance frequency was chosen to be a decade lower than the switching frequency, such that $f_{res,LCL} = 1500hz$. Furthermore the inverter, and grid side inductor values are chosen in co-operation with Siemens Energy. The capacitor value is calculated according to Equation 23, and the results are shown in Table 6.

Table 6: Parameters LCL-filter

Parameter	Symbol	Value
Inverter side inductor	L_i	50 µH
Inverter side resistor	R_i	1 mΩ
Damping resistor	R_d	3.336 mΩ
Damping capacitor	C_d	600µF
Grid side inductor	L_g	30 µH
Grid side resistor	R_g	1 mΩ

As can be seen in Figure 21 the LCL filter has a resonance frequency of 1500 Hz.

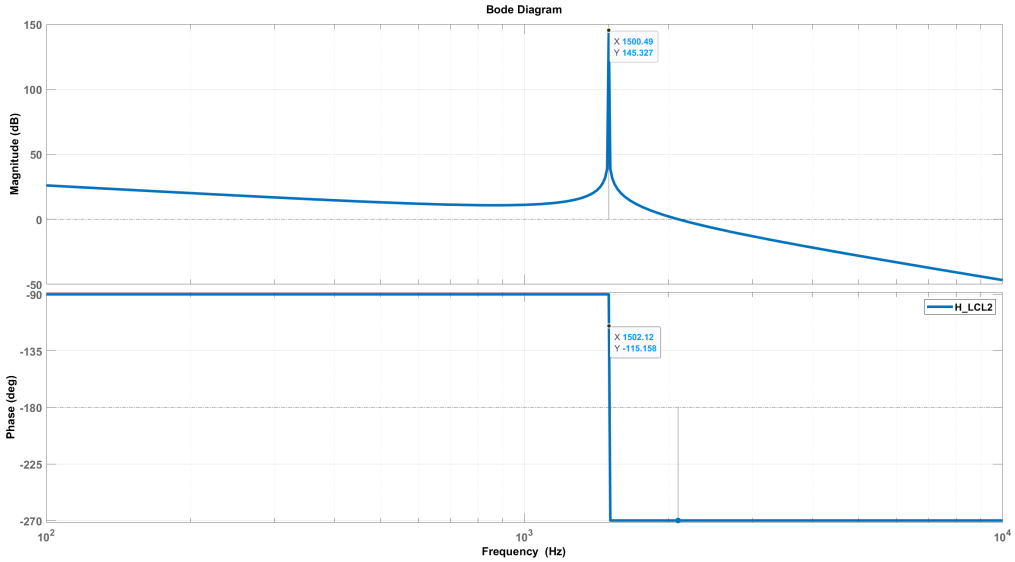

Figure 21: Resonance frequency of the LCL-filter

6.5. Parameters for grid-forming control

For the droop controller the droop coefficients was calculated in per unit values. This means that they are equal to the Δf and ΔV values respectively. Furthermore the PI-regulator gains calculated using pole placement did not yield a satisfactory result, and hence the tuning technique used for the power controller in grid following was applied instead. This implies applying a step in the reference signal and tuning the regulators until a satisfactory performance was achieved. Verification of tuning process is shown in Figure 22 and Figure 23, where a step increase in the reference and corresponding response is shown. The step response for V_q and I_q is shown in the appendix if further validation is of interest.

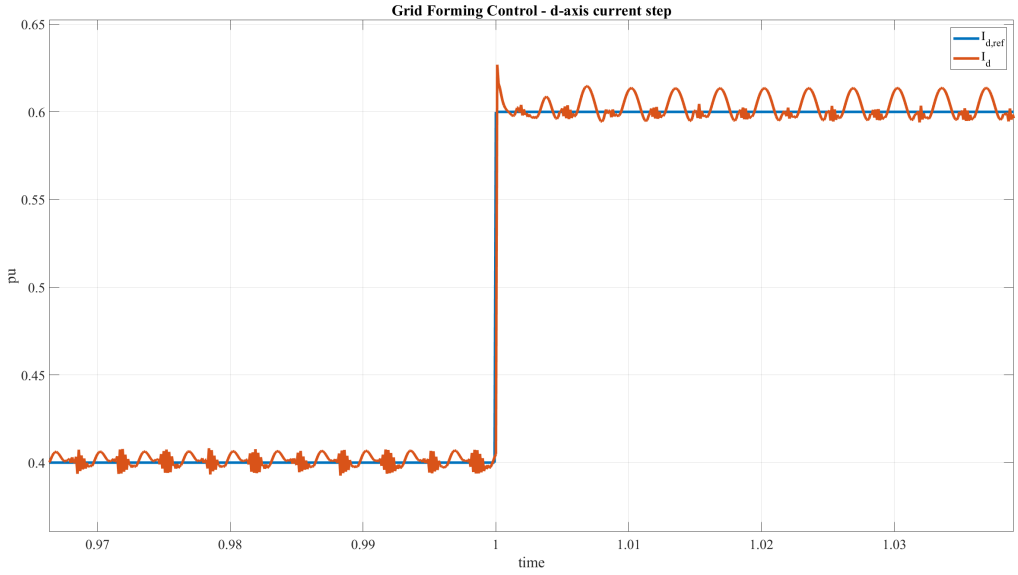

Figure 22: Step increase of 0.2 pu in $I_{d,ref}$ and the response of I_d

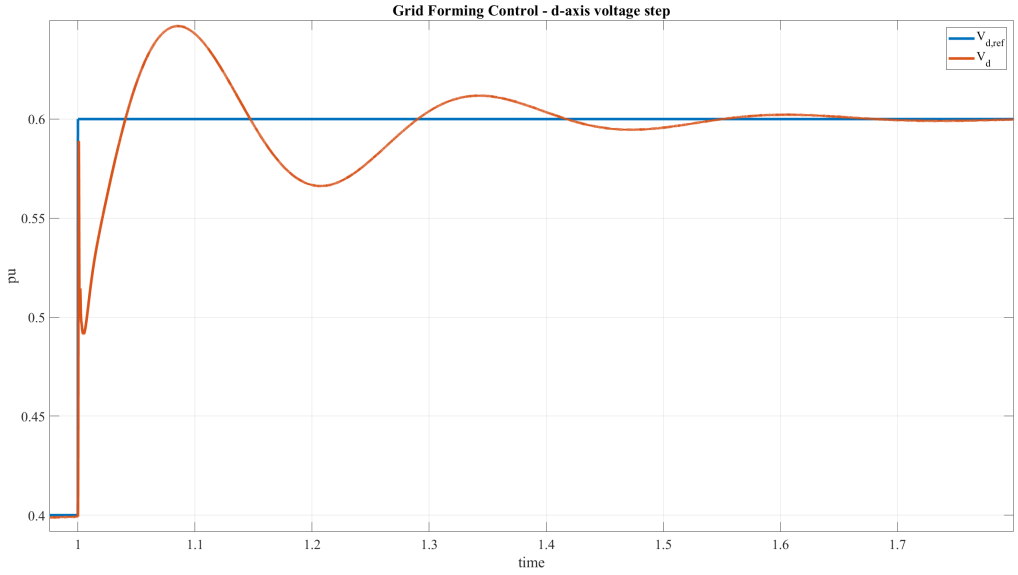

Figure 23: Step increase of 0.2 pu in $V_{d,ref}$ and the response of V_d

The bode plot of the open loop transfer function of the voltage control loop and current loop is shown in Figure 24 and Figure 25. As can be seen the phase margin is 90° at the gain crossover frequency. While the gain margin is infinite as the phase crossover frequency never

occurs. As a rule of thumb the minimum stability requirements is a gain margin of $6dB$ and a phase margin of 45° [2]. This is therefore a stable control loop. The same reasoning yields for the current control loop. However the current controller has a much larger gain crossover frequency enabling a faster inner controller and a cascaded structure.

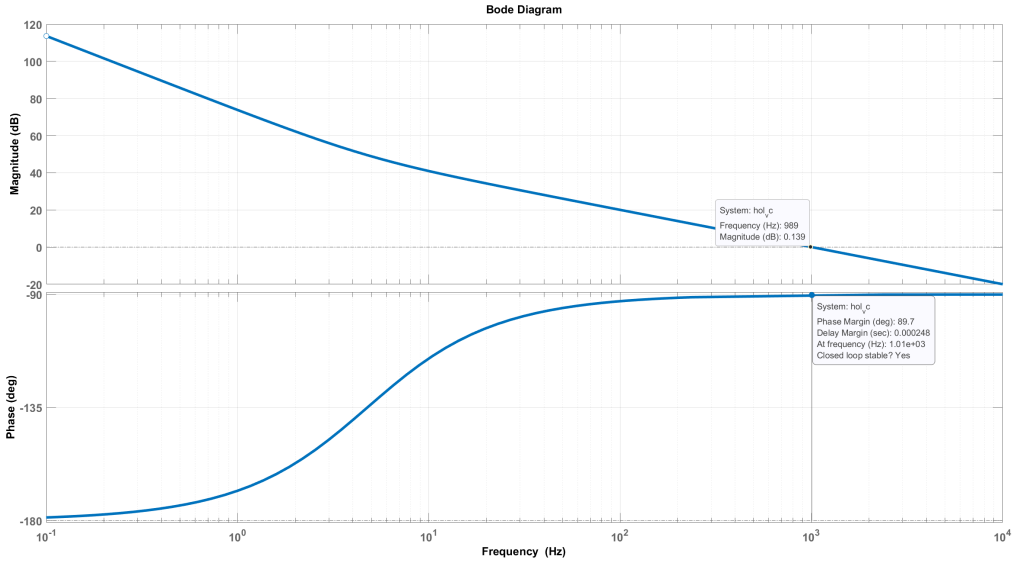

Figure 24: Bode plot of the voltage control loop

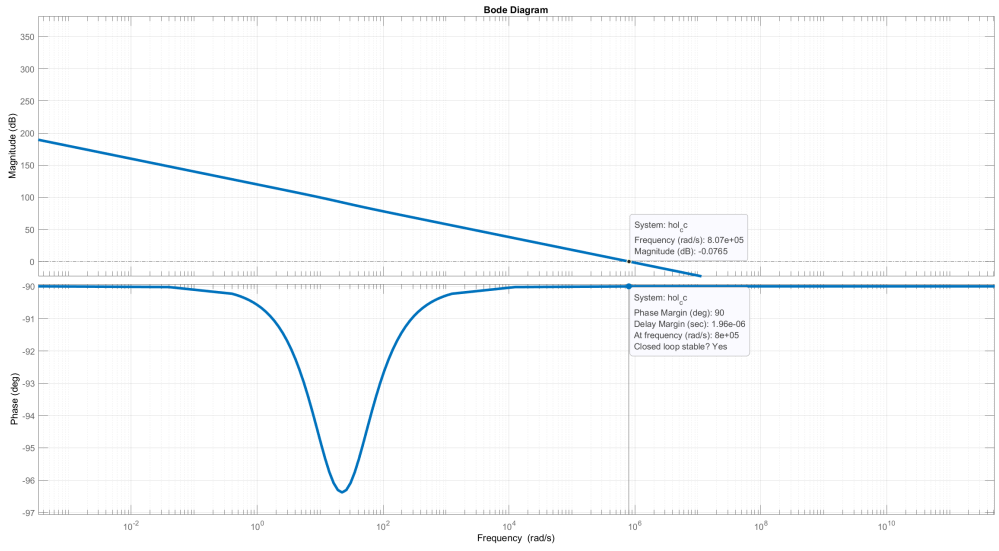

Figure 25: Bode plot of the current control loop

As an important aspect of this thesis is to limit the current out of the VSC during and after a symmetrical fault, it is also necessary to determine the saturation levels for the PI-regulators. This was done by starting off with no limits and then decreasing the saturation limits of the PI-regulators until a satisfactory performance was achieved. During this part it was discovered that the feed-forward term in the voltage controller made it very difficult to reduce the current down to a acceptable value. Hence it was removed in order to get the satisfactory current limitation. This will be further commented in the simulation study. The resulting saturation limits, as well as regulator gains is summarised in Table 7.

Table 7: Parameters for the grid forming control system

Parameter	Symbol	Value
Proportional gain voltage regulator	K_{pv}	20
Integral gain voltage regulator	K_{iv}	600
Proportional gain current regulator	K_{pi}	40
Proportional gain current regulator	K_{ii}	1000
Saturation limits V_d regulator	$PI_{out,vd}$	$\in [0, -3]$
Saturation limits V_q regulator	$PI_{out,vq}$	$\in [1.5, -2.6]$
Saturation limits I_d regulator	$PI_{out,id}$	$\in [5, -5]$
Saturation limits V_q regulator	$PI_{out,iq}$	$\in [6, -5]$

6.6. Parameter for grid-following control

The tuning of the PLL was done according to symmetrical optimum, and the chosen degree of freedom was set to $a = 3$ corresponding to a damping coefficient of $\rho = 1$. This is chosen as it is close to the chosen damping coefficient for the other tuning processes. For the PLL the calculated regulator parameters worked sufficiently. The manual tuning was necessary for the power loop, and the current loop is equal to the one in the grid forming control such that similar gain parameters was sufficient there. A step response for the power and current loop is shown in Figure 26 and Figure 27. Step responses of the rest of the control system is found in the appendix if further validation is wanted.

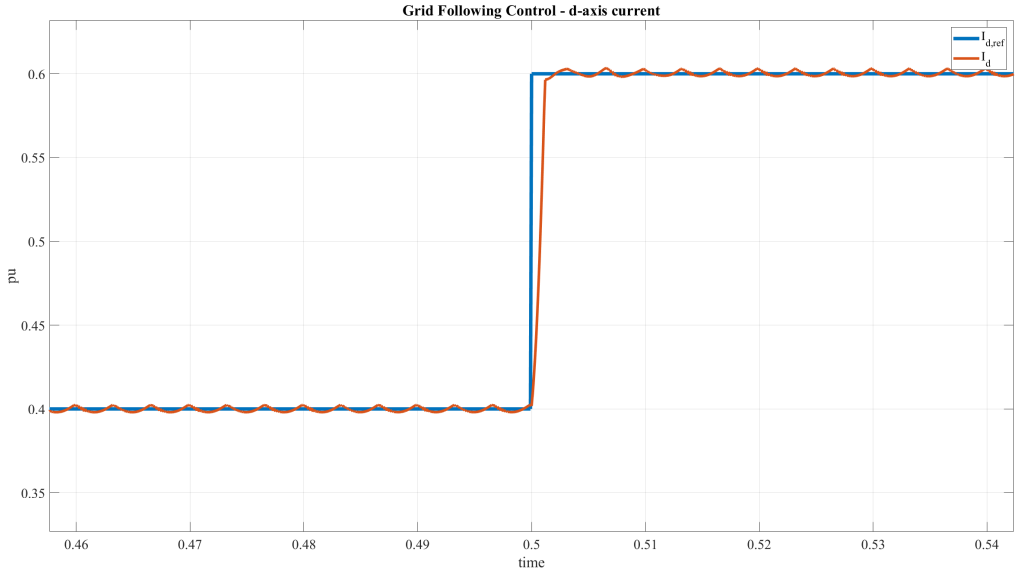

Figure 26: Step response of the d-axis current

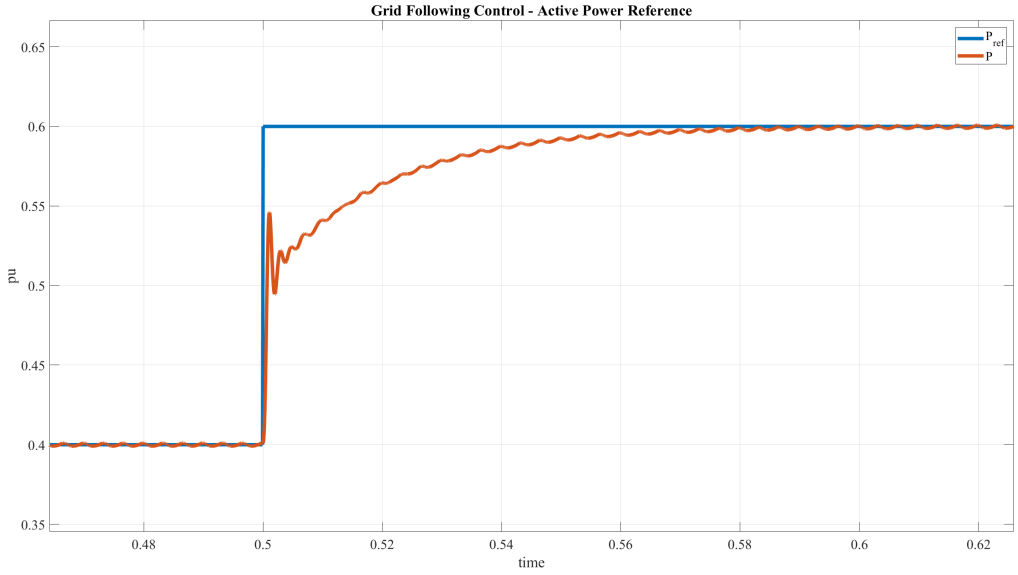

Figure 27: Step response of the active power

For further validation the bode plot of the inner control loop is shown in Figure 28. As for the grid forming current loop, the gain margin is infinite and the phase margin is 90° ensuring a stable control loop. This ensure stable controls as well as a cascade structure,

with the inner current controller much faster than the outer power control. In addition they are both between the LCL filter response and the switching frequency. Furthermore, in order to limit the amplitude of the current during the fault it was sufficient to only limit the output of the regulators in the outer control loop. The summarised grid following parameters are shown in Table 8.

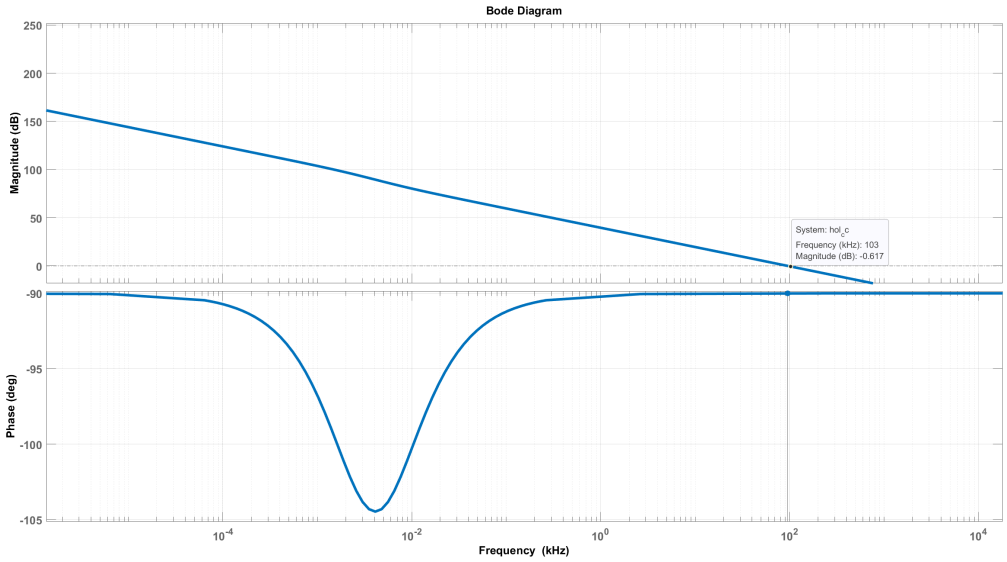

Figure 28: Bode plot of the current control loop

Table 8: Parameters for the grid following control system

Parameter	Symbol	Value
Proportional gain PLL regulator	$K_{p,PLL}$	5.3052
Integral gain PLL regulator	$K_{i,PLL}$	11.111
Proportional gain power regulator	$K_{p,P}$	0.1
Integral gain power regulator	$K_{i,P}$	100
Proportional gain current regulator	$K_{p,I}$	30
Proportional gain current regulator	$K_{i,I}$	1000
Saturation limits P regulator	$PI_{out,P}$	$\in [2, -2]$
Saturation limits Q regulator	$PI_{out,Q}$	$\in [2, -2]$

6.7. Three Phase Symmetrical fault

The three-phase fault is modelled as a bolted fault, being the worst possible scenario that can occur. It is placed on the low voltage side of the transformer modelling a fault near the

charging system, and not in the grid. A model of how the fault is implemented in simulink is shown in Figure 29.

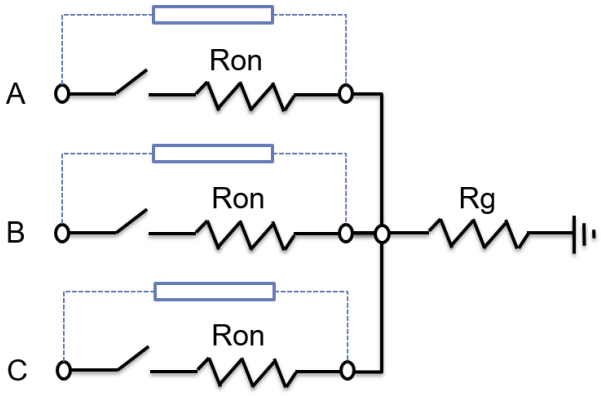

Figure 29: Three-phase bolted fault implementation in simulink [21]

For the initial simulations the fault resistance is $R_{on} = 1m\Omega$, while the ground resistance is set to $R_g = 0.1\Omega$. These will however be varied in the simulation study to determine the capacity and nature of the two different control systems. The resulting fault current then becomes as shown in Equation 58, where $\frac{1}{R_{tot}} = \frac{1}{R_{on}} + \frac{1}{R_g}$. The ground resistance is kept constant during all scenarios.

$$I_{fault} = \frac{V_{fault}}{R_{tot}} \tag{58}$$

The initial simulation is done with a fault that occurs at $t = 1s$ with a clearing time = 100 ms chosen according to [12]. Even though the simulations might be able to handle a very large fault current, in practise equipment will be destroyed. Hence it is necessary to set an operational limit of the fault current for practical reasons. This limitation is done in the PI-regulators by saturating their output. A limit is determined to 200% of the nominal current during steady state, while transients are allowed up to 400% based on [29].

7. Simulation Study

In this chapter the steady-state simulations will be presented and analysed. After that the three-phase bolted fault will be introduced at the low voltage side of the transformer. The response of the two control systems will be presented and compared. Furthermore the fault time and fault impedance will be varied in order to study the effect this has on the control systems. Lastly the impact of the grid impedance will be varied in order to determine what effect this has on the ability of the control systems to handle the fault situation. An

important notice is that during the three-phase fault simulation study it was discovered that the feed-forward term in the voltage control loop of the grid-forming control made it very difficult to reduce the transient current during the fault. When removed, it was possible to limit the current sufficiently. Another solution was to introduce saturation limits on the feed-forward term. Because of this it was interesting to look at the difference in response of the two solutions in the other scenarios as well. This is therefore included as an additional variable during this simulation study.

7.1. Steady-state operation

The steady state current and voltage of the grid-forming converter is presented in Figure 30. While the steady state current and voltage of the grid-following converter is presented in Figure 31. For both the control modes the current achieves a rms value of 1.044 pu, while the voltage has an rms value of 0.982. As can be seen in both cases there are smooth sinusoidal curves with little distortion, resulting in a power quality that is sufficiently good. For the grid-forming converter there was no difference between the scenario with and without feed-forward term with regards to the power quality and steady state values of the voltage and current. The steady state powers and frequency are shown in subsection Appendix C.2.

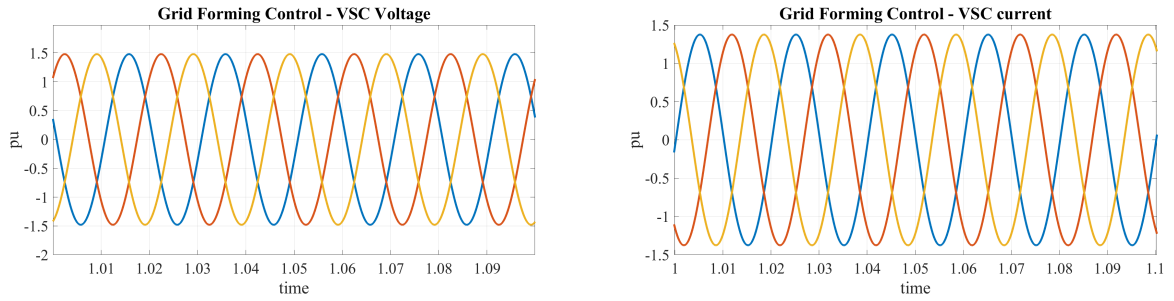

(a) Voltage **(b)** Current

Figure 30: grid-forming converter voltage and Current

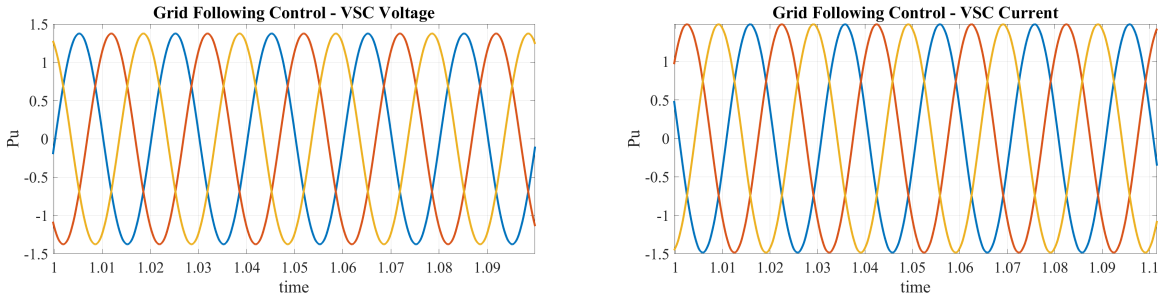

(a) Voltage **(b)** Current

Figure 31: grid-following converter voltage and Current

A good way to validate the steady state performance of the control modes is to introduce a step change, and look at the response. Hence a step reduction in load of 0.3 pu is applied for the reference value of the active power to simulate a change in load demand. Starting with the active power response shown in Figure 32 where the responses of grid-following and the two version of grid-forming control is shown. Here *GRMFF* represents the grid-forming control with feed-forward included. As can be seen the fastest response is from the grid-following control which is expected as this is directly controlled in this control mode. Comparing the two grid-forming control modes it is clear that the feed-forward term enables not only a faster response, but additionally removes the overshoot seen in the response of the grid-forming control without feed-forward.

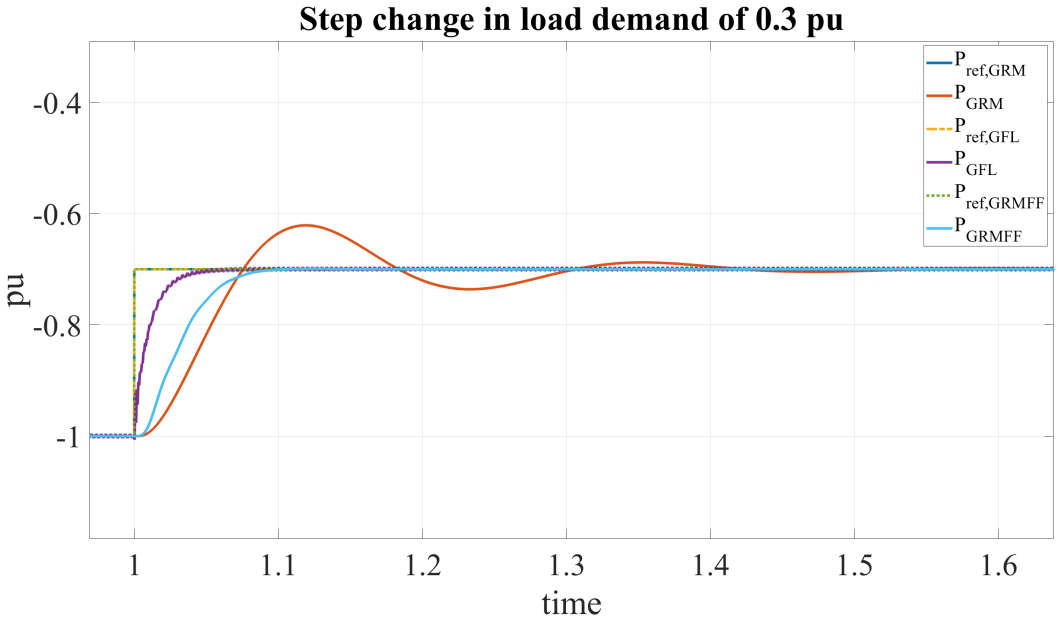

Figure 32: Active power response of step change

Looking at the frequency response shown in Figure 33 some interesting observations can be made. The grid-forming control has a larger offset in amplitude compared to the grid-following control, regardless of feed-forward term. This is unexpected as this is directly controlled by the grid-forming control, and not by the grid-following control. The slower response time of the grid-following control is because the frequency is regulated indirectly through meeting the active power demand. However, the grid-forming converter with feed-forward included performs better with regards to recovery time, and reaches the initial value fastest. Noticeably the grid-forming control without feed-forward performs worse than grid-following control in regards of frequency response.

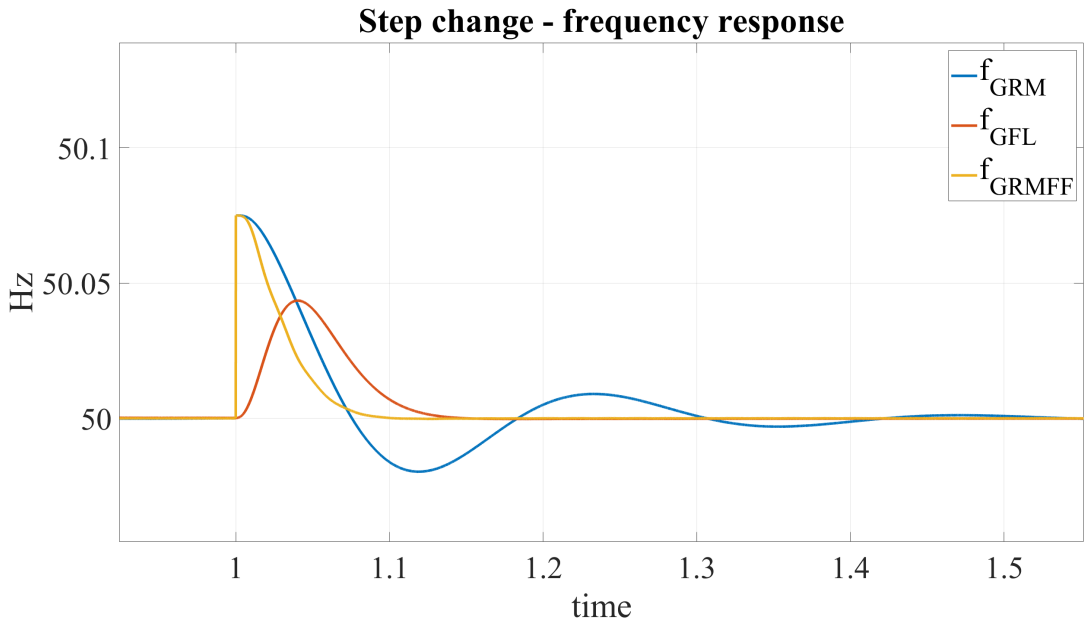

Figure 33: Frequency response to step change in load demand

In Figure 34 the response of the d-axis voltage and current is shown. Here the difference between the control systems are clearly shown as the $V_{d,GFL}$ changes value due to the change in load demand. Less current is drawn from the grid as can be seen in 34a, and a corresponding increase in voltage is shown in 34b for the grid-following control. However the grid-forming control controls the voltage to a preset value, and it returns back to this initial value.

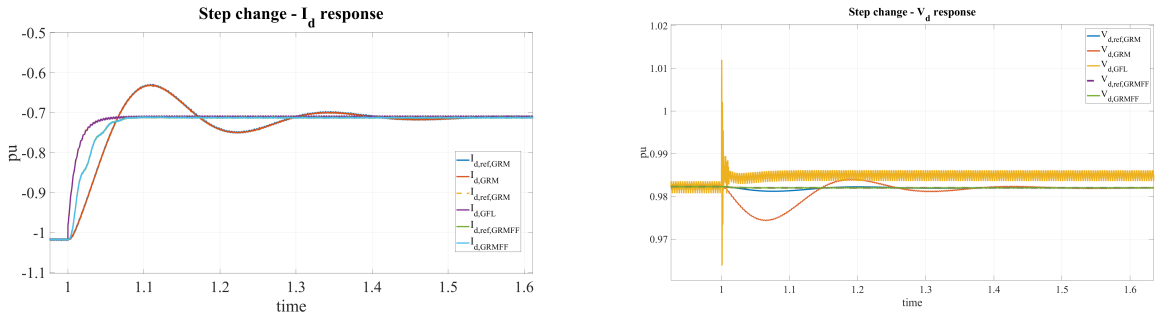

(a) Voltage **(b)** Current

Figure 34: Response of d-axis voltage and current to step change in load demand

As less reactive power losses occur in the transmission line as a result of reduced active power transfer, according to Equation 7, more reactive power must be drawn in order to keep the voltage down at the preset value. This is shown in Figure 35 where it shown that

the grid-forming control increases the amount of current drawn from the grid. Even though the grid-forming converter has a reference value of -0.2, it will be an offset as it shown because of the *peer-to-peer* operation mode.

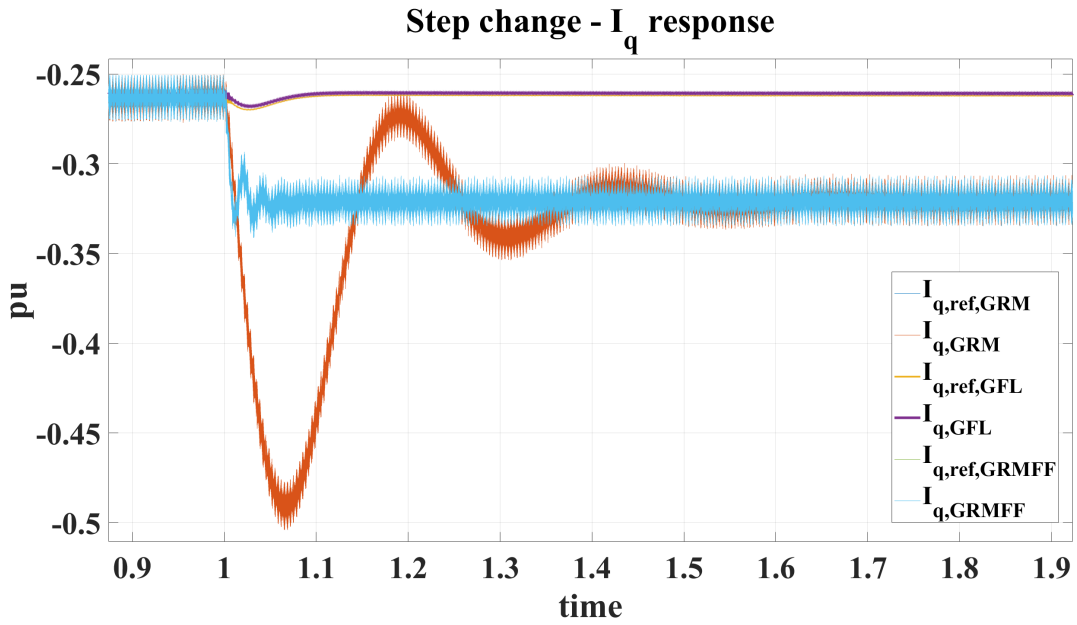

Figure 35: q-axis current response due to load change

The result is that the reactive power is increased as shown in Figure 36, and it differs from the grid-following control as it takes the necessary value to maintain the correct voltage.

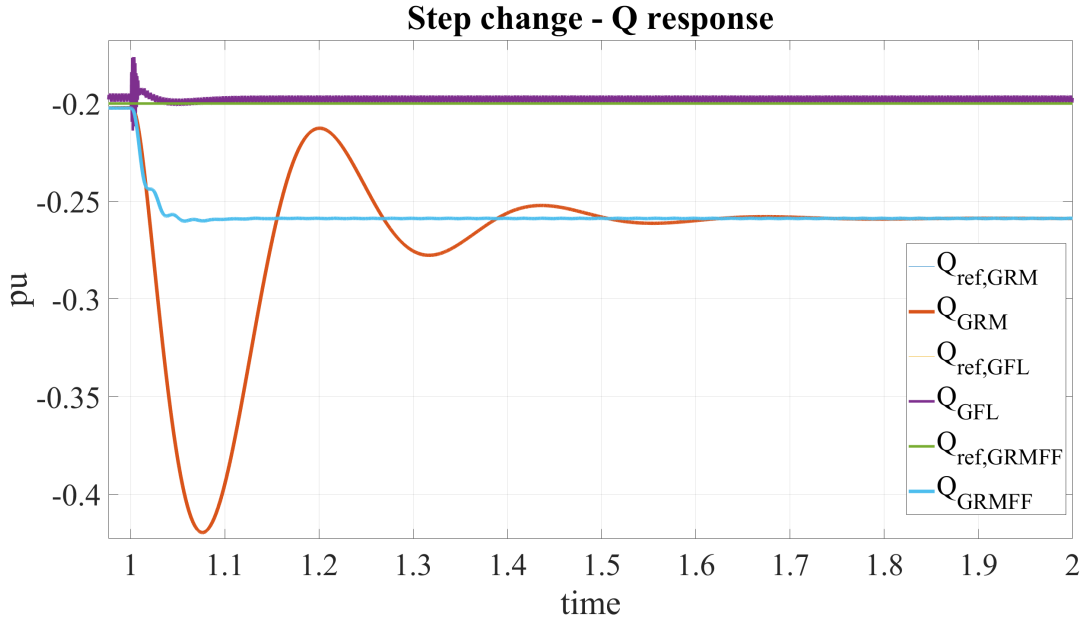

Figure 36: Reactive power response to step change in load

7.2. Three-phase symmetrical fault

Introducing a three-phase symmetrical fault at the low-voltage side of the transformer. The fault will be a bolted fault, in order to determine the worst case scenario as the purpose is to determine the operational limits of the control systems. The power quality during the fault is in all cases insufficient, however it is of more importance how the power quality becomes after recovering, as the fault duration is very short. In Figure 37 the fault current is shown. The decay of the DC-component of the fault current is very fast as the time constant $T = \frac{L}{R} = 0.02$ is very small. Hence the fault current mainly consists of the AC-component during the initial fault scenario. This will however change when line parameters will be varied later in the simulation study.

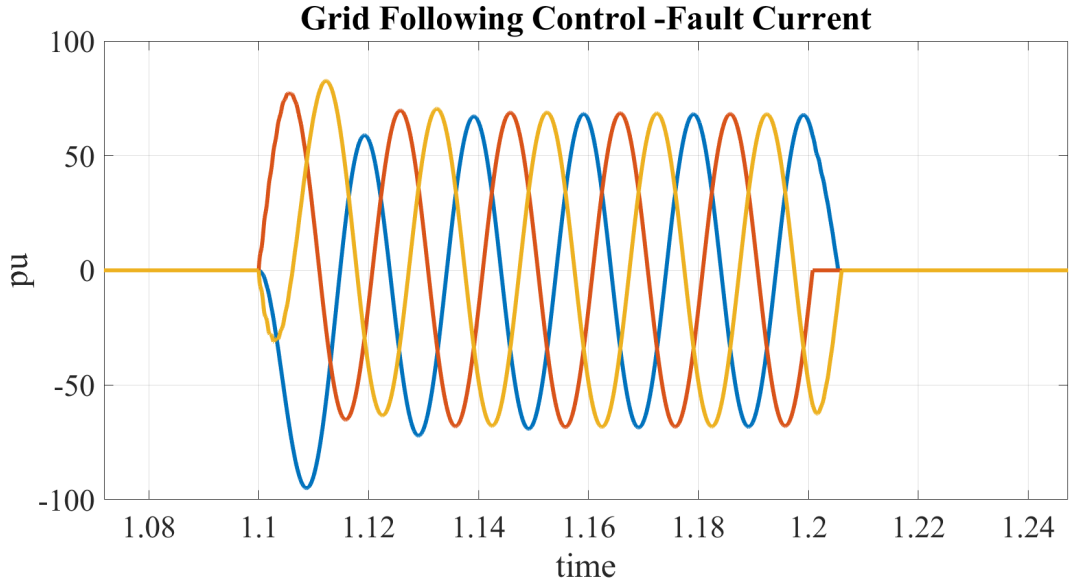

Figure 37: Fault current with initial fault resistance and duration

In order to illustrate the effect of introducing saturation limits on the PI-regulators a simulation without limits is done. The voltage and current of the VSC for the two control systems are shown in Figure 38 and Figure 39. Noticeably, the grid-following converter does not stabilize again, while the grid-forming converter does. However, it falls out of synchronisation and the recovery time is approximately 1.5 seconds. In both cases the voltage and current becomes highly distorted after the fault, and during recovery, such that the power quality is insufficient. This is shown in Figure C.72, where the current and voltages are showed zoomed in. Furthermore the current reaches values which are significantly larger than the practical limits determined to prevent damage of the equipment. For the grid-forming converter this especially happens when fault is cleared and when the system recovers.

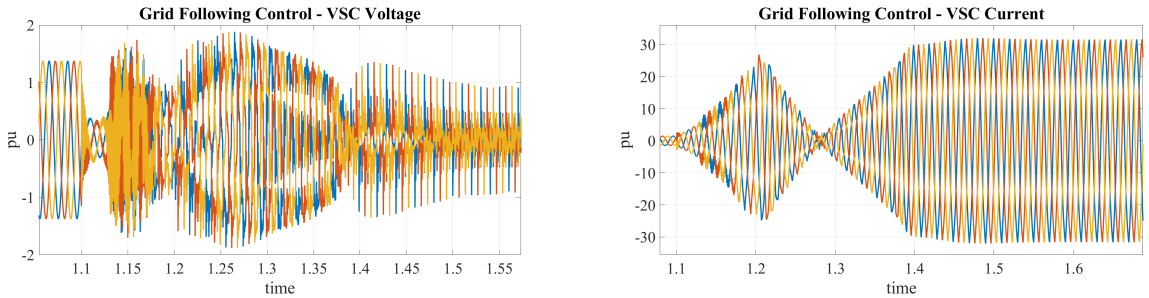

(a) Voltage **(b)** Current

Figure 38: Grid-following converter voltage and current response after fault

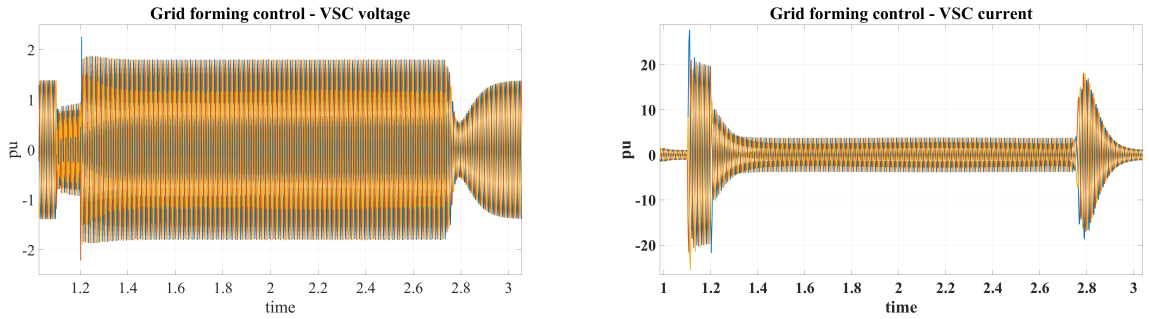

(a) Voltage **(b)** Current

Figure 39: Grid-forming converter voltage and current response after fault

When introducing the saturation limits of the PI-regulators, it was discovered that it was difficult to limit the currents in the grid-forming converter. The high currents during the fault, also visible in 39b, was only slightly reduced when limiting the regulator outputs. It was discovered that the high current during the fault occur because of the nature of the grid-forming converter. When the voltage drops during the fault, the grid-forming converter will draw as much reactive power as possible in order to prevent the voltage from falling further.

A comparison between the reactive power drawn for the grid-forming converter and grid-following is shown in Figure 40. The grid-forming converter will inject approximately 10 times more reactive power than the grid-following converter, in order to prevent the voltage from dropping. It also exceeds the rated capability of the VSC by 700%. Furthermore the effect of the feed-forward term is visible. Here *GRM* represents removing it completely, while *GRMFFLim* represents limiting the current. The reactive power injected in these scenarios are considerably smaller. A drawback of limiting the reactive power is that as the voltage is allowed to drop further, the control system loses synchronization for a longer period. The grid-following converter regains stability a short while after, while the best performing scenario for the grid-forming converter with regards to recovery time is with feed-forward unlimited. Even in this scenario the recovery time is approximately 1.3 seconds longer, and closer to 2 and 2.5 seconds when the feed-forward term is limited or removed.

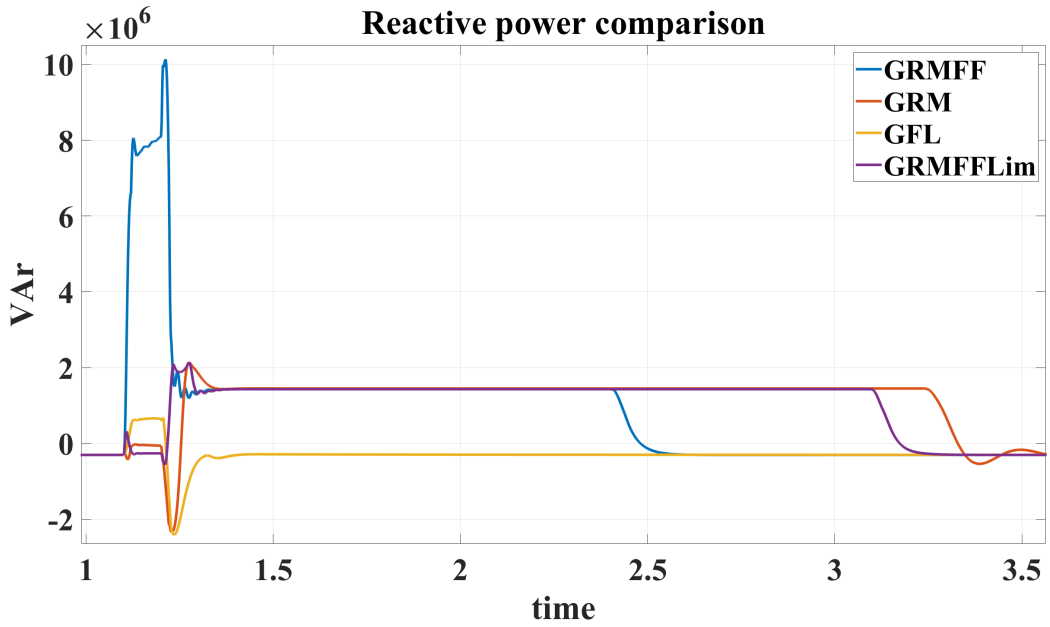

Figure 40: Comparison of reactive power drawn during the fault between GRM and GFL

The effect the feed-forward term has on the current reference determined in the voltage control loop is shown in Figure C.73, in the appendix. After introducing the limits of the regulators, as well as either limiting or removing the feed-forward term the control systems are able to stabilize again. The voltage and current response for the grid-following converter is shown in Figure 41. During the fault the voltage drops to 0.21 pu and when the fault is being cleared a voltage surge occurs. Ignoring the voltage level during the fault, the power quality is sufficient with respect to the grid codes in this scenario. The current increases up to 2.1 pu during the fault, and has a transient during clearing which is not significantly larger. Hence they stay within the practical limits set to protect the equipment for being destroyed.

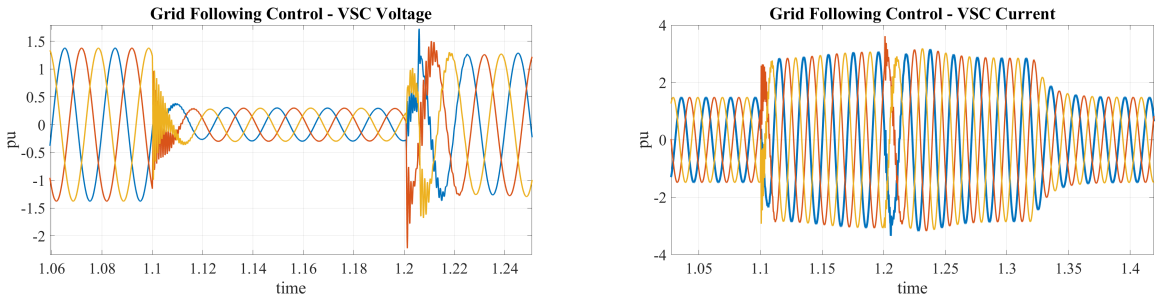

(a) Voltage **(b)** Current

Figure 41: VSC Voltage and current response after fault with limits

For the grid-forming converter without feed-forward the voltage and current is shown in Figure 42 and Figure 43. During the fault the voltage drops to 0.14 pu, before it increases to 1.03 pu during the recovery phase of the fault. During this phase the voltage is highly distorted as shown in 42b. The power quality present during the recovery phase after the fault is not accurately determined, however it is likely that the it is insufficient. The initial response of the current is shown in 43a where the current is limited to 1.55 pu during the fault. When the fault is cleared a surge in the current occurs when the control system tries to recovery. Here the current reaches a transient value of 2.95 pu, sufficient with respect to the limits for transient currents. Approximately 2 s after the fault occurs the system recovers undramastically as shown in 43b.

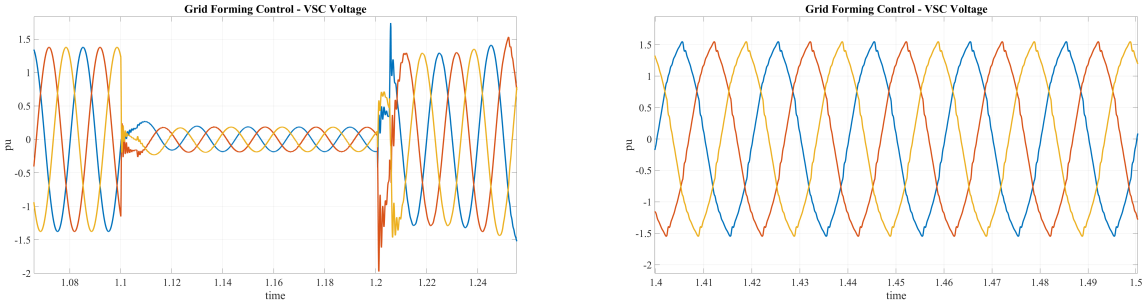

(a) During fault and initial response **(b)** Distorted Voltage

Figure 42: VSC voltage during and after fault with limits

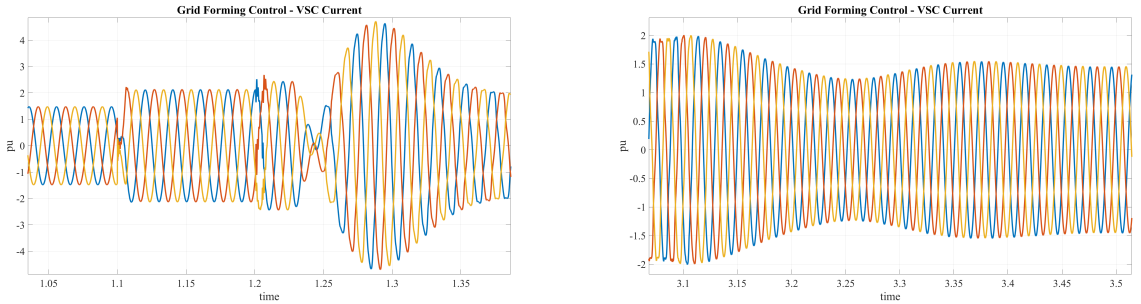

(a) During fault and initial response **(b)** Recovery phase

Figure 43: VSC current during and after fault with limits

Compared with the response when limitations on the feed-forward term is introduced, as shown in Figure 44, the effect of removing the feed-forward term is clear. When clearing the fault the response of the current is more dramatic, as seen in 44b. A large transient current occurs, which has an rms value of 3.65 pu, marginally sufficient with respect to current limitations. However, during the fault the behaviour is quite similar, with the current

limited to 1.7 pu, and the voltage dropping to 0.11 pu. In this scenario the power quality during the recovery phase is also questionable, however it is slightly improved compared to the scenario without feed-forward, in addition to it recovering slightly faster as well. Noticeably, in both grid-forming scenarios the voltage is allowed to drop significantly lower than compared to without any limitations.

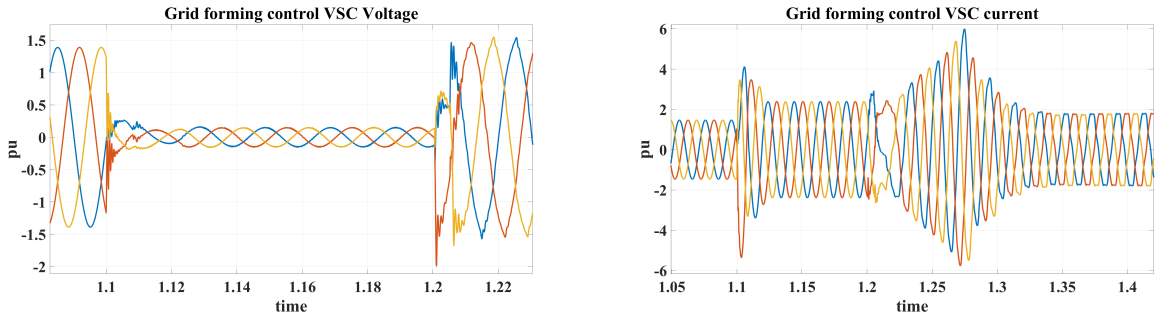

(a) Voltage during the fault

(b) Current during the fault

Figure 44: VSC voltage and current during with limits on feed-forward term

The frequency response of the of the three-phase fault is shown in Figure 45. The main advantage of the grid-forming converter is illustrated here, as it is able to limit the frequency amplitude better than compared to the grid-following converter. In addition, they both recover faster as well. For the grid-following control the frequency decreases down to 48.9 Hz during the fault, before it rapidly increases up to 51.7 Hz after the fault is cleared. With regards to the limits determined in subsection 2.4 this is not an acceptable power quality. Whereas for the grid-forming converter the larges offset is 50.5 Hz and 50.65 Hz. The grid-forming converter with limited feed-forward has a slightly larger frequency offset, however it does recover faster than without the feed-forward term.

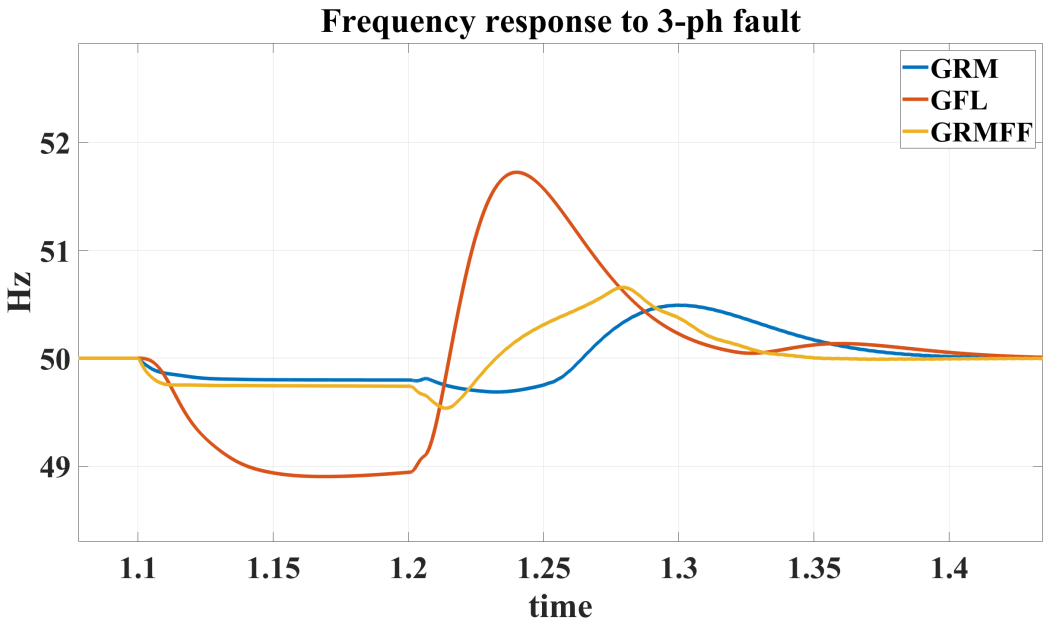

Figure 45: Comparing the frequency response of the control systems

Taking a step back and looking at the overall response of the grid-forming control compared to the grid-following it is clear that the grid-forming control falls out of synchronization. This is seen in the long recovery period of the grid-forming converter shown in Figure 46. In both grid-forming scenarios the regulators loses contact with the reference value after the large decrease in voltage. After clearing they overshoot and stays at a value larger than the preset voltage. It is clear that the control system is out of synchronization because of the large amount of noise in the signal, as well as not following the reference value. The reason it stabilises on a higher voltage value during recovery is because the grid-forming converter still believes the voltage is to low, and injects more reactive power to the grid, as seen in Figure 40 where the reactive power flow changes direction during the recovery phase. The q-axis voltage is shown in Figure C.78, in which both control systems are able to follow the references. This indicates that the performance of the grid-forming converter is limited by the d-axis regulation and the q-axis voltage regulator prevents the grid-forming converter from collapsing.

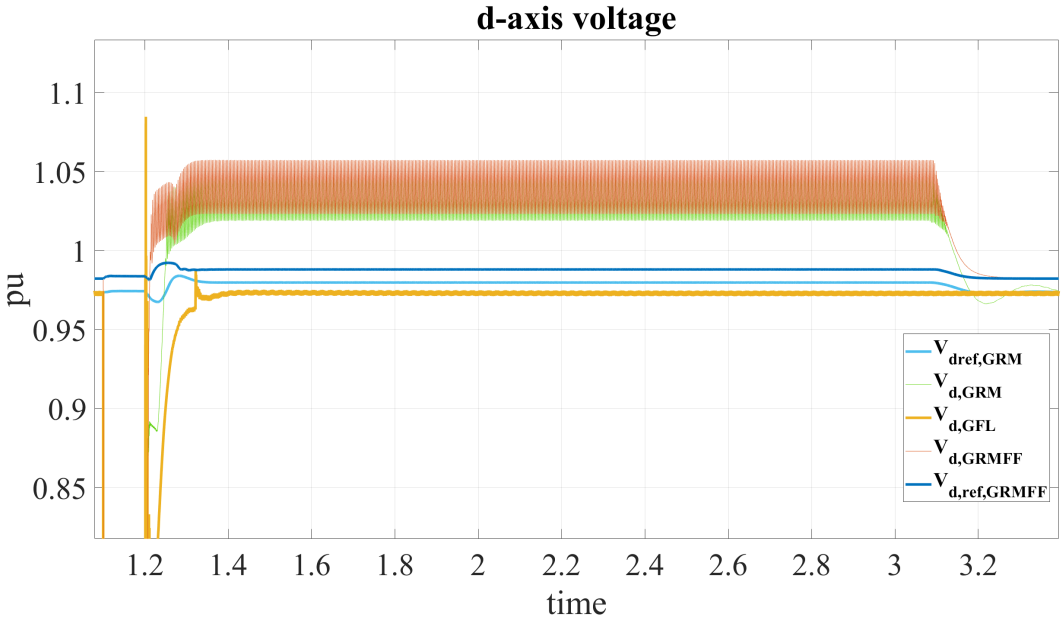

Figure 46: Comparison of V_d during 3ph fault

7.3. Effect of varying the fault duration

The purpose of this study is to determine the critical clearing time of the fault for the two control systems, as well as to quantify the effect increasing fault duration has on the control system response. In order to do so the fault duration will be varied from a very small, unrealistic clearing time to whenever the system is not able to handle the fault, hence determining the critical clearing time. The results shows that the main tendencies are increasing current amplitude when the fault is cleared, as well as a longer recovery phase. This tendency was present in both control systems, and across all three variations.
The difference between them was how sensitive they where to the increasing fault duration. The grid-forming control with limitations on the feed-forward term was the most sensitive. An increase in fault duration of 50 ms, resulted in 1 second longer recovery phase. 47b illustrates the difference in performance between the control systems. With the feed-forward term limited the grid-forming converter was unable to stabilize if the fault duration was 155 ms, yielding a critical clearing time between $150 - 155$ ms for this control method. When the feed-forward term was removed, the critical clearing time was increased up to 320 ms. Whereas for the grid-following control system, a critical clearing time was not established because the system was able to recover during all scenarios. The results above is observed in Figure 47. In 47a the increasing recovery time as well as amplitude after clearing the fault is shown.

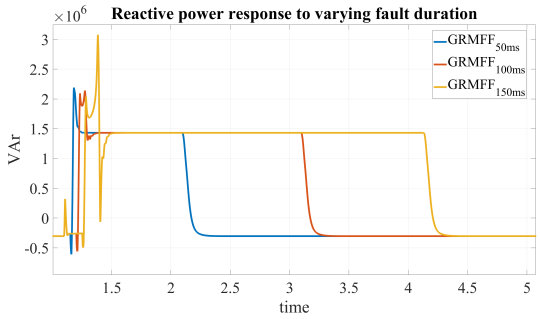

(a) Increasing recovery time and amplitude

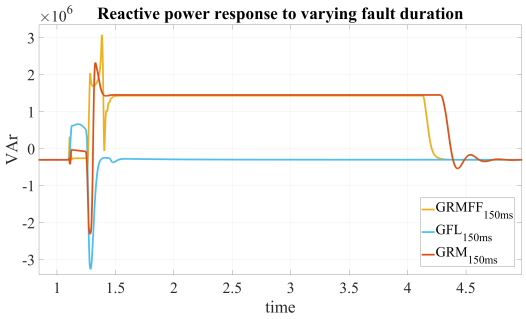

(b) Comparison at $t_{fault} = 150$ms

Figure 47: Reactive power response to increasing fault duration

It is difficult to pinpoint the exact reason for why the grid-forming converter with feed-forward is not able to regain stability when the fault duration is increased from $150 - 155$ ms. With that said, whenever the grid voltage sags during the three-phase fault, the d-axis voltage and current regulators are not able to follow their references, as illustrated in Figure C.77 and Figure 46. Whereas the V_q-component has been able to follow its reference, and still is when the fault duration is 150 ms as shown in Figure 48. When the fault duration increases up to 155 ms it is not able to anymore. As this is vital in regards to calculating the current references to get the correct active and reactive power, it is possible that this causes the converter to fall out of synchronization. This is also what happens when the grid-forming converter without feed-forward falls out of synchronization around 325 ms. Whereas for the grid-following converter, the PLL is able to control the V_q to follow its reference as shown in Figure C.84.

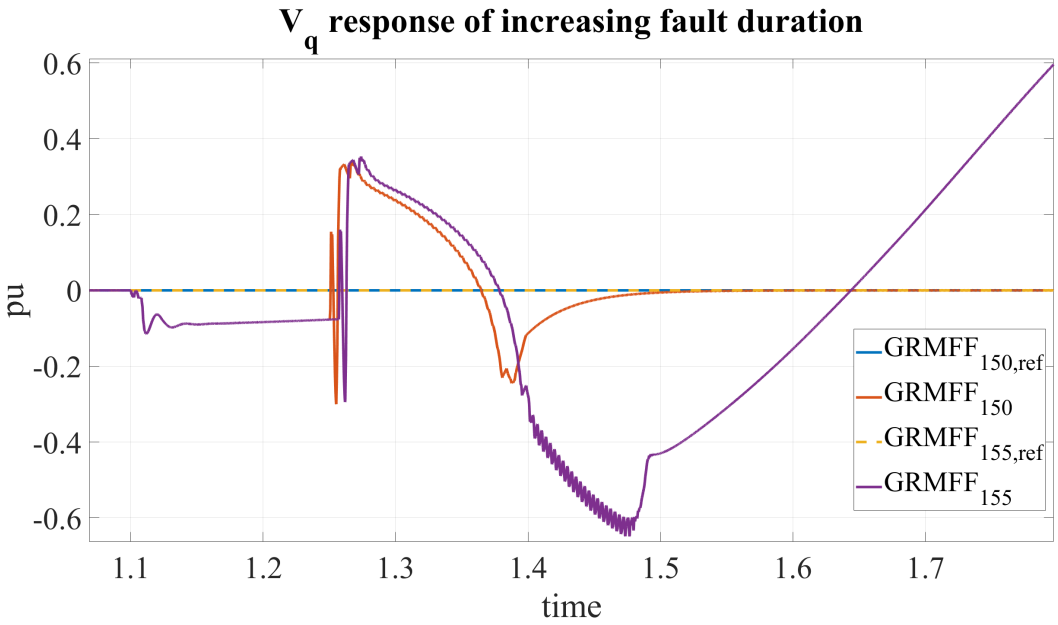

Figure 48: Comparison of the V_q response with increasing fault duration

In Figure 49 the frequency response of increasing fault duration is shown for the three control scenarios. The dashed-line represents the grid-following, dotted-line represents grid-forming with feed-forward and solid-line represents grid-forming without feed-forward. Across all scenarios the same tendency is observed, namely increasing frequency offset. The grid-following control exceeds the power quality limit for frequency when the fault duration is increased above 50 ms. Whereas the grid-forming control with feed-forward does this around 150 ms, keeping in mind that this is very close to its critical clearing time. Without feed-forward the grid-forming converter does not exceed the limit when the fault duration is less than 150 ms.

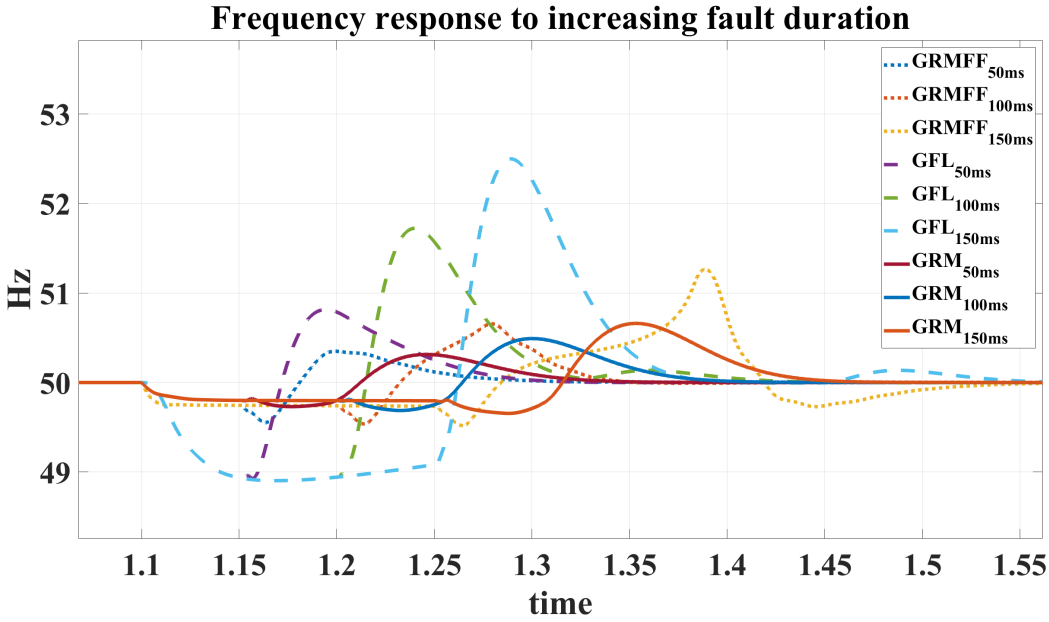

Figure 49: Frequency response of the control modes for increasing fault duration

7.4. Effect of varying the fault resistance

The fault resistance is responsible for the fault current which in order determines the impact on the control systems. The purpose of studying the effect of increasing the fault resistance is to determine what effect it has on the control systems, as well as determining the maximum limit fault current the systems are able to handle. In order to do so the fault impedance will be varied from $10\Omega - 0.01m\Omega$ in order to determine the effect and responses of the two control systems. This will be done with the fault duration kept at the original 100 ms. The different fault resistances and corresponding fault current amplitudes for the two control systems are shown in Table C.9 and Table C.10. During the study it was discovered that the difference between the grid-forming converter with and without feed-forward term was negligible and the outcome equal. They are therefore considered as one control system in this section. Additional simulation results are shown in the appendix.

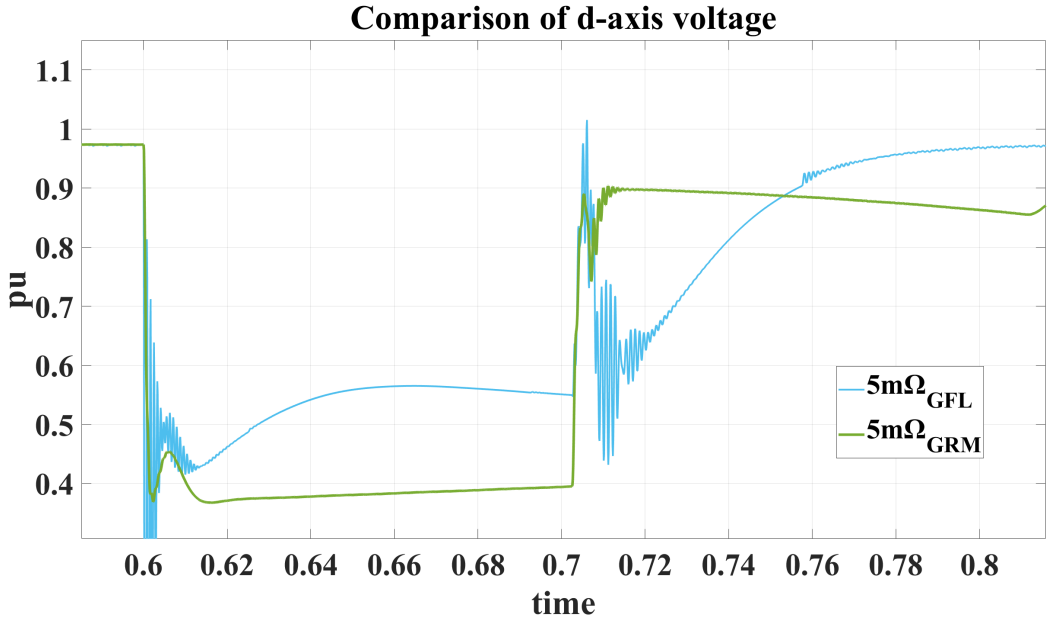

Figure 50: Comparison of d-axis voltage at $R_{fault} = 5\Omega$

The effect of increasing the fault resistance, and hence fault current amplitude, is that the voltage sag increases and that the recovery duration becomes longer. This tendency was equal for both control systems. Still there are some differences, such as how much the given voltage drop is for a given fault current amplitude. As can be seen in Figure 50 the voltage level is at 0.4 pu when a fault resistance of $5m\Omega$ is simulated, whereas for the grid-following converter the voltage level is 0.65 pu. This is opposite of what is expected from the converters, however it is the cost of removing the feed-forward term in the grid-forming converter.
For both control systems a large drop off in voltage level occurs when the fault resistance is reduced further $5m\Omega$. The effect of increasing it further is therefore negligible as the voltage is approximately zero already. Hence the reactive power injected from the converter in to the grid can not increase further. This is shown in Figure 51. Here the increased recovery duration is also shown. Noticeably the largest offset amplitude does not occur for the smallest fault resistance, i.e highest fault current. This also indicates that the converter is saturated at an earlier fault resistance.

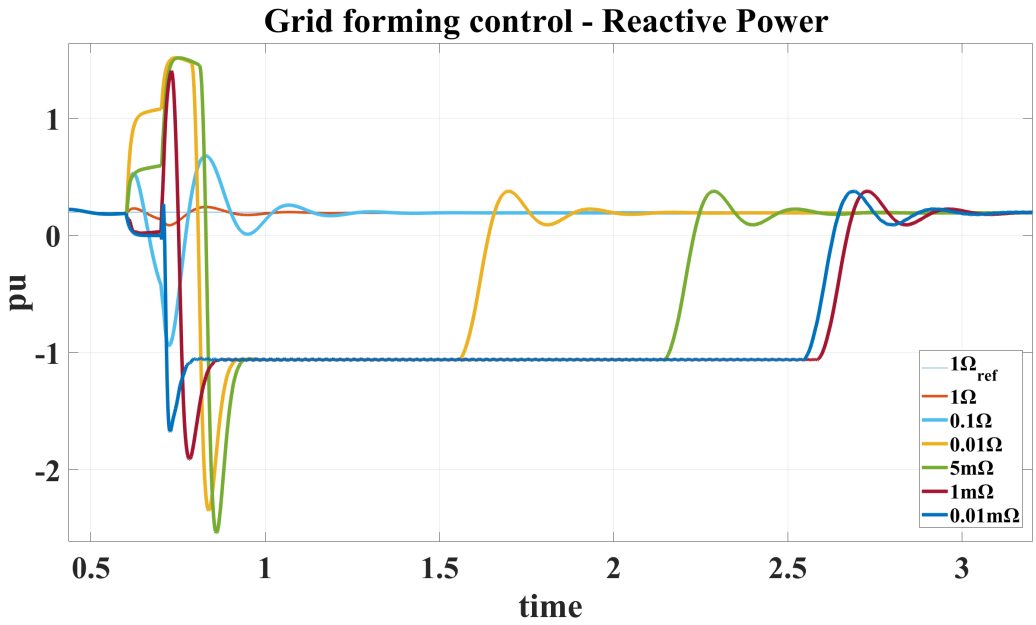

Figure 51: Reactive power response to increasing fault resistance

An interesting observation is that the grid-forming converter is able to keep in contact with the V_d-reference until the fault resistance is lower than 0.1Ω yielding a fault current of 3 pu, Figure C.88. When the fault current is increased above it loses contact, however the V_q-component is able to stay with the reference as shown in Figure C.85. It is able to do so for all of the fault current amplitudes which indicates that for the stability of the control systems, fault duration is more critical than fault amplitude. Another aspect is with regards to power quality. Looking at the frequency responses of the two control systems shown in Figure 52. For the grid-following control the frequency has an insufficient power quality for the four largest fault currents. The power quality is sufficient for the grid-forming control with regards to frequency, however the voltage becomes distorted whenever the fault resistance decreases lower than 0.1Ω. An interesting observation for both control systems is that the largest offset occur in the overshoot, when the systems recover.

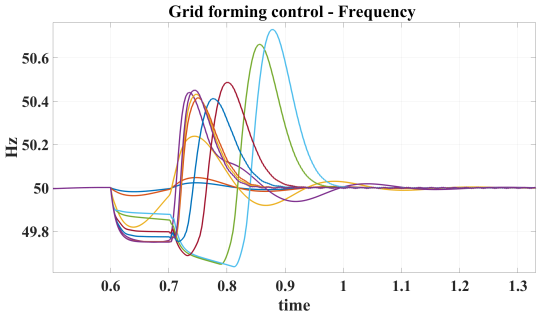

(a) Frequency response grid-forming control

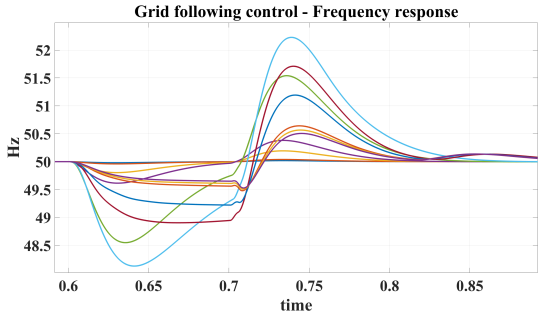

(b) Frequency response grid-following control

Figure 52: Comparison of frequency response to fault resistance

7.5. Effect of varying line impedance

It is of interest to see how the control systems can handle a three-phase fault when the line impedance is increased, simulating a weaker grid. The line impedance will be increased from the initial parameters shown in Table 4. This will be done with the initial fault duration and magnitude. For the effect of varying the line impedance two questions arise as the points of interest. What effect has the varying line impedance on the control systems? In addition, how much is the control system able to handle before a three-phase bolted fault will cause it to collapse? Additional simulation results are shown in the appendix.

7.5.1. Grid-forming control

The line parameters where increased separately in order to determine its maximum capacity. Beginning with the line inductance, when this increases the reactive power losses in the line also increases. Another aspect is that it prevents fast changes in the current, slowing down the dynamic responses of the entire power system. In Figure 53 the reactive power transfer for different line inductances is shown for the converter and grid. As can be seen the the increased losses are covered by the grid-forming converter completely. The converter have to cover the increased losses by itself because the grid is modelled as a stiff voltage source, and can not vary its voltage level. As seen in 53b the changes in reactive power generated is therefore small. As the objective for the grid-forming converter is to maintain the preset voltage level, it does so by manipulating the reactive power flow. In the two lower inductance scenarios the grid-forming converter is still able to draw reactive power from the grid. When the line inductance increases to $1.8H = 12.98$ pu the reactive power losses in the transmission line becomes so large that the voltage at the line bus becomes lower than at the grid-forming converter, at the direction of the reactive power flow changes. At $l_{line} = 5H$ the converter supports the losses in the transmission line with approximately 450 KVAr.

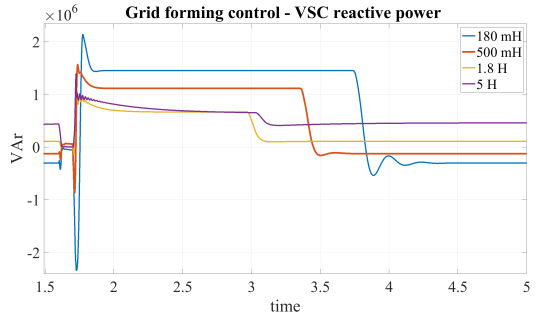

(a) VSC Reactive Power

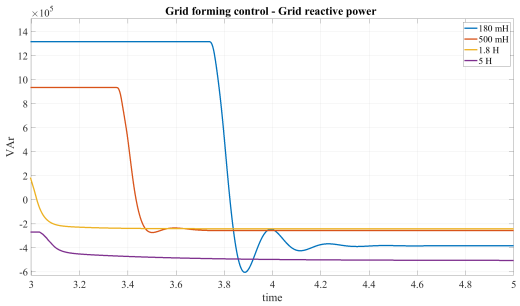

(b) Grid reactive power

Figure 53: Reactive power for different line inductances at different buses

When the fault occurs and the voltage drops the converter will inject reactive power in order to prevent the voltage from falling. The increased reactive power losses in the takes up a larger amount of the reactive power, causing the voltage to drop further as less reactive power is available. This is shown in Figure 54, where the voltage level during the fault is decreasing. The system collapses when the line inductance is increased up to $L_{line} = 9H = 57.7$. At $L_{line} = 8H = 50.48$ pu the reactive power losses in the line are larger than the rated capacity of the converter. At this line inductance the converter is delivering over half of it. When it is increased further, as the grid is not able to cover the losses, this might cause the converter to try and deliver more reactive power than its rated capacity, which is causing the control system to collapse. For the grid-forming converter with limitations on the feed-forward term the performance was significantly poorer than compared to removing it. It was able to stabilize again after up to $1.8H$, and the transient currents after clearing was reduced. However, at $5H$ the system was not able to stabilize pre-fault.

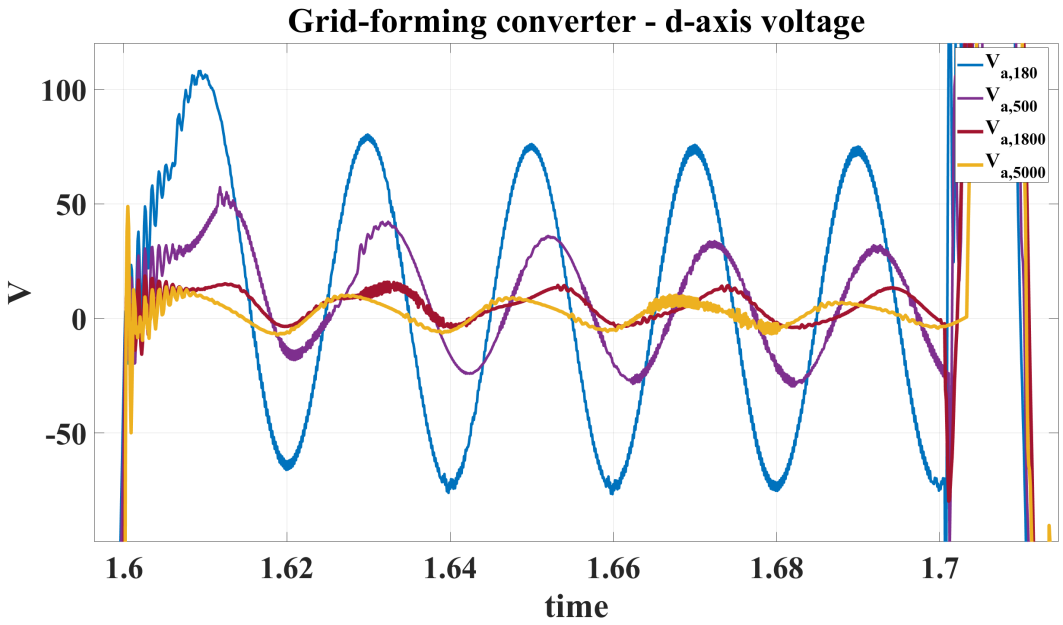

Figure 54: Fault voltage decreasing with increasing line inductance

When the line inductance was kept constant, and the line resistance increased several interesting observations was done. Two clear tendencies was that the effect of increasing the line resistance was an increasing duration of the recovery period, as well as that the transient currents was reduced slightly. Increasing the line resistance also increases the active power loss of the transmission line. As apposed to the reactive power loss, this loss is covered by the grid. As shown in Figure 55. This enables the converter to maintain the active power delivered to the on-board batteries during all scenarios. This is seen in Figure 56. Since the grid is covering the increased losses, the converters response to the fault does not change. As can be seen the active power transferred during the fault is approximately equal for all higher resistance scenarios. An interesting observation is also that with an increasing line resistance, the overshoot after clearing the fault, seen in 56b, is damped. It does so when the line can be said to be purely resistive, as $R_{line} >> X_{line}$.

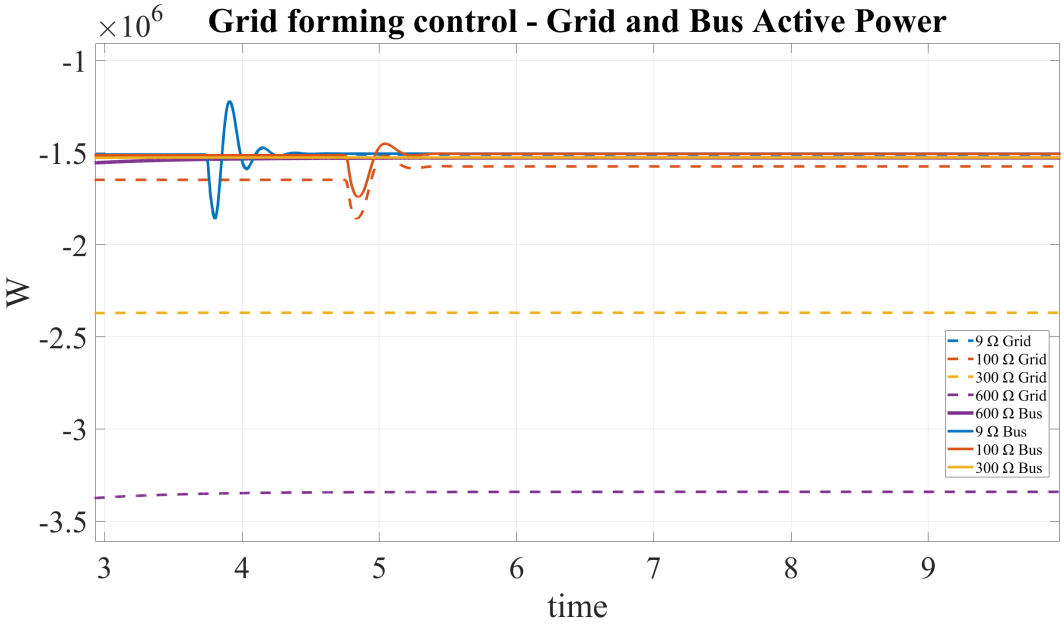

Figure 55: Grid covering the increased losses in the line

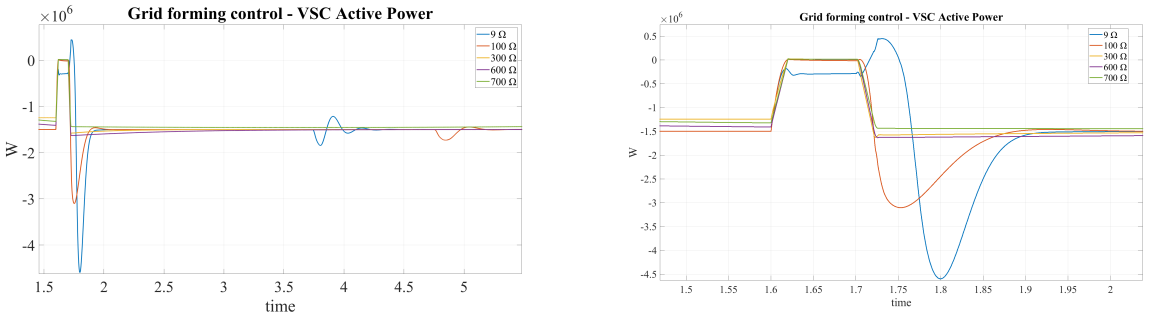

(a) Tendency **(b)** During the fault

Figure 56: VSC Active Power for different line resistances

As described by Equation 7 an increase of real power transfer, will increase the reactive power loss, which will be covered by the converter. As for the case with increasing line inductance, the limiting factor therefore becomes the converters ability to inject reactive power to prevent the voltage for dropping. This is shown in the VSC reactive power in Figure 57 where it is seen that the reactive power changes direction in order to compensate for the increased reactive losses. As can be seen, when the line resistance is increased to 700Ω the system collapses. The change in reactive power can also be seen in the current which is shifted as well as increased in magnitude, Figure C.90
For the grid-forming converter with limitations on the feed-forward term, the performance was generally much worse. Increasing the line resistance to $100\Omega = 2.29$ pu yielded a power

quality which was insufficient with regards to current limitations. Increasing it further, the system was not able to stabilize again.

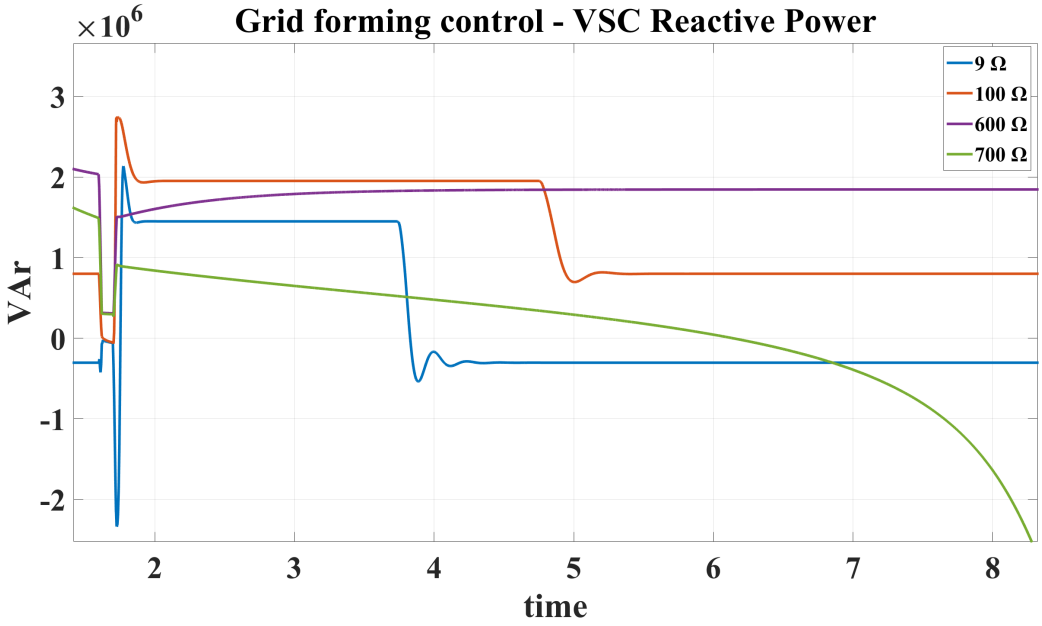

Figure 57: Reduced reactive power transferred to the VSC

7.5.2. Grid-following control

Moving on to the grid-following control system. Increasing the line inductance it became clear that the limitations where not the control systems ability to control the amount of power needed for the losses in the line. However it was the ability to ensure that the voltage and current contained a sufficient power quality. Increasing the line inductance further than $L = 775mH = 5.59$ pu resulted in the current and voltage being to distorted, such that the power quality would be insufficient. It was possible to increase this inductance a bit further by increasing the line resistance, however this was incremental. At the inductance limit this distortion was triggered by the three-phase fault. A single-phase comparison for the voltage is shown in 58a. As it can be seen the voltage at 775 mH contains high frequency oscillations around 650 Hz. This is because the PLL is not able to synchronize with the grid frequency again after the fault occurs. As seen in 58b the signal contains a considerable amount of noise for 775 mH, with a frequency of approximately 650 Hz whereas for 750 mH it is dampened.

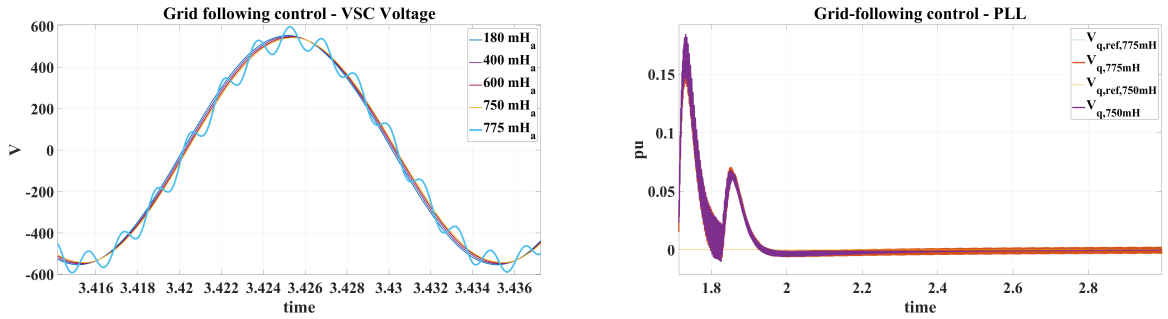

(a) Voltage response **(b)** PLL response

Figure 58: Voltage and PLL response to increasing line impedance

When increasing the line resistance the tendency was similar to the grid-forming converter as the duration of the recovery phase was increased as well. Initially there was no large transient currents when clearing the fault, such that it is difficult to determine the impact it had on this. As for the grid-forming converter the increased line resistance causes this causes increased active loses, as well as reactive losses because of the additional active power transferred. The grid-following converter maintains the power transferred by manipulating the voltage level, as seen in Figure 59. As can be seen the rms value of the voltage decrease with increasing line resistances. A small phase shift can also be observed as a consequence of the increased reactive losses. The reduced voltage level at the converter will cause the converter to try to draw more current to maintain the reactive and active power. For the higher line resistances the current becomes limited by the saturation levels of the regulator, as seen in Figure C.91.

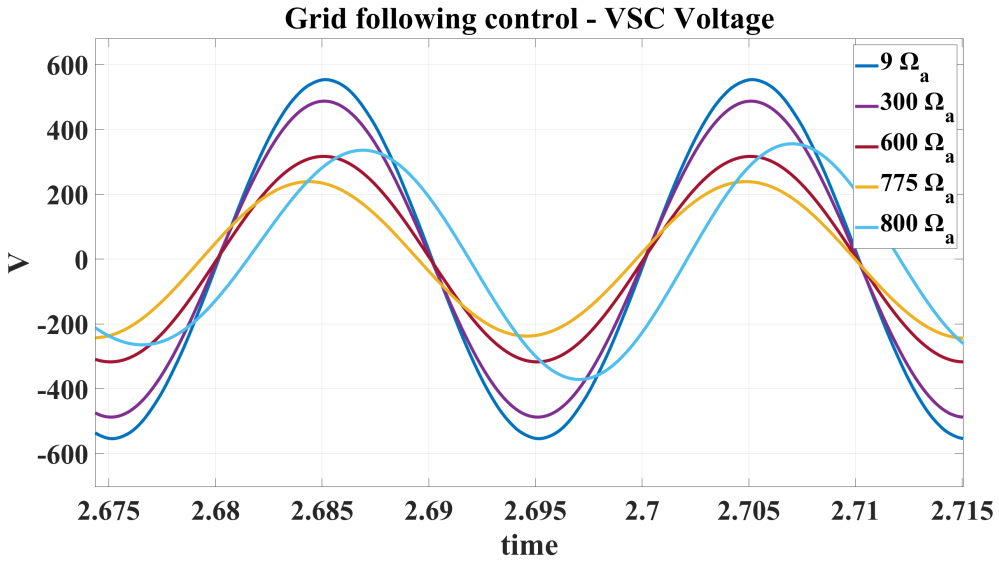

Figure 59: Reduced voltage level with increasing line resistance

In 60b the reactive power is shown. When the line resistance is 600Ω or less the grid-following converter is able to respond and regulate the three-phase fault. An interesting observation is that the grid-following control also get a recovery phase with increasing fault resistance. As for the grid-forming converter, it is the d-axis regulator that loses contact with its reference, while the q-axis regulator is able to follow it, preventing the control system from collapsing. This is shown in Figure C.92. When the line resistance is increased further low frequency oscillations start to occur. This trend is seen in both the active, Figure C.93 and reactive powers. For the 775Ω -scenario, which is marginally stable, the oscillations are dampened, and the control system are able to recover. While at the 800Ω-scenario the control system is not able to dampen the oscillations. These low-frequency oscillations are typical of the grid-following converter in a high impedance grid, and is a known disadvantage. The oscillations are introduced by the regulators in the control system. The regulator gains are now over-tuned as a consequence of the increasing line resistance. The PLL-response to increasing line resistance is shown in 60a in which the oscillations are clearly observed.

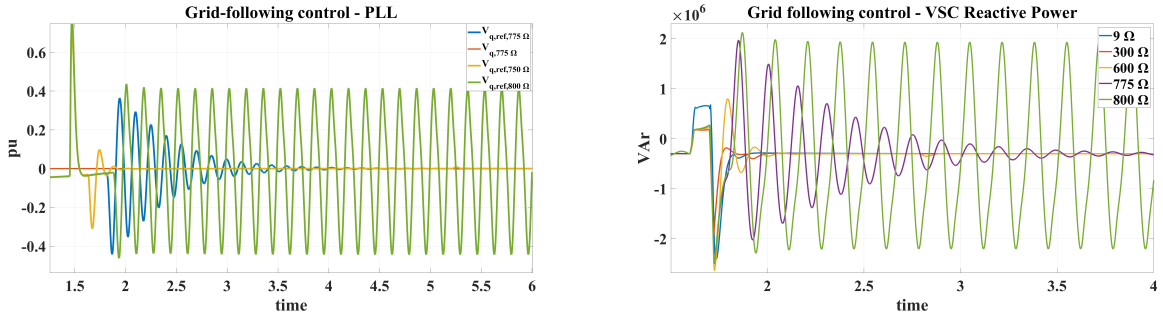

(a) Active Power response

(b) Reactive Power response

Figure 60: VSC Reactive Power and PLL response for different line resistances

8. Discussion

The overall purpose of this thesis was to compare the performance of the grid-forming control of the voltage source converter with the grid-following control of the voltage source converter, especially during a three-phase fault. In order to quantify the performance, different variables where varied in order determine the robustness of the control systems. The grid-following control is the established, and widespread of the two, and its advantages and disadvantages are a fairly established concepts. For the grid-forming control it was a question of whether it was able to handle the same fault scenarios, and if it could out-perform the grid-following control in certain areas. What turned out to be a difficult and complex task was to limit the fault current in the grid-forming converter. This made it naturally to distinguish between the two methods discovered, namely limiting the feed-forward term in the voltage control loop or removing it completely.

The initial steady state simulations illustrated that both are able to ensure a steady state voltage and current with sufficient power quality. Some of the different performance characteristics of the two control modes was outlined when a step change of 0.3 pu in load was applied. GFL control responded fastest, however not outperforming GRMFF considerably. The GRM without feed-forward illustrated the effect of removing this, causing a slower response, as well as an overshoot, which was characteristic throughout the simulation study. The frequency response to the step change illustrated that the GRM is the better option at managing frequency response, because of its working principle, however removing the feed-forward term resulted in a better performance from the grid-following converter. It should be considered that this was an incremental change in load, as seen from the grid point of view. Hence it could have been that the outcome was different if the step change was increased a further. The initial simulations also outlined the difference in working principle between the control modes. As the step change in load resulted in the grid-following converter manipulating the voltage level, in order to maintain the correct reactive power level. Whereas the grid-forming converter manipulated the reactive power flow, in order to maintain the correct voltage level. This also illustrated an underlying issue with droop control with *peer-to-peer* operation of the grid-forming converter. When it operates alone, as it does in these simulations, there will be a deviation when conditions differ from initial conditions.

Introducing the three-phase fault without saturation limits on the regulators highlighted that the grid-following control acts a current source, while the grid-forming converter acts a voltage source. In the way that the grid-forming converter was able to recover by itself, whereas the grid-following was not. With that said neither of the converters performed sufficiently, as the power quality of the grid-forming voltage was insufficient during the recovery phase. In addition this simulation illustrated the devious nature of the grid-forming converter when it comes to three-phase faults, with the large transient currents during the fault and when clearing. As outlined in [37] the grid-forming converter will simply request a current reference such that it prevents the voltage from dropping. Hence without limiting the current references, large reactive currents will be injected as seen in Figure 39 where the peak current amplitude reaches 20 pu. As a result it prevents the voltage from dropping as low as for the grid-following, as seen in 38a. However, the VSC must be protected from over-currents. Initial efforts to limit the fault current through saturation limits of the voltage control regulators outlined that the feed-forward term had a major impact on the current references. It was then discovered that by removing the feed-forward term, or limiting it enabled the fault currents to be limited sufficiently. Hence both options was chosen to be studied in order to quantify the different characteristics of the two solutions.

When the fault currents was limited sufficiently the overall performance of the grid-following converter was still the clearly the best. This was mainly due to the short recovery time compared to the grid-forming variations. In both grid-forming variations the three-phase fault caused the d-axis voltage to lose contact with its reference value, which in turn caused the d-axis current regulator to lose contact with its reference. This is shown in Figure 46.

What prevented the control system for falling completely out of synchronisation might have been that the q-axis voltage regulator was able to follow its reference. By doing this, the modelling premise of ensuring i_q and i_d regulating reactive and active power respectively is kept intact, which might be what enables the system to recover. During this recovery phase the voltage is distorted such that the power quality likely is insufficient. The duration of the recovery phase is slightly less in the case with limitations on the feed-forward term compared to removing it. This might be because some of the properties of the feed-forward term, which is enabling a faster response, is kept even though it is limited. This also correlates with the more dramatic, and faster behaviour of the GRM with feed-forward observed during the fault.
The better frequency control of the grid-forming converter is also illustrated in Figure 45, where both grid-forming variations out-performs the grid-following converter, which strengthen the suspicion of the size of the step change in load being to small.

There was a clear advantage with the grid-following converter compared to the grid-forming converter, regardless feed-forward or not, when it came to the effect of increasing fault duration. The grid-forming converter with limited feed-forward term had a critical clearing time of $t_{crit} \in [150ms, 155ms]$, while the critical clearing time was increased up to $320ms$ when removing the feed-forward term. Whereas the grid-following converter was always able to stabilize again, regardless of clearing time. This result is likely due to the way the grid is modelled as a stiff voltage source, which is largely unaffected by the loss of the load. Hence the grid will always be a voltage source, in which the grid-following converter will be able to synchronize to and act in accordance with. This is not the case in reality, where the grid would have been affected by the loss of the load, and hence a critical clearing time does exist for the grid-following converter. A way to determine it in this model would be to increase the line inductance. This would imitate a weaker connection to the grid, however this changes the premise for the stability assessment, as this would have likely reduced the critical clearing time for the grid-forming converters as well.
It is difficult to pinpoint the exact reason for why the grid-forming converter is not able to stabilize after the fault, nevertheless it was observed that the q-axis voltage regulator lost contact with its reference when the systems became unstable, as seen in Figure 48. It might be that the large transient shown in 47a is the reason why the q-axis voltage regulator loses contact with its reference and causes *GRMFF* to collapse. This would explain why it loses contact much earlier than *GRM* as it has a much more dramatic transient. This would also explain why the grid-following converter never lost contact because the PLL was always able to lock on to the phase angle of the stiff grid voltage.

When studying the effect of the fault resistance, a clear trend is that the impact of the fault size was less critical than the fault duration. This was clear as both control modes was able to stabilize again in all the tested scenarios. Again, this outcome is likely unrealistic and happens because of the way the grid is modelled. Even so it is still useful for looking at the general tendency of the control systems, as well as comparing with the effect of the fault duration. The general trend was that increasing fault resistance resulted in increasing

recovery time as well as increasing the voltage sag. In this case there was little difference between the grid-forming converter with or without feed-forward, however they performed worse than the grid-following converter. Even when looking at the voltage drop for a given fault resistance, the grid-following converter was performing better, which is unexpected but illustrates the large compromise that have to done in order to limit the fault current properly. Interestingly the grid-forming converter lost contact with the d-axis voltage reference when the fault resistance was decreased lower than $0.1\Omega = 0.315pu$, yielding a fault current of 3 pu. The extend of this means that seen from a power quality point of view, the performance of the grid-forming converter is insufficient if the fault current is increased above this. Whereas in 52b it can be seen that the power quality of the grid-following converter becomes insufficient for the four largest fault currents, indicating a much better performance.

Lastly, when the effect of the varying line impedance was studied it was chosen to vary the line parameters separately in order to determine the maximum capacity for each parameter, in stead of determining a maximum capacity for both at the same time. The argument for doing this is that in this thesis it is more important to quantify the effect of increasing line inductance, or line resistance, rather than determining the maximum capacity of the line which will be a product of both.
For the grid-forming converter there was a significant difference between the performance of the two variations. The converter with feed-forward term limited was able to stabilize after the fault with a line reactance of $X_{line} = 12.98$. Increasing it further resulted in a distorted pre-fault voltage, i.e insufficient performance during steady state as well. The effect of increasing the line inductance for the grid-forming converter was that it had to cover the increased reactive losses in the line independently. This is likely due to how the grid is modelled as a stiff voltage source, with a given voltage level which prevents it from responding to increased reactive losses. The result of this was that reactive power had to be injected to the grid, rather than drawn to the on-board batteries when the line reactance was increased above $X_{line} = 12.98$. The increased reactive losses also resulted in less reactive power available for maintaining the voltage level during the fault, which can be observed in Figure 54. When the reactive losses was increased above the rated capacity of the converter, the system became unstable. This seemed to be the limiting factor when the line resistance was increased as well, The increased active power losses was covered by the grid, as seen in Figure 55, however the increased reactive power loss was covered by the converter. An interesting observation is that the converter was able to inject more reactive power in this scenario, which is likely due to less reactive losses.
For the grid-following converter the limitations was not on the power capability, rather on the power quality. Increasing the line reactance above 5.6 pu resulted in a distorted voltage and insufficient power quality, as seen in 58a. The oscillations in the signal is high-frequency which might be because of the PLL not being able to synchronize again without the signal containing a large amount of noise caused by the increasing line reactance, shown in 58b. When the line resistance was increased it caused the voltage to drop because of the increased reactive power losses. Furthermore low-frequency frequency oscillations occurred when the resistance was increased above $600\Omega = 13.7$ pu. This is a point of weakness of the

grid-following converter, according to [37]. A physical explanation is presented in [38] which suggest that it happens because the phase angle of the converter output voltage becomes very sensitive when the line impedance is increased. This is then more disturbed by I_d and I_q current injections, which in turn is calculated based on the PLL reference angle, which in turn tries to lock onto the phase angle of the converter voltage. This feedback loop can fall out of stability if the phase angle of the voltage changes to quickly, as it does when subject to a symmetrical fault, because the PLL is not able to keep up. This correlates well with 60a and is reasonable to suspect is the explanation of the results. A possible solution would be to reduce the PLL gains, to slow it down, allowing it to follow the phase angle better. Similar to the effect seen in the grid-forming converter when removing the feed-forward term.

Generally there are both advantages and disadvantages of both the grid-forming converter and grid-following converter. In this simulation study the performance of the grid-following converter has been superior to the grid-forming with regards to stability and power quality. However it might have been in a slightly unfair result. As the grid is modelled as a stiff voltage source, this is highly in favour of the grid-following converter. Often grid-forming converters are modelled with synthetic inertia, which has a stabilising effect on the performance. This was not done in this simulation study. Furthermore the fault current limitations are very simple, and came at large cost of performance for the grid-forming converter. A better fault current limitation scheme, with less cost of performance would also push the grid-forming converter closer to the grid-following converter. A proposed method in [11] based on adding the V_q component in the droop equation as a non-linear component, could yield better performance. Other methods include adding extra virtual impedance whenever the current surpasses a pre-defined threshold [25], or switching the control method to grid-following control when the fault occurs [24] which could be a relevant for further work with this model. In addition it might be that a better performance could be achieved with other saturation limits, however according to [37] reducing the saturation limits on the current regulators will increase the risk of not synchronizing.
The effect of limiting the feed-forward term in the voltage controller compared to removing it is that the response is faster, but more dramatic generally. It also seems to have a smaller range of operation, as it becomes unstable earlier. If there was another way of improving the response time of the grid-forming converter without feed-forward in the voltage loop, it would probably be a more robust solution, compared to reducing the limitations on the feed-forward term. The grid-following converters point of weakness was exposed when the grid connection became increasingly weaker, hence it is a cross-over point in high-impedance grid where the grid-forming converter performs better, even with simple current limitations presented here.
In addition for the virtual frequency in the converter, it is clear that the grid-forming converter performs better. However it is important to consider the point of view of the grid. As the grid-forming converter allows the voltage to drop further it might be seen as a equally large disturbance, causing the grid frequency to change as much as it would have for a grid-following converter. Furthermore, initial fault conditions might have been in favour of one of the control system, but the important aspect is the relative performance between

them.
Another major drawback of the grid-forming converter illustrated in this thesis was the loss of synchronisation because the d-axis voltage regulator lost contact with its reference. This could likely have been improved by reducing the regulator gains enabling a slower response of the regulator. As the tuning values calculated by the tuning principles presented in the tuning chapter caused an insufficient performance, the tuning was done manually which might have resulted in over-tuning the regulators. The calculated tuning values are are highly dependent on the parameters of the LCL filter, and it might be that the presence of resistance and inductance elsewhere in the model causes the tuning parameters to not work. Furthermore, there are other forms of control schemes for the grid-forming converter that could have improved the performance. Some of these are *Synchronous Power Controller* (SPC), *Virtual Synchronous Machine* (VSM), *Synchroverter* and *Power Synchronization Control* [37]. However droop control was utilized in this study as it was the most relevant for the case presented by Siemens Energy.

9. Conclusion

It is important to remember that even though this is an fairly detailed modelled, it is still an aggregated model which should be used to observe tendency rather than specific details. Looking at the larger picture some trends are clear throughout the simulation study of the control systems.
Two different control methods of the voltage source converter, PLL-based grid-following control and droop-based grid-forming control, have been studied under varying three-phase fault conditions. Because of the nature of grid-forming control, it is a difficult and complex task to limit over-currents during and when clearing the fault, as well as maintaining synchronization and sufficient power quality afterwards compared to the PLL-based grid-following control system.
Two simple methods for limiting the fault current in the grid-forming control system was tested, and it was discovered that removing the feed-forward term in the voltage control loop was the better option. However both of these resulted in a large loss of performance, and loss of the sought-after abilities that define a grid-forming converter. The PLL-based grid-following control is a highly reliable and well-performing control system. However, if exposed to a high impedance grid the grid-forming converter performs better, even with simple over-current limitation methods.
It can therefore be concluded that without proper fault current limitations techniques in the droop-based grid-forming converter, the PLL-based grid-following converter performs better whenever not exposed to a high impedance grid. Lastly, the work to establish fault current limitation methods for the grid-forming converter will be crucial moving forward in order ensure a safe, reliable and flexible power system in the future.

9.1. Further work

The field of study in this thesis has lots of undiscovered potential, and interesting topics to further look into. The simulink model, as well as the Matlab-code is attached in order to facilitate further work on this model. Some suggestions for further work are presented below.

- Expanding the droop-based grid-forming converter model with some of the suggested fault current limitation techniques.
- Modelling and testing other synchronization methods than droop control for the grid-forming converter.
- Expanding the model with to include Pulse-Width-Modulation based VSC, introducing switching harmonics to further understand the power quality issues related with this issue.
- Making a linearized model of the simulink model. Expanding the one created in the project thesis in order to better the comparison between theory and practise.
- Expanding the model handle different types of fault scenarios. Testing for unsymmetrical fault showed that the grid-following control was able to handle it, but the grid-forming control, with its simple current limitations was not able to stabilize.

Bibliography

[1] Aabakken, C., Aker Nordeng, R., Eggum, E., Hansen, H., and Tjersland, J. (2018). Veileder til leveringskvalitetsforskriften. Technical report, Norges vassdrags- og energidirektorat, Middelthunsgate 29, Oslo.

[2] Balchen, J. G. (2016). Reguleringsteknikk. Edition: 6. utg. ISBN: 978-82-7842-202-1 Place: Trondheim.

[3] CENELEC (2005). EN 50160. Technical report, CENELEC, Brussels, Belgium.

[4] Ding, H., Wang, Z., Fan, L., and Miao, Z. (2021). Modeling and Control of Grid-following Single-Phase Voltage-Sourced Converter. pages 1–6.

[5] ENTSO-E (2018). ENTSO-E Future System Inertia 2. Technical report, ENTSO-E, Avenue Cortenbergh 100, 1000 Brussels, Belgium.

[6] Fang, J., Li, X., and Tang, Y. (2016). A review of passive power filters for voltage-source converters. pages 1–6.

[7] GL, D. (2019). Barometer for grønn omstilling av skipsfarten. Tech, DNV GL, Fornebu, Oslo.

[8] Glover, J. D. (2017). Power system analysis & design. Edition: Sixth edition. ISBN: 9781305636187 Place: Boston, Mass.

[9] Guerrero, J., de Vicuna, L., Matas, J., Castilla, M., and Miret, J. (2004). A wireless controller to enhance dynamic performance of parallel inverters in distributed generation systems. *IEEE Transactions on Power Electronics*, 19(5):1205–1213.

[10] Hordnes, E. (2019). RACE TO ELECTRIFICATION – NORWAY IN A POLE POSITION. Technical report, Sweco.

[11] Huang, L., Xin, H., Wang, Z., Zhang, L., Wu, K., and Hu, J. (2019). Transient Stability Analysis and Control Design of Droop-Controlled Voltage Source Converters Considering Current Limitation. *IEEE Transactions on Smart Grid*, 10(1):578–591.

[12] Janssen, A., Zhuang, Q., McGuinness, S., Poggi, G., Kubis, A., Palazzo, M., Aprosin, K., and Willième, J.-M. (2017). Operating experience with and future challenges for coordinating power plant and power system protection. *Cigre Science & Engineering*, 7:63.

[13] Kahlane, A. E. W. H., Hassaine, L., and Kherchi, M. (2015). LCL filter design for photovoltaic grid connected systems.

[14] Karimi, S., Zadeh, M., and Suul, J. A. W. (2020a). Evaluation of Energy Transfer Efficiency for Shore-to-Ship Fast Charging Systems. Publisher: Institute of Electrical and Electronics Engineers (IEEE).

[15] Karimi, S., Zadeh, M., and Suul, J. A. W. (2020b). Shore Charging for Plug-In Battery-Powered Ships: Power System Architecture, infrastructure, and Control. Publisher: Institute of Electrical and Electronics Engineers (IEEE).

[16] Li, F., Li, R., and Zhou, F. (2015). *Microgrid Technology and Engineering Application*. Elsevier Science & Technology, San Diego.

[17] Lin, C.-H. and Wu, Y.-K. (2021). Overview of Frequency-Control Technologies for a VSC-HVDC-Integrated Wind Farm. *IEEE Access*, 9:112893–112921.

[18] Liu, J., Miura, Y., and Ise, T. (2014). Dynamic characteristics and stability comparisons between virtual synchronous generator and droop control in inverter-based distributed generators. In *2014 International Power Electronics Conference (IPEC-Hiroshima 2014 - ECCE ASIA)*, pages 1536–1543.

[19] Machowski, J. (2002). Power system dynamics : stability and control. Edition: Third ed. ISBN: 9781119526346 Place: Chichester.

[20] Mahmoud, M. S. (2016). *Microgrid: Advanced Control Methods and Renewable Energy System Integration*. Elsevier Science & Technology, Oxford. Publication Title: Microgrid.

[21] MathWorks, I. (2006). Three-Phase Fault.

[22] Melby, M. (2019). Comparison of virtual oscillator control and droop control in an inverter-based stand-alone microgrid.

[23] NVE (2004). Forskrift om leveringskvalitet i kraftsystemet.

[24] Oureilidis, K. O. and Demoulias, C. S. (2016). A Fault Clearing Method in Converter-Dominated

Microgrids With Conventional Protection Means. *IEEE Transactions on Power Electronics*, 31(6):4628–4640.

[25] Paquette, A. D. and Divan, D. M. (2015). Virtual Impedance Current Limiting for Inverters in Microgrids With Synchronous Generators. *IEEE Transactions on Industry Applications*, 51(2):1630–1638.

[26] Patel, V. and Jamnani, J. (2015). Techniques to increase Surge Impedance Loading level of EHV AC transmission lines for improving power transfer capability. In *2015 International Conference on Computation of Power, Energy, Information and Communication (ICCPEIC)*, pages 0518–0523.

[27] Qoria, T., Rokrok, E., Bruyere, A., François, B., and Guillaud, X. (2020). A PLL-Free Grid-Forming Control With Decoupled Functionalities for High-Power Transmission System Applications. *IEEE Access*, 8:197363–197378.

[28] Rokrok, E., Qoria, T., Bruyere, A., Francois, B., and Guillaud, X. (2020). Classification and dynamic assessment of droop-based grid-forming control schemes: Application in HVDC systems. *Electric Power Systems Research*, 189:106765.

[29] Rygg, A. (2022). marine power system design.

[30] Sanchez, S., Bergna, G., and Tedeschi, E. (2017). Tuning of control loops for grid-connected Modular Multilevel Converters under a simplified port representation for large system studies. In *2017 Twelfth International Conference on Ecological Vehicles and Renewable Energies (EVER)*, pages 1–8.

[31] Skjong, E., Rodskar, E., Molinas, M., Johansen, T. A., and Cunningham, J. (2015). The Marine Vessel's Electrical Power System: From its Birth to Present Day. *Proceedings of the IEEE*, 103(12):2410–2424. Place: New York Publisher: IEEE.

[32] Statnett (2021). Nettutviklingsplan 2021. Technical report, Statnett.

[33] Storlien, O. A. (2021). *Power Quality requirements and standards in weak grids during charging of electric vessel*. Specialization Project, Norwegian University of Science and Technology, Trondheim, Gløshaugen.

[34] Suul, J., Ljokelsoy, K., and Undeland, T. (2009). Design, tuning and testing of a flexible PLL for grid synchronization of three-phase power converters. pages 1 – 10.

[35] Suul, J. A. (2021). Phase Locked Loops for Grid Synchronization of Power Electronic Converters.

[36] Taha, W. (2016). Axes Transformation (abc-0-dq0). page 3.

[37] Taul, M. G., Wang, X., Davari, P., and Blaabjerg, F. (2020). Current Limiting Control With Enhanced Dynamics of Grid-Forming Converters During Fault Conditions. *IEEE Journal of Emerging and Selected Topics in Power Electronics*, 8(2):1062–1073.

[38] Zhou, J. Z., Ding, H., Fan, S., Zhang, Y., and Gole, A. M. (2014). Impact of Short-Circuit Ratio and Phase-Locked-Loop Parameters on the Small-Signal Behavior of a VSC-HVDC Converter. *IEEE Transactions on Power Delivery*, 29(5):2287–2296.

[39] Zuo, Y., Yuan, Z., Sossan, F., Zecchino, A., Cherkaoui, R., and Paolone, M. (2021). Performance assessment of grid-forming and grid-following converter-interfaced battery energy storage systems on frequency regulation in low-inertia power grids. *Sustainable Energy, Grids and Networks*, 27:100496.

Appendix A. Additional documents

Appendix B. Additional Theory

Appendix B.0.1. Swing Equation

The swing equation represents how a generator will respond to a disturbance. It can be expanded to represent how the power grid will respond to a disturbance by expanding it to represent a multi-machine system [19]. For the purpose of this thesis it is sufficient to use the single-machine representation. The swing equation is shown in Equation B.1. Here P_M,P_e and P_D is the mechanical power, electrical power and damping power respectively[19]. The difference between the electrical power demand and mechanical power will determine the change in speed and rotor angle. By modelling the generator with a very large inertia constant, H, the angular momentum becomes very large as seen in Equation B.2. The effect of this is that the change in speed and rotor angle of the generator will be negligible.

$$M\frac{\Delta\omega}{dt} = P_M - P_e - P_D = P_{acc} \tag{B.1a}$$

$$\frac{d\theta}{dt} = \Delta\omega \tag{B.1b}$$

$$M = \frac{2HS_N}{\omega_s} \tag{B.2}$$

Appendix C. Additional Simulation Results

Appendix C.1. Controller tuning

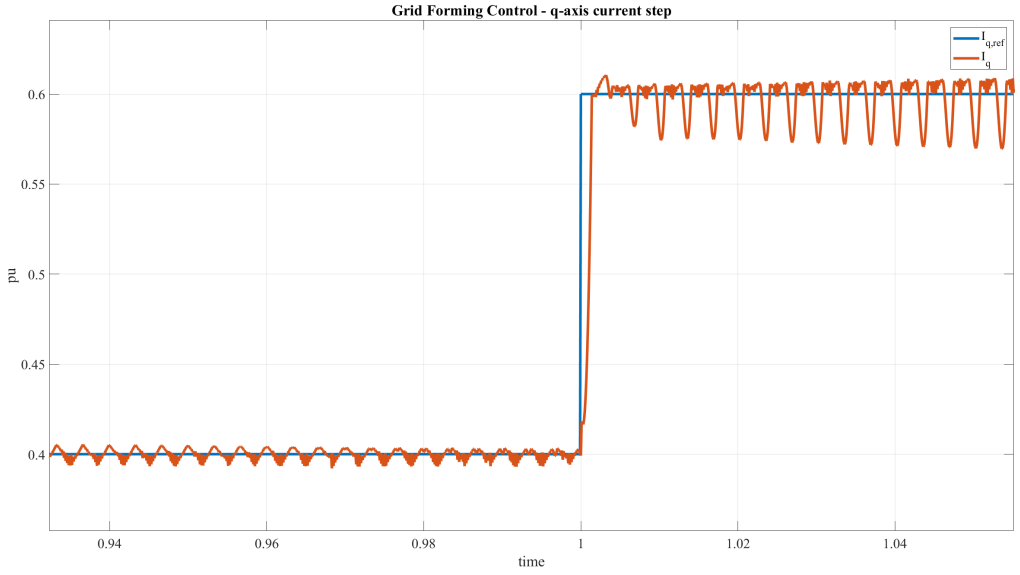

Figure C.61: Step response for I_q-regulator for GRM

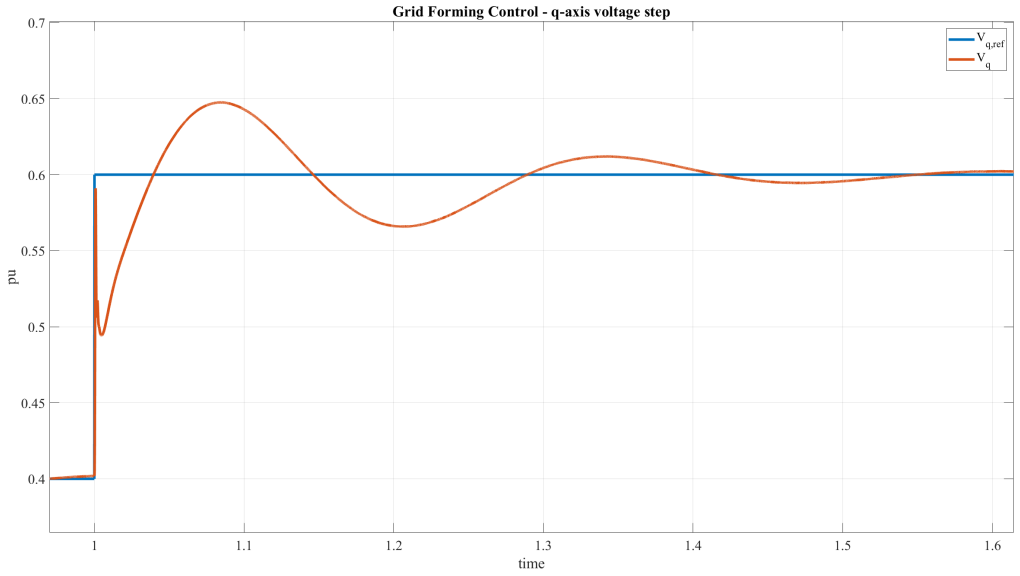

Figure C.62: Step response for V_q-regulator for GRM

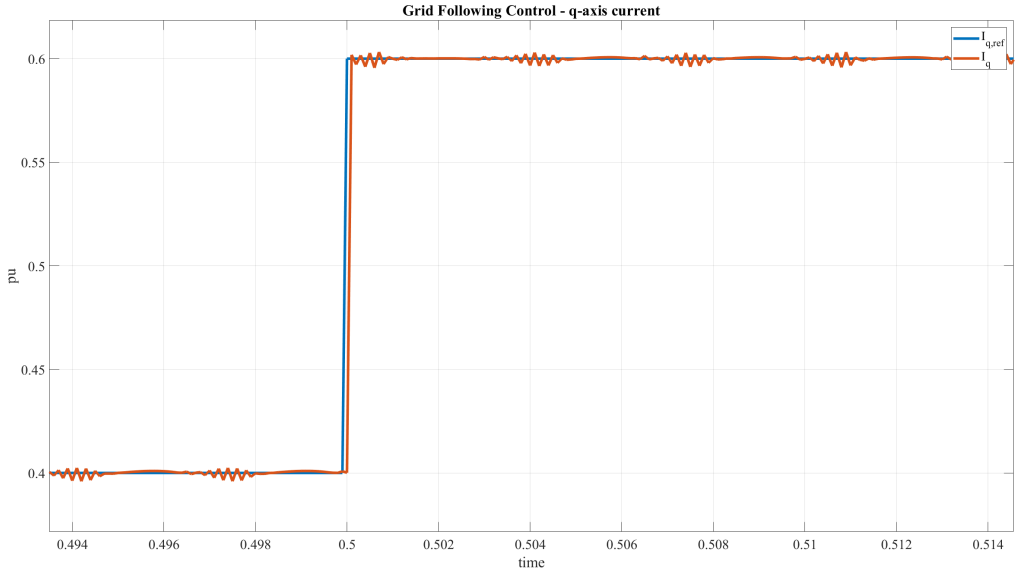

Figure C.63: Step response for I_q-regulator for GFL

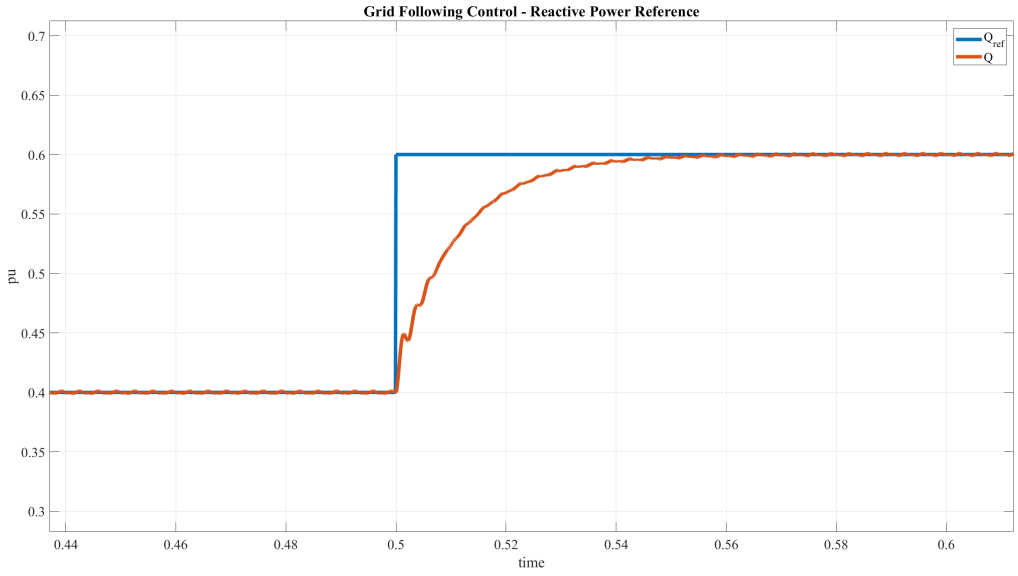

Figure C.64: Step response of reactive power control tuning

Appendix C.2. Steady state results

The voltage of the grid forming converter in $dq0$-reference frame is shown in Figure C.65. V_q is controlled to be equal to zero, indicating a working control system.

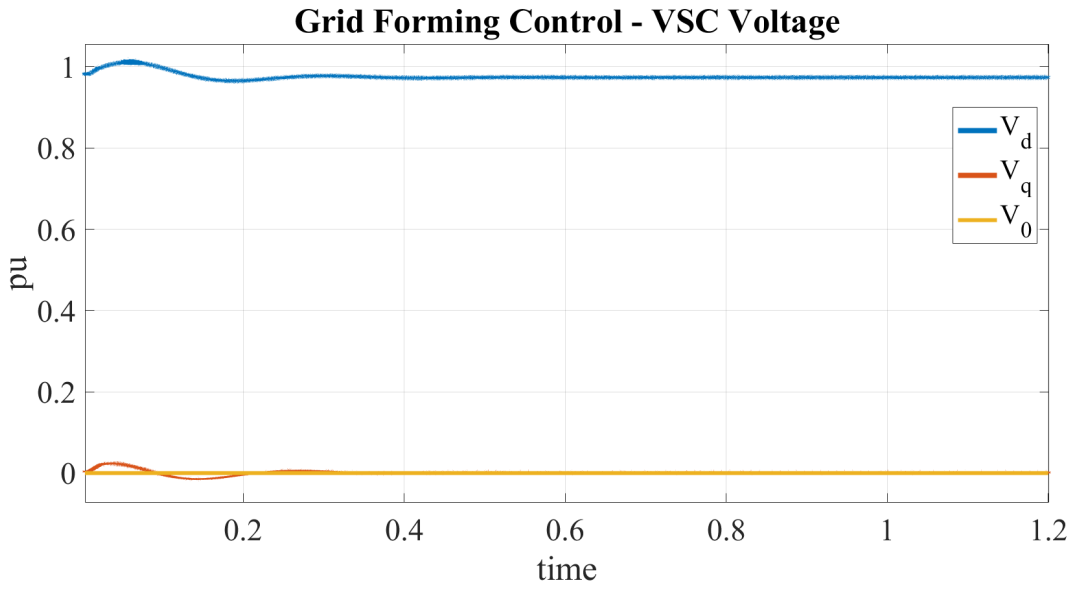

Figure C.65: d-,q-axis voltage of the steady state VSC Voltage

In Figure C.66 the frequency of the VSC voltage is shown. As can be seen the the steady state offset is negligible, and the frequency becomes 50 Hz exact.

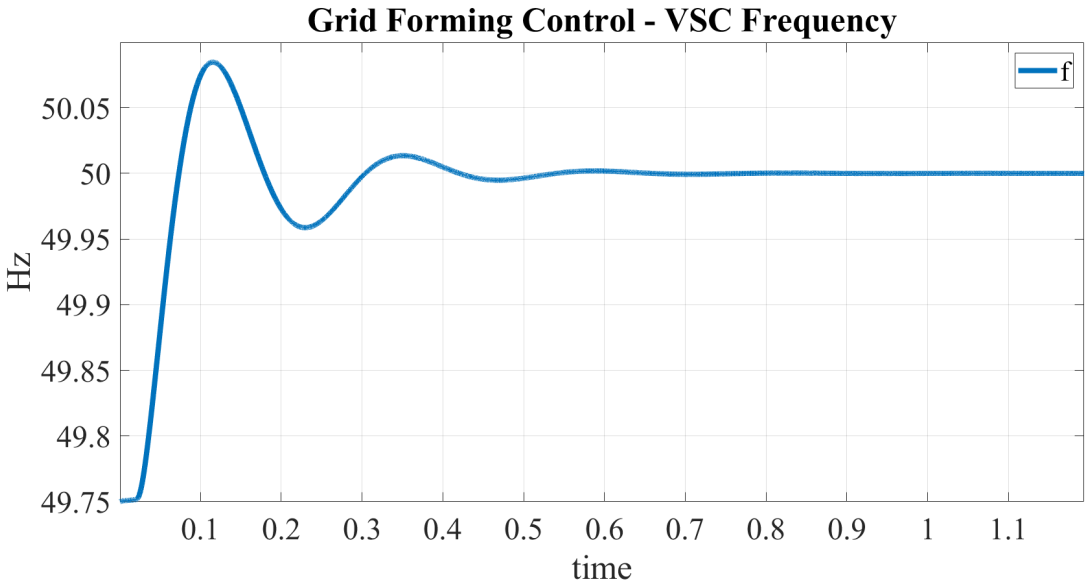

Figure C.66: VSC frequency

In Figure C.67 the active and reactive power transfer controlled by the VSC shown respectively. As can be seen the active power reaches a value of 1.5 MW, while the reactive power is approximately equal to 0.3 MVAr

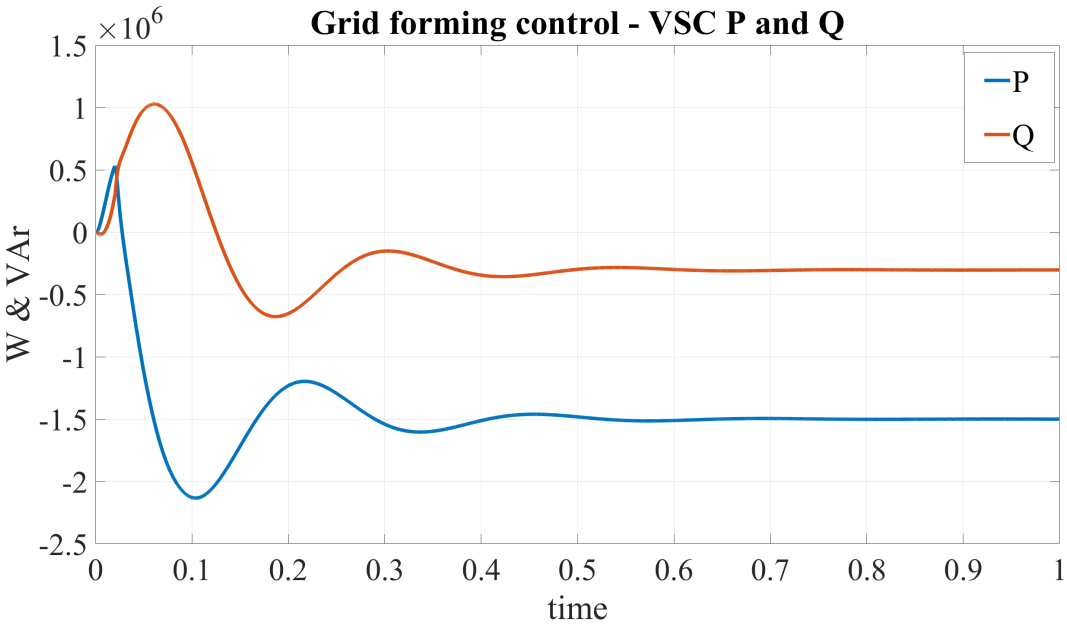

Figure C.67: Active and reactive power transferred to the on-board battery during grid forming control

In Figure C.68 the voltage is shown in the V_{dq0}-reference frame where. The V_q-component is controlled to be equal to 0 pu, while the V_d-component controls the voltage level indicating a working PLL.

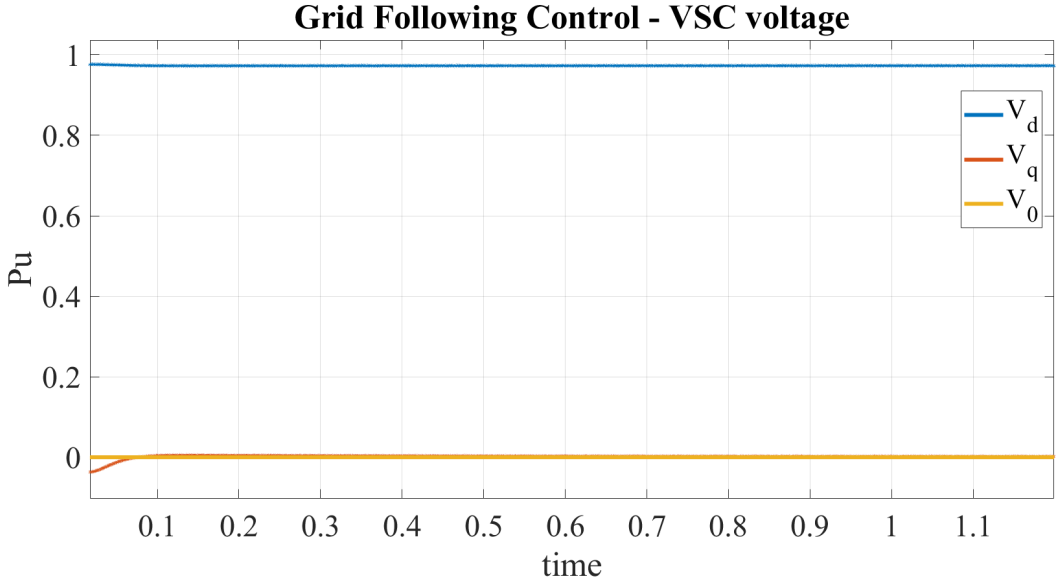

Figure C.68: d-,q-axis VSC voltage

The active and reactive power delivered to the on-board batteries is shown in Figure C.69 and Figure C.70. Both stabilize at their given set-points of 1.5 MW and 0.3 MVAr. The frequency of the voltage is shown in Figure C.71

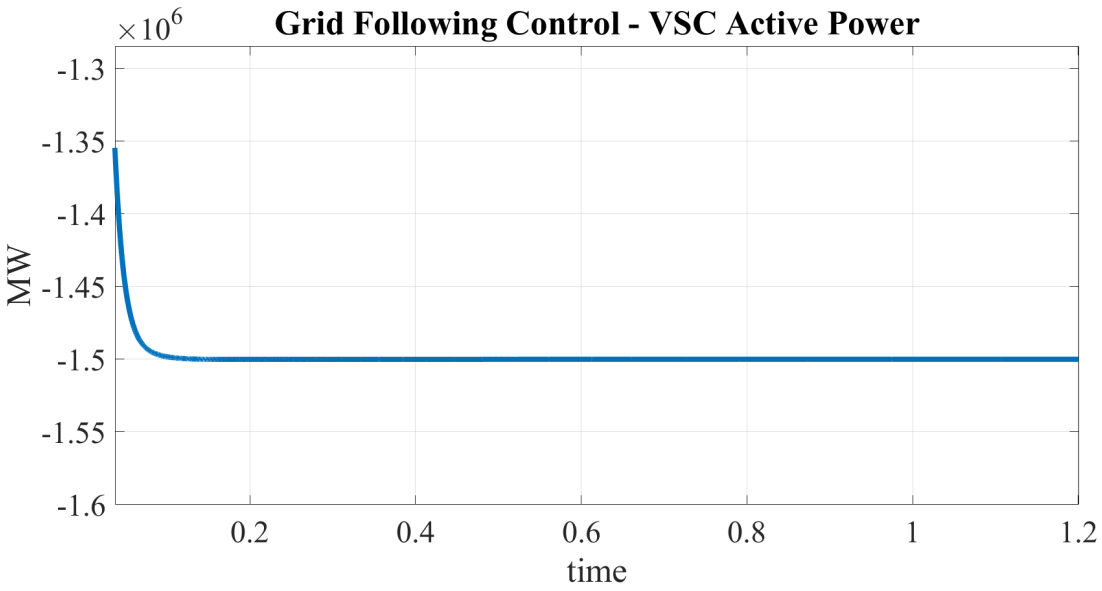

Figure C.69: Steady-state Active Power

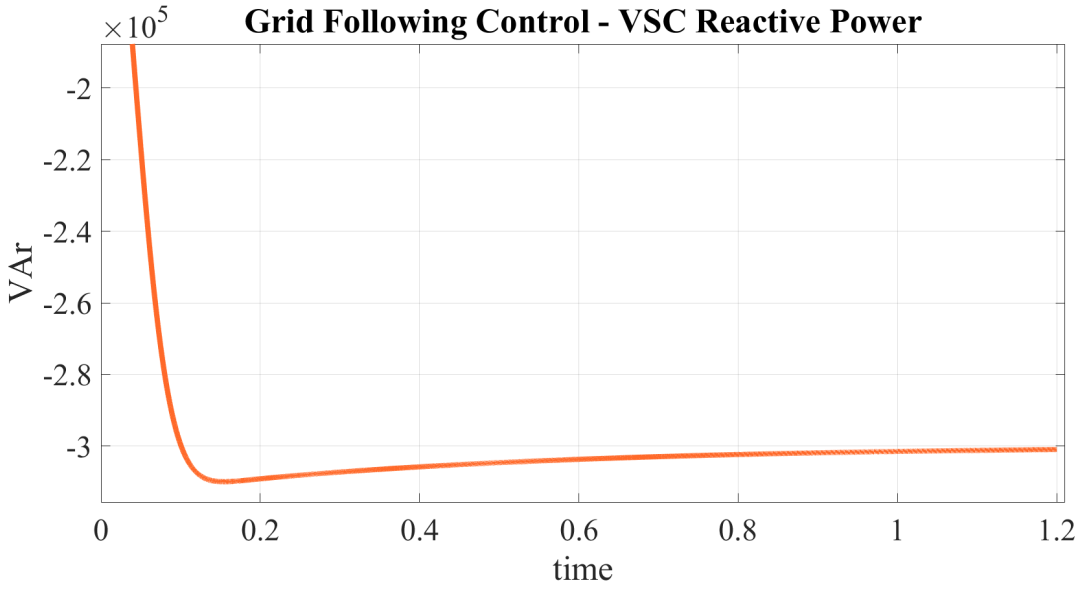

Figure C.70: Steady-state Reactive power

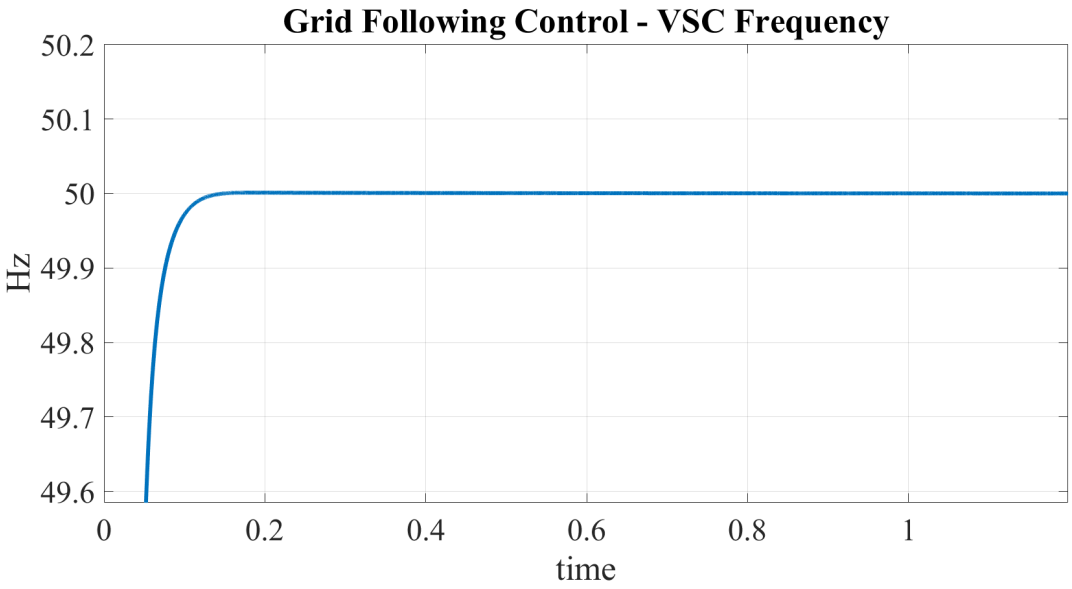

Figure C.71: Steady-state frequency

Appendix C.3. Three-phase fault

Figure C.72 shows the distorted voltage and current of the grid-following converter after the three-phase fault.

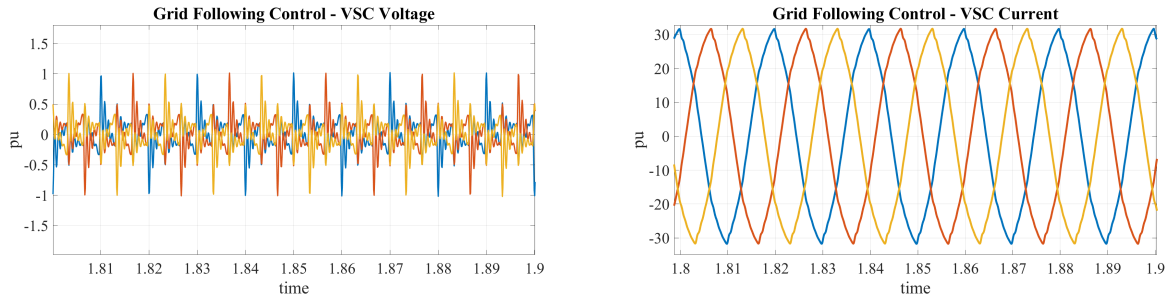

(a) Voltage **(b)** Current

Figure C.72: Grid-following converter voltage and current response after fault

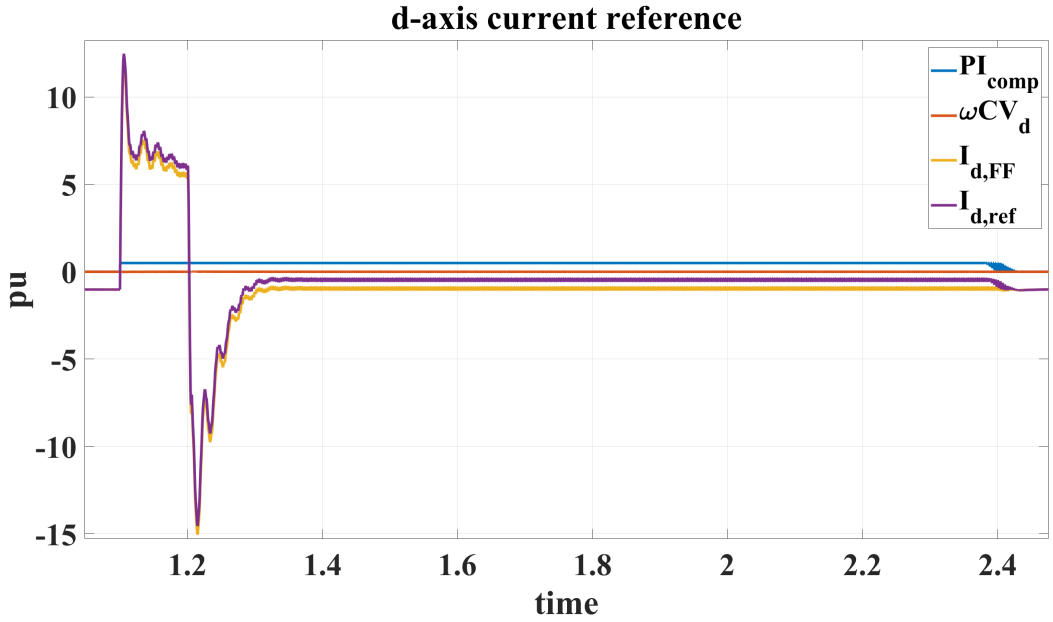

Figure C.73: d-axis current reference and its components

The active and reactive power transferred to the on-board batteries during the fault is shown in Figure C.74.

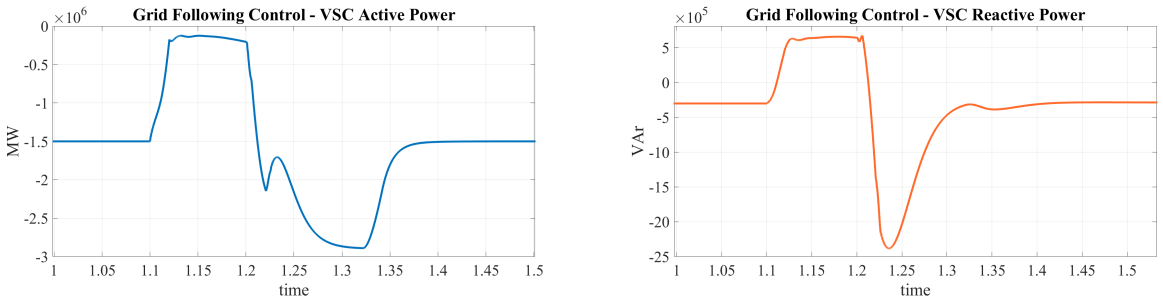

(a) Active Power **(b)** Reactive Power

Figure C.74: VSC P and Q response during and after fault with limits

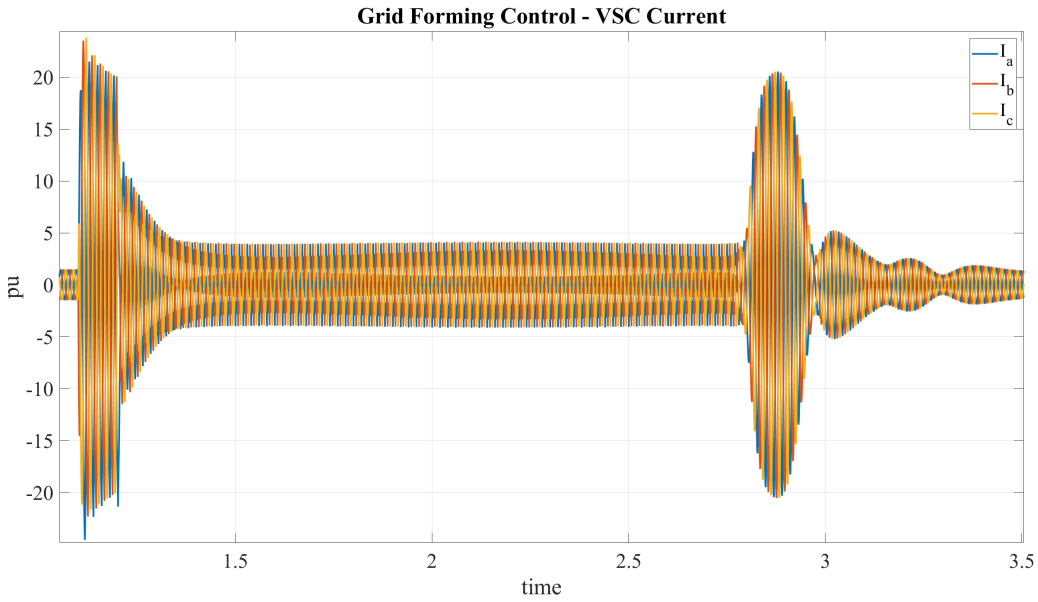

Figure C.75: VSC Current during and after three-phase fault without limitation of the regulators

The power transferred to the on-board batteries is shown in Figure C.76.

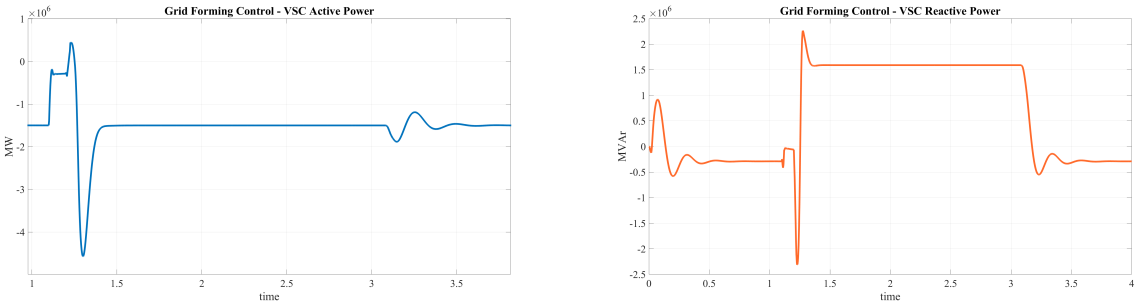

(a) Active Power **(b)** Reactive Power

Figure C.76: VSC power transferred during and after fault with limits

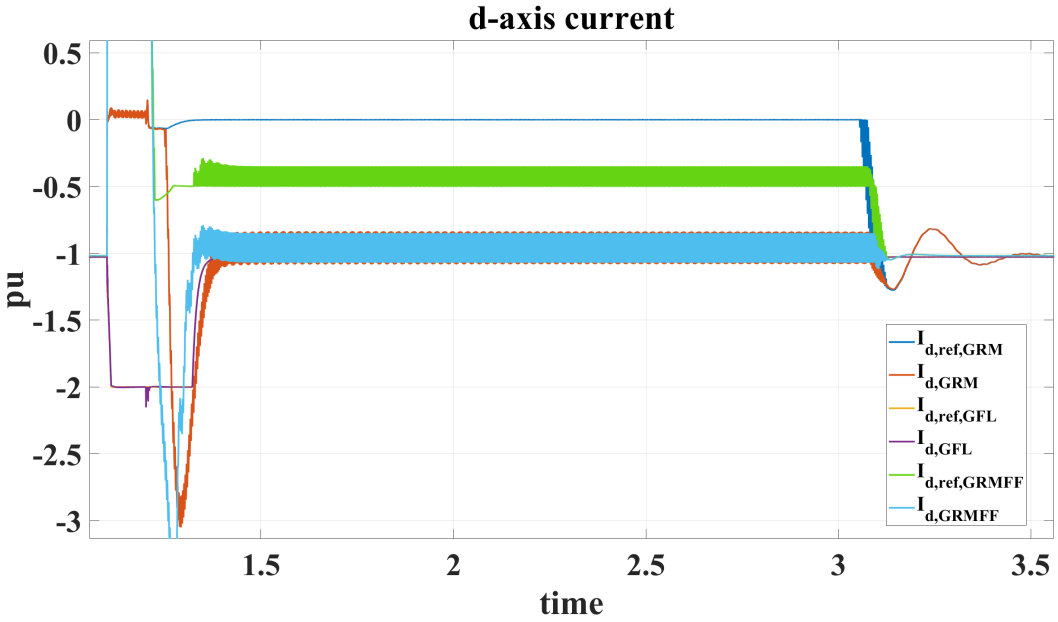

Figure C.77: Comparison of I_d response

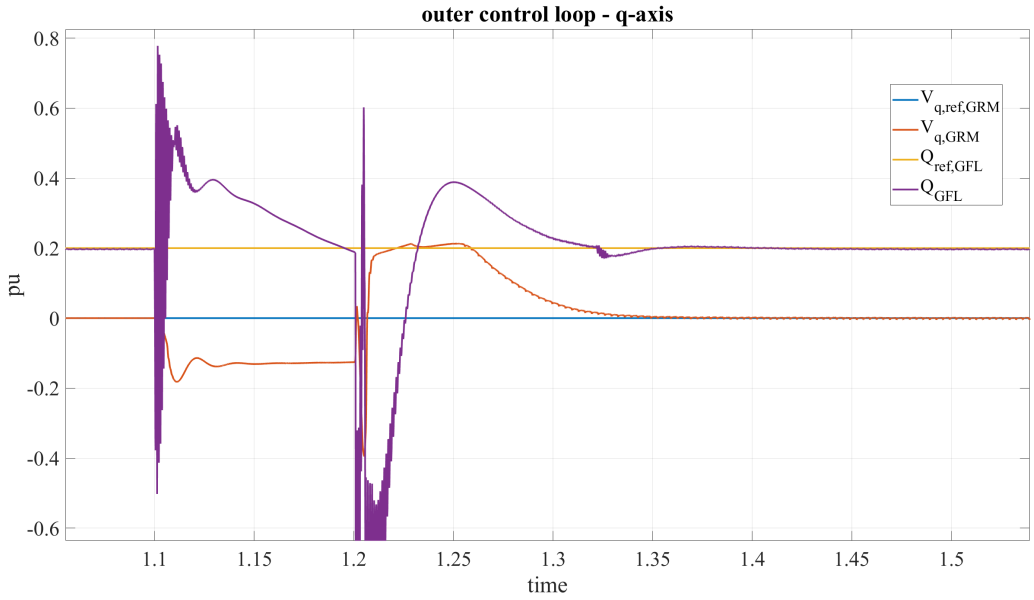

Figure C.78: Comparison of the q-axis voltage responses

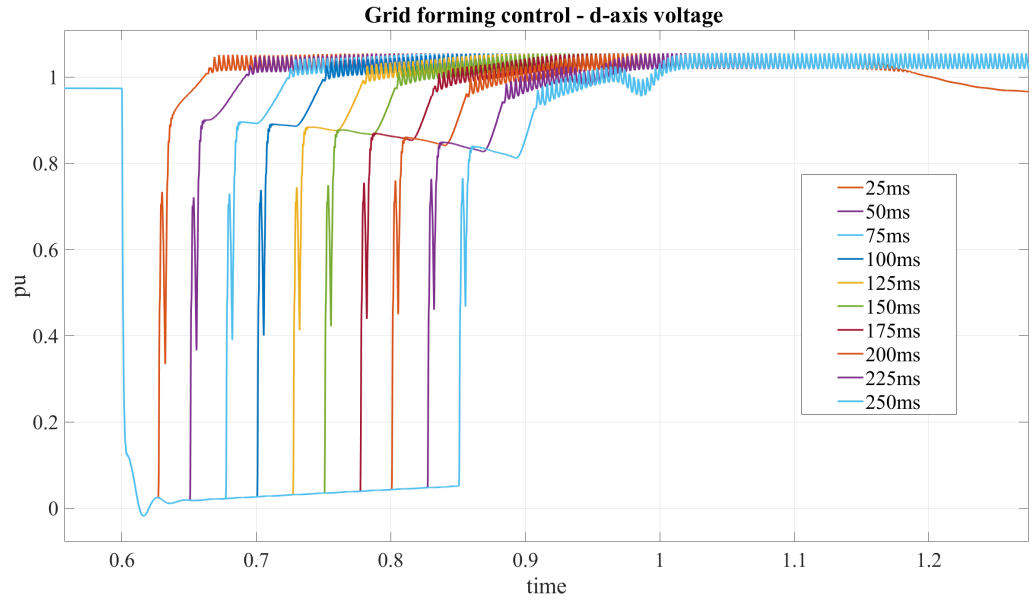

Figure C.79: Increased fault duration response

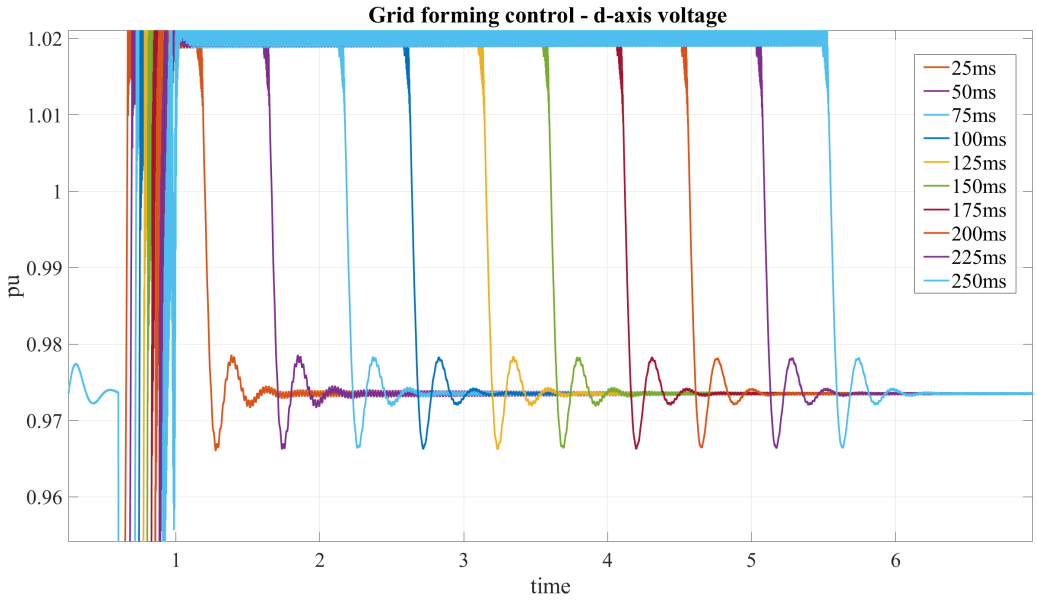

Figure C.80: Increased recovery time as a consequence of increased fault duration

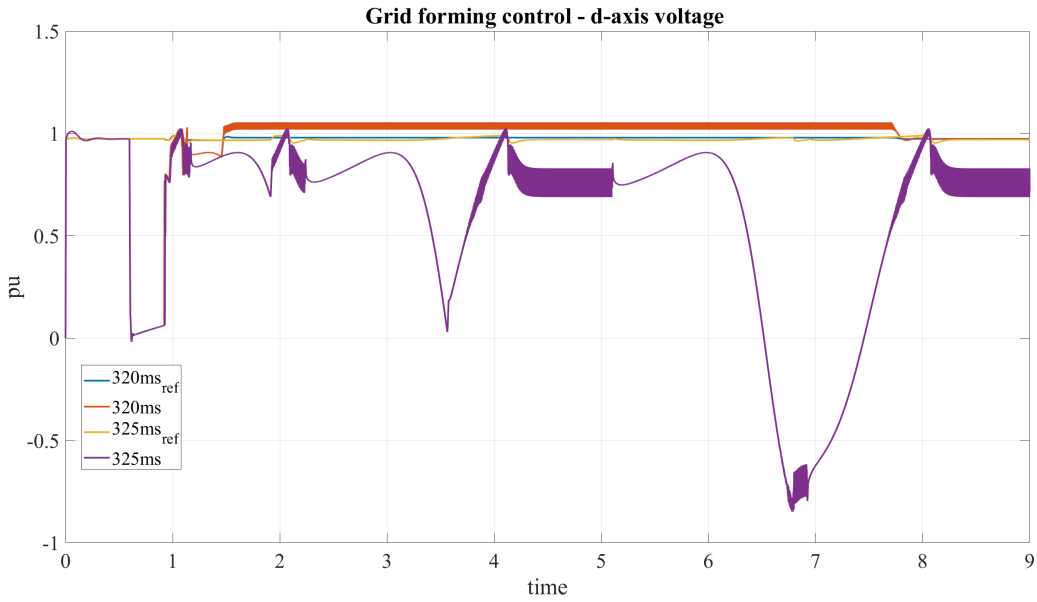

Figure C.81: The critical clearing time of the grid forming control without feed-forward

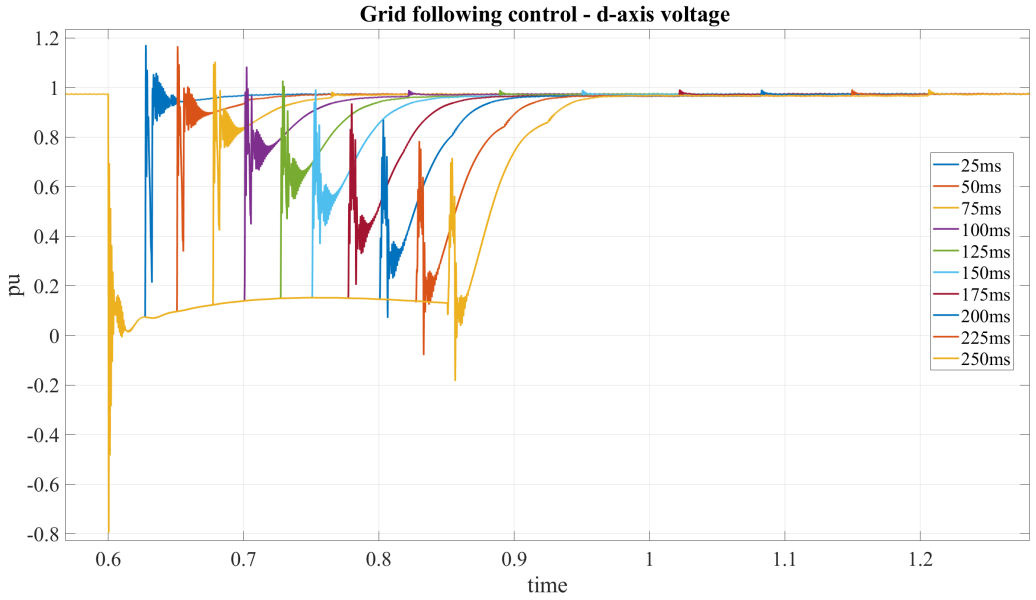

Figure C.82: Tendency of increased fault duration in the d-axis voltage

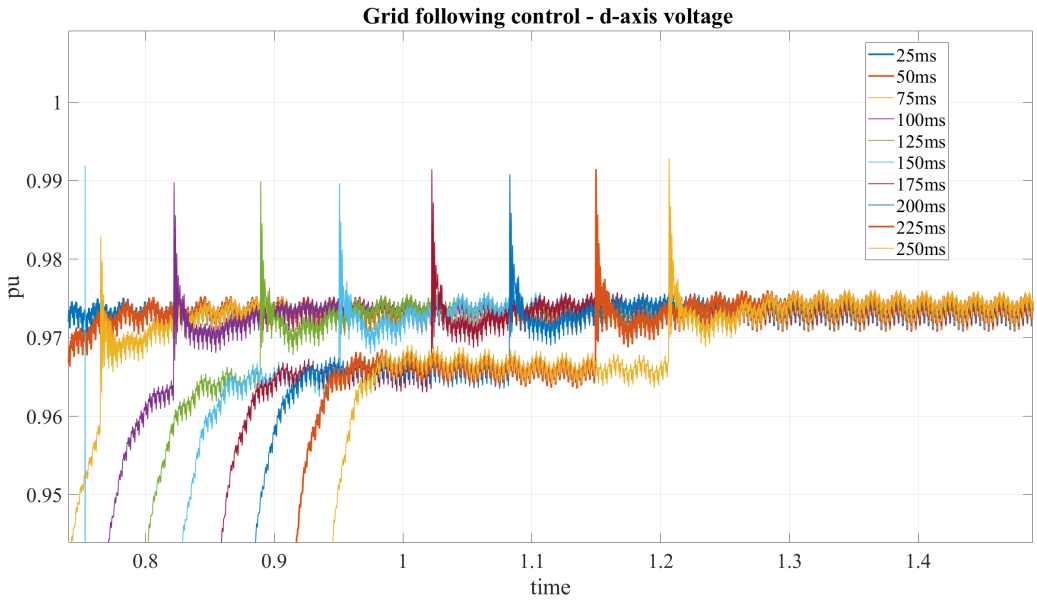

Figure C.83: Slightly increased recovery time

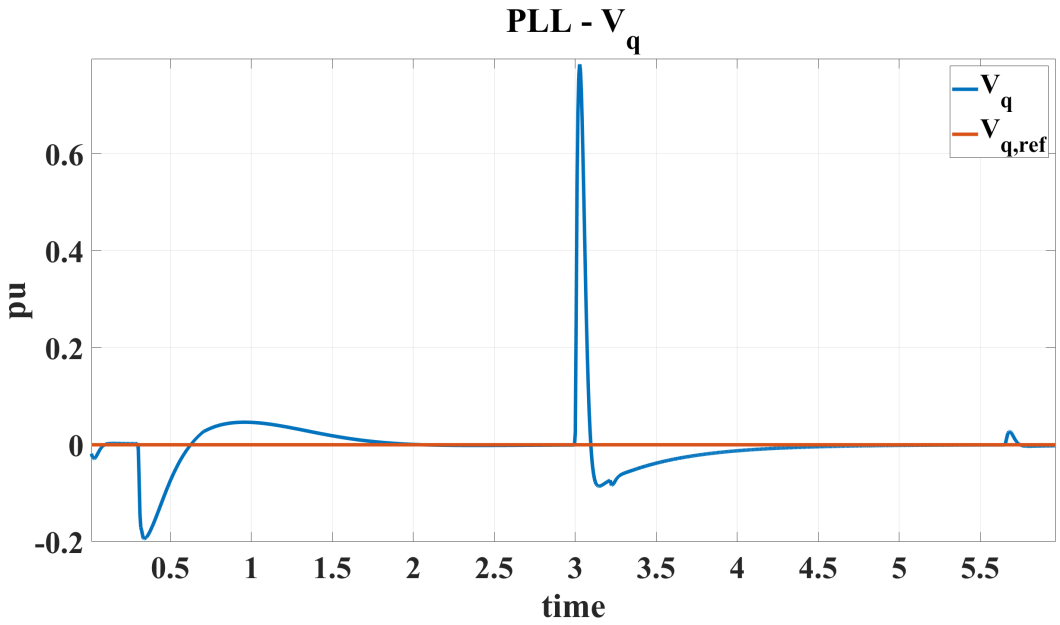

Figure C.84: PLL controlling V_q

Table C.9: Fault resistance and corresponding fault current - grid following control

Fault resistance	Fault Current rms value
$R_{on} = 1\Omega$	0.3 pu = 376.5 A
$R_{on} = 0.5\Omega$	0.59 pu = 753 A
$R_{on} = 0.1\Omega$	3.0 pu = 3765 A
$R_{on} = 0.05\Omega$	5.9 pu = 7404.5 A
$R_{on} = 0.01\Omega$	23.71 pu = 29 756 A
$R_{on} = 5m\Omega$	35.09 pu = 44 042 A
$R_{on} = 1m\Omega$	48.18 pu = 60 470 A
$R_{on} = 0.5m\Omega$	49.51 pu = 62 130 A
$R_{on} = 0.1m\Omega$	50.51 pu = 63 386 A
$R_{on} = 0.05m\Omega$	50.71 pu = 65 649 A
$R_{on} = 0.01m\Omega$	50.86 pu = 63 829.3 A

Table C.10: Fault resistance and corresponding fault current - grid forming control

Fault resistance	Fault Current rms value
$R_{on} = 1\Omega$	0.306 pu = 384 A
$R_{on} = 0.5\Omega$	0.608 pu = 763 A
$R_{on} = 0.1\Omega$	3.028 pu = 3800 A
$R_{on} = 0.05\Omega$	5.9 pu = 7404.5 A
$R_{on} = 0.01\Omega$	23.56 pu = 29 568 A
$R_{on} = 5m\Omega$	34.97 pu = 43 887 A
$R_{on} = 1m\Omega$	48.2 pu = 60 491 A
$R_{on} = 0.5m\Omega$	49.14 pu = 61 671 A
$R_{on} = 0.1m\Omega$	51.2 pu = 64 256 A
$R_{on} = 0.05m\Omega$	51.61 pu = 64 771 A
$R_{on} = 0.01m\Omega$	51.91 pu = 65 147 A

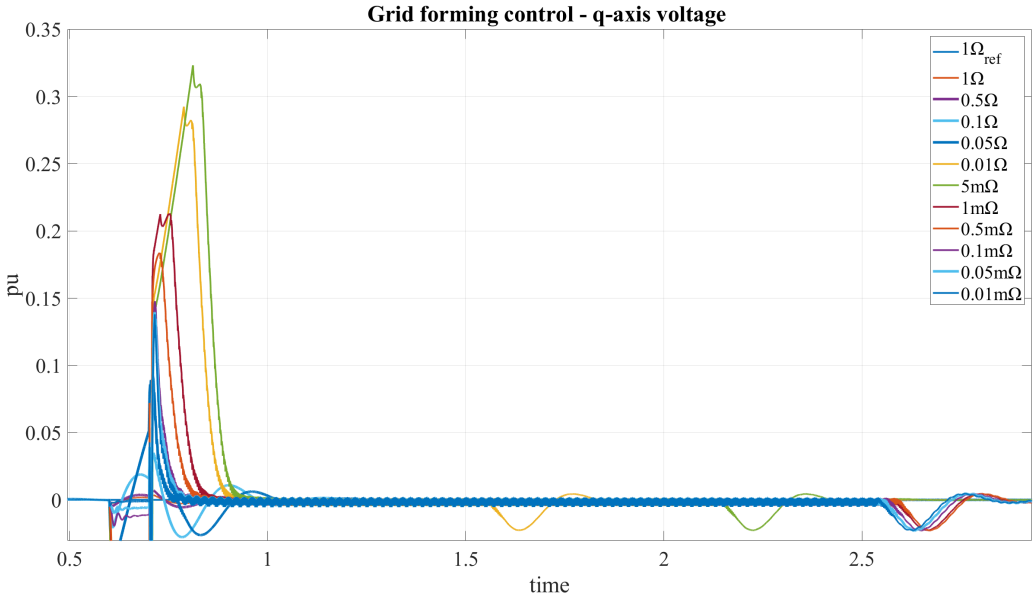

Figure C.85: V_q response to decreasing fault resistance

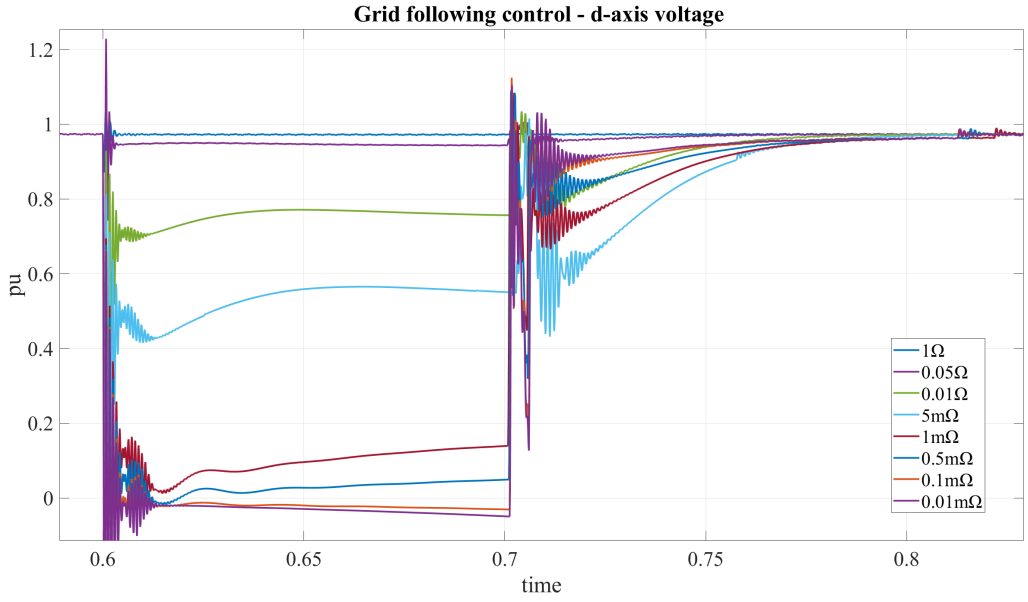

Figure C.86: The response in V_d related to variations in fault magnitude

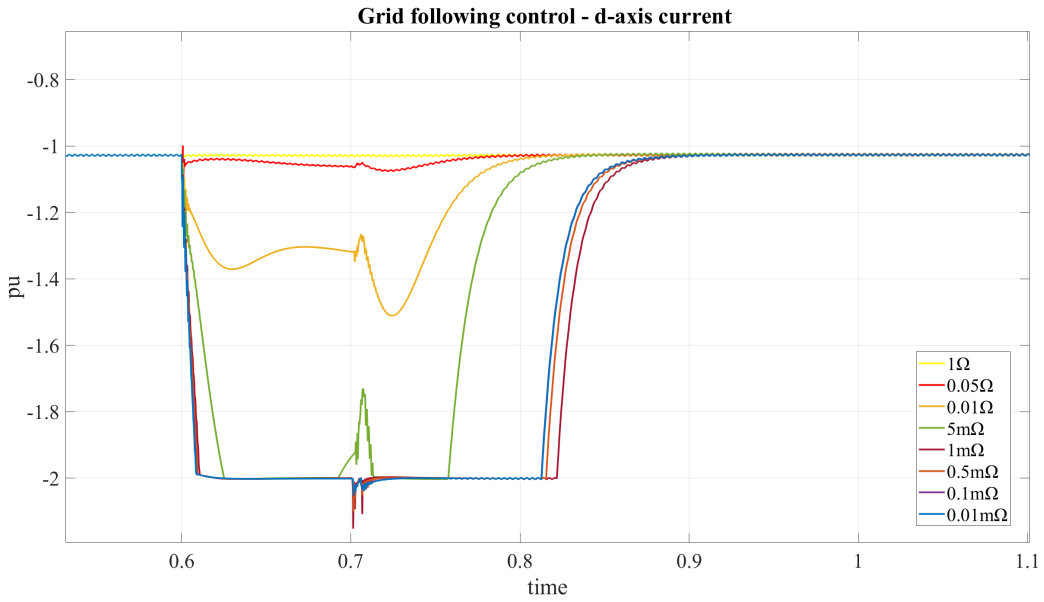

Figure C.87: The response in I_d related to variations in fault magnitude

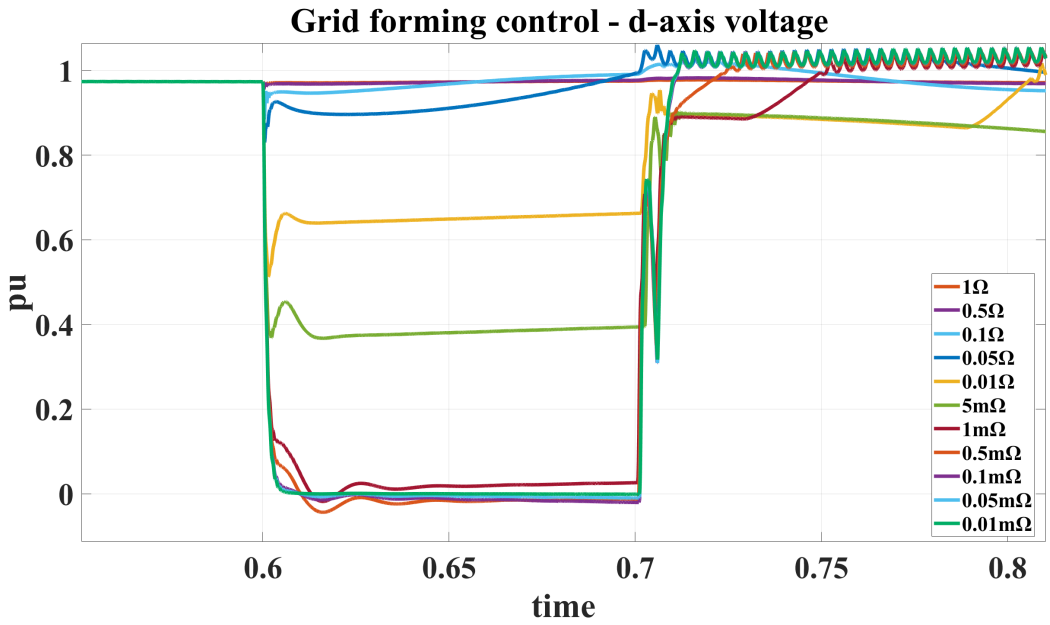

Figure C.88: V_d response of increased fault magnitude

Appendix C.6. Effect of varying the line impedance

Appendix C.7. Grid-forming control

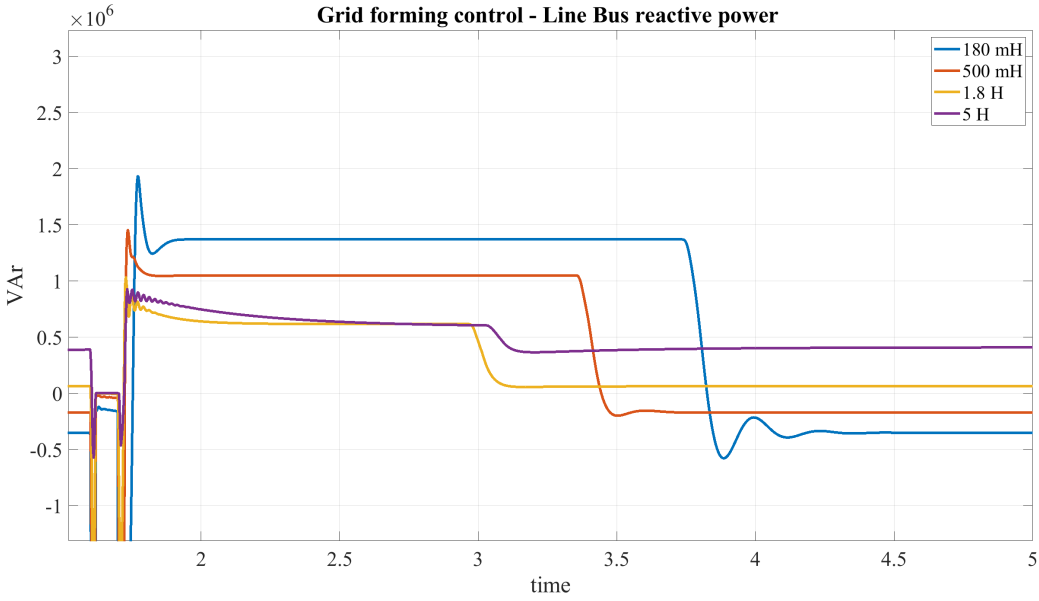

Figure C.89: Reactive power flow at the transformer-side of the transmission line

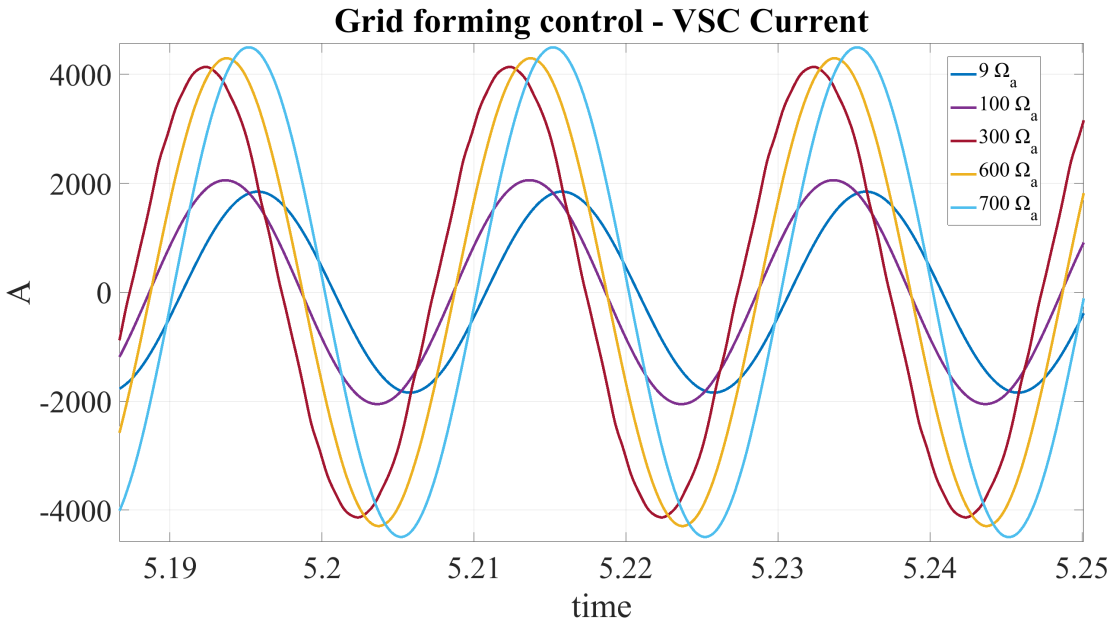

Figure C.90: Increased shift and magnitude of the VSC current

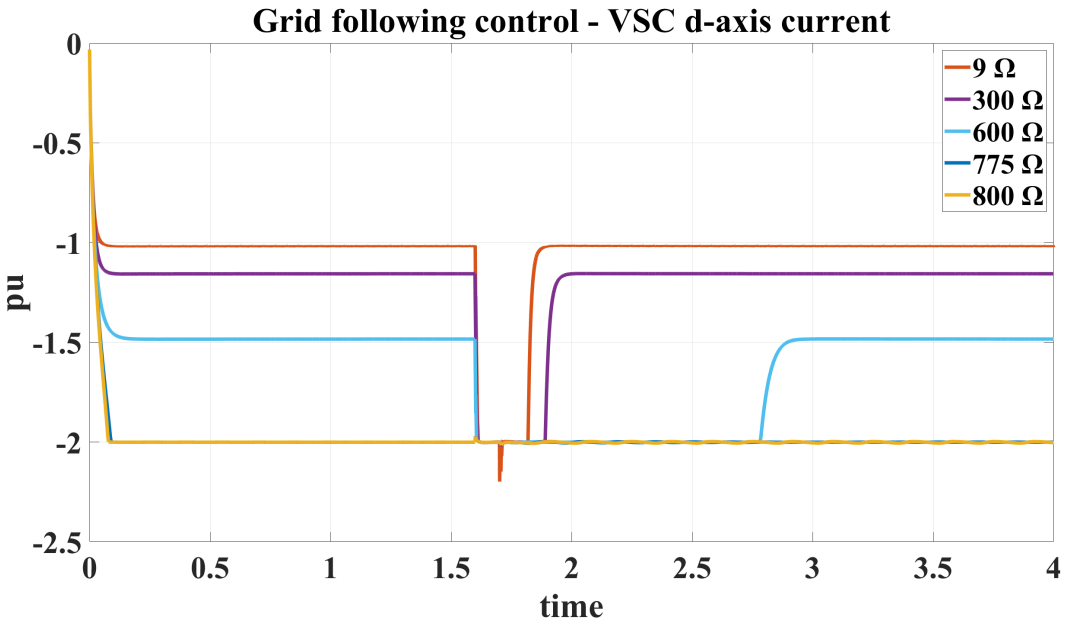

Figure C.91: Saturation limits limiting the d-axis current

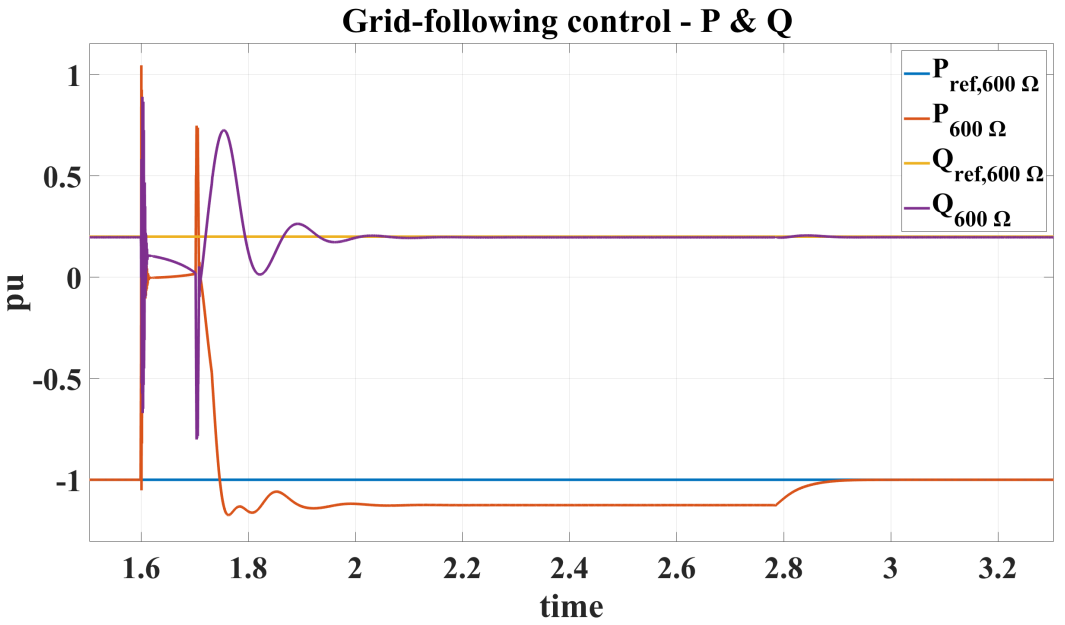

Figure C.92: P and Q control response to fault at 600Ω

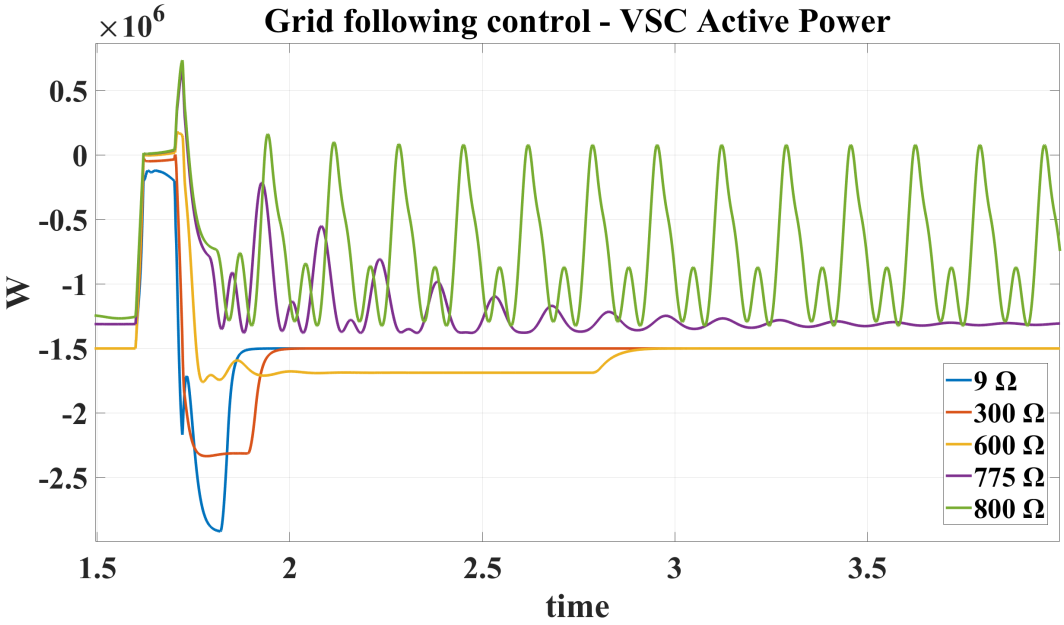

Figure C.93: The active power response to increasing line resistance

Appendix D. Simulink Models

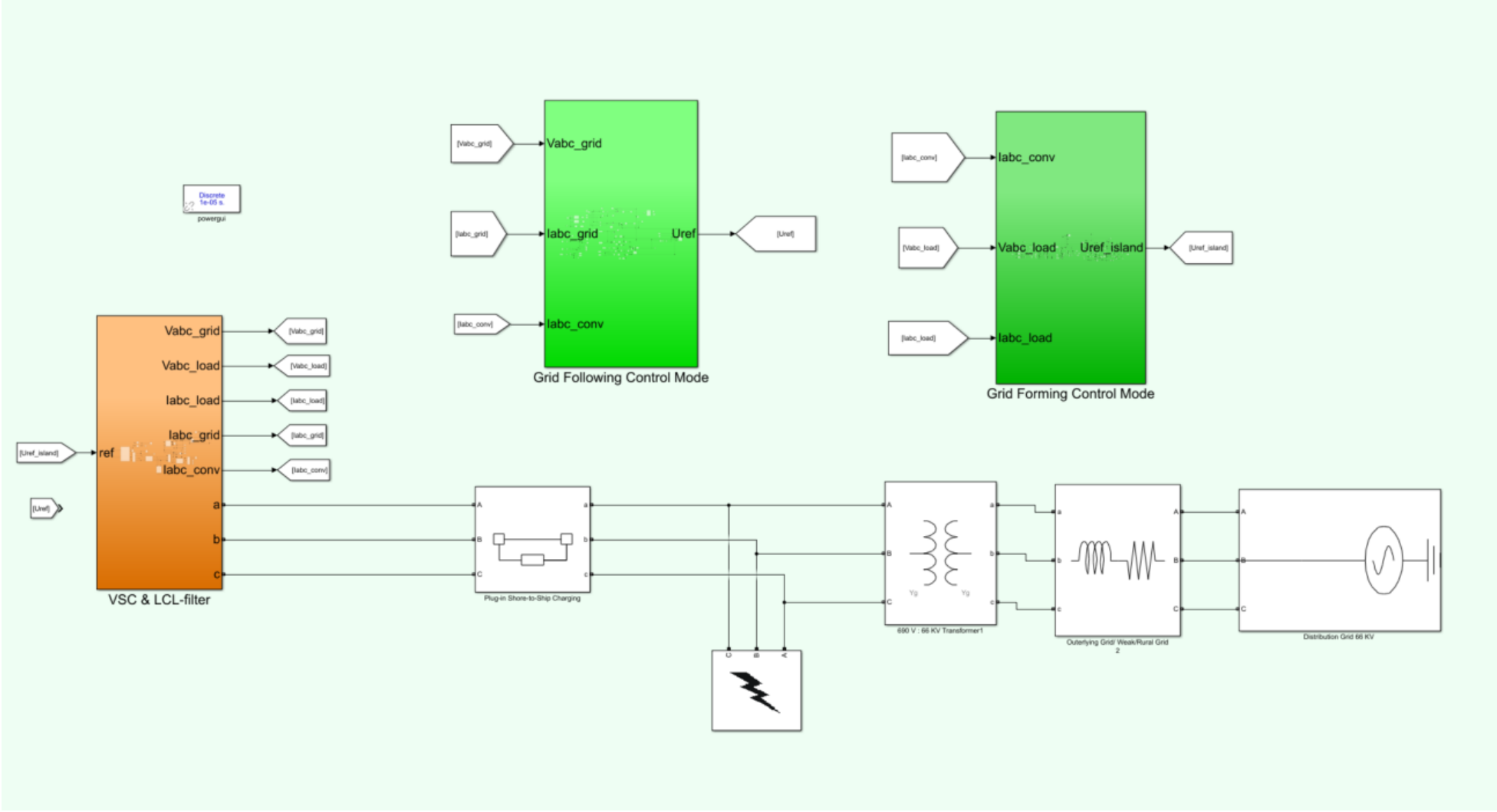

Figure D.94: The Simulink Power System Model

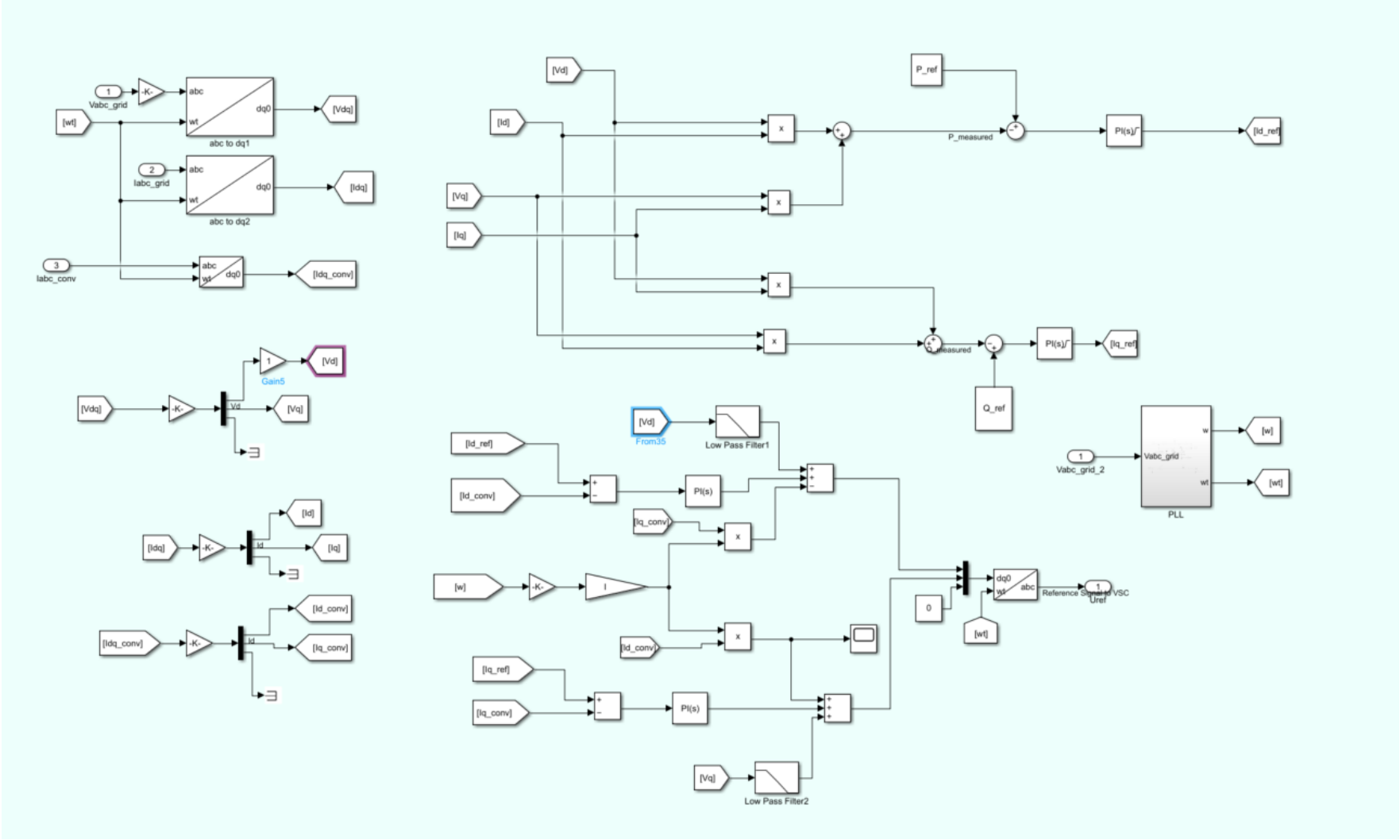

Figure D.95: The Simulink Grid-Following Model

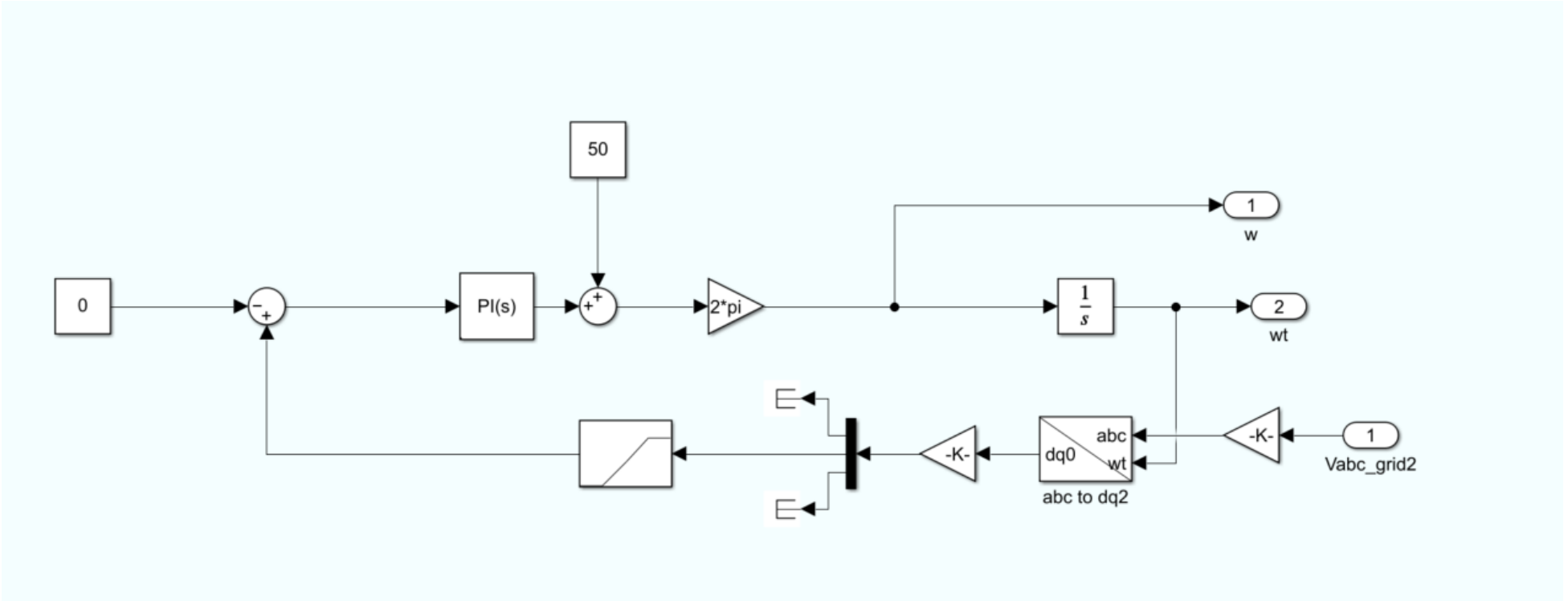

Figure D.96: The Simulink Phase Locked Loop Model

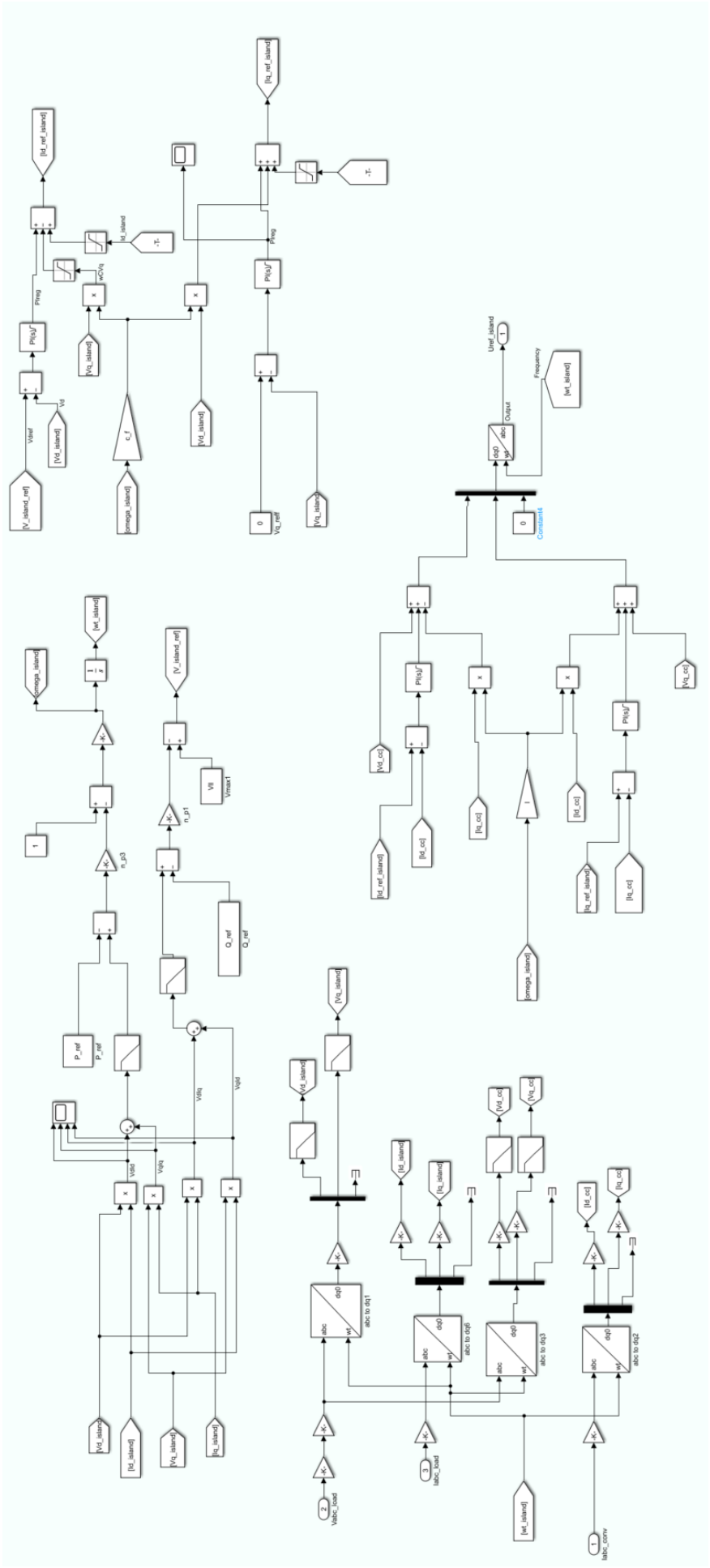

Figure D.97: The Simulink Droop-based Grid-Forming Model

```
%% System Spesifications
stepsize = 1e-5;
Vll = 690;
Vdc = 1000;
f = 50;
f_sw = 15e3;
w = 2*pi*f;
P_rated = 1.5e6;
Q_rated = 1.5e6;
V_max = 1.05*Vll;
V_min = 0.95*Vll;
w_max = 1.005*w;
w_min = 0.995*w;

%%LCL filter
R_i = 1e-3;
R_g = 1e-3;
R_d = 0.1;
L_i = 5e-5;
L_g = 3e-5;
C_f = 6e-4;

%%Base Values
Vbase = Vll;
Vbasedq = Vbase*sqrt(2);
Sbase = P_rated;
Ibase = Sbase/(Vbase*sqrt(3));
Ibasedq = Ibase*sqrt(2);
Zbase = Vbase^2/Sbase;
wbase = w;
Vdcbase = Vdc;


%%pu values
r = R_i/Zbase;
l = L_i/Zbase;
c_f = C_f/Zbase;
```

Figure E.98: Matlab Script initialising the Simulink Model

```
%%Droop coefficients
DeltaW = 0.005;
DeltaV = 0.005;
n_p = DeltaW*w/P_rated; %P-f
n_p_pu = DeltaW;
m_q = DeltaV*Vll/Q_rated; %Q-V
m_q_pu=DeltaV;


%%Power references
P_charging = -P_rated;
Q_charging = -Q_rated*0.2;
P_aux = 1e4;
Q_aux = 0.2e4;
P_ref = P_charging/Sbase;
Q_ref = Q_charging/Sbase;


%%Tuning the current controller
w_0i = 2*pi*f_sw/10; %Bandwith of the current controller
rho = 1.1; %Damping coefficient
Kp_i = 2*rho*w_0i*L_i - R_i; %Proportional gain in current controller
Ki_i = w_0i^2*L_i; %Integral gain of current controller
V_filt = 1000; %1/timeconstant for filtering the voltage at the capacitor.

%%Tuning the voltage controller
w_0v = w_0i/10; %Bandwidth of the voltage controller
Kp_v = 2*rho*w_0v*C_d; %Proportional gain in voltage controller
Ki_v = w_0v^2*C_d; %Integral gain in voltage controller

%%PLL
T_filter_PLL = 1e-2;
a_PLL = 3;

Ti_PLL = a_PLL^2*T_filter_PLL;
Kp_PLL = 1/(a_PLL*2*pi*T_filter_PLL);
```

Figure E.99: Matlab Script initialising the Simulink Model

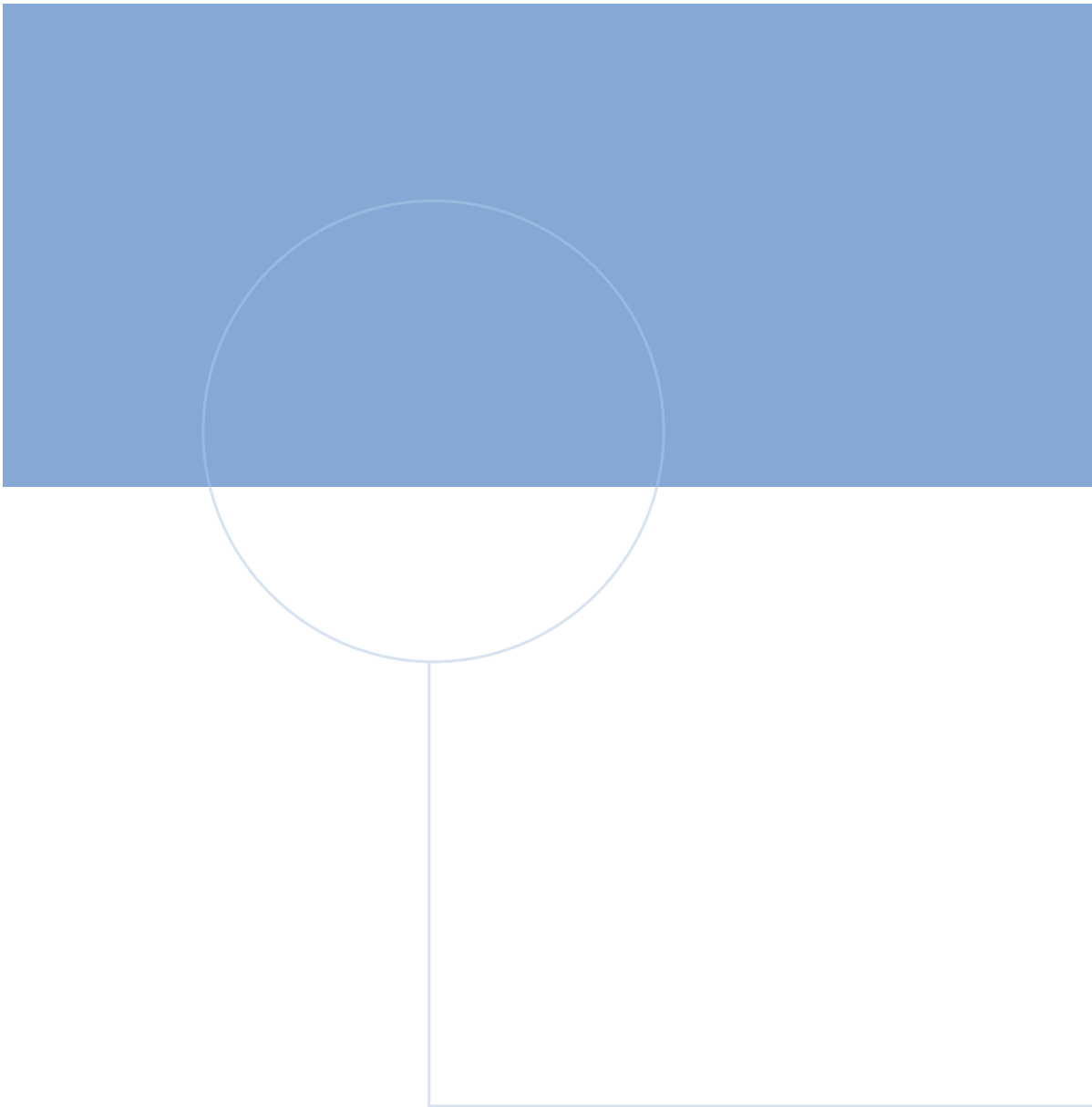

NTNU

Kunnskap for en bedre verden